EXPLORING SURFACE PROPERTIES OF ADVANCED NI-BASED CONCENTRATED SOLID-SOLUTION ALLOYS BY NANOMECHANICAL TECHNIQUES

by

Liuqing Yang

A dissertation submitted to the faculty of
The University of North Carolina at Charlotte
in partial fulfillment of the requirements
for the degree of Doctor of Philosophy in
Mechanical Engineering

Charlotte

2024

Approved by:

_____
Dr. Youxing Chen

_____
Dr. Harish Cherukuri

_____
Dr. Qiuming Wei

_____
Dr. Yong Zhang

_____
Dr. John Shingledecker

ABSTRACT

LIUQING YANG. Exploring surface properties of advanced Ni-based concentrated solid-solution alloys by nanomechanical techniques. (Under the direction of DR. YOUXING CHEN)

The invention of concentrated solid solution alloys (CSAs) has vastly expanded the compositional space of alloys, which provides properties that cannot be achieved by conventional alloys. Ni-based CSAs have shown the potential for exceptional toughness and radiation resistance, which make these alloys viable candidate materials for energy and nuclear industries. Different from conventional alloys with only one principal element, CSAs contain multiple elements with equal or near equal compositions and have unique intrinsic properties such as a high entropy effect, severe lattice distortion, sluggish diffusion, and cocktail effect. However, as new-emerging materials, the theoretical and experimental investigations on their performances are still limited. The goal of this thesis is to (a) develop nanomechanical methods to exact mechanical properties of Ni-based CSAs. (b) apply nanomechanical methods to detect radiation-induced defects and radiation hardening of Ni-based CSAs. (c) yield stress-strain curves directly from flat punch nanoindentation to study the effect of radiation on work hardening behaviors of Ni-based CSAs.

First, we explore the deformation mechanisms of a set of five Ni-based CSAs, including NiCo, NiFe, $Ni_{80}Cr_{20}$, $N_{80}Mn_{20}$, and NiCoFeCr, by nanoindentation with the Berkovich tip. We developed a complete methodology for nanoindentation to extract accurate hardness, elastic modulus and strain rate sensitivity and investigate deformation mechanisms, considering indentation size effect. Our results show that the most effective strengthening mechanisms in these alloys are attributed to lattice distortion from the mismatch in atomic size. The element type of alloying elements plays a more important role than the number of alloying elements in strengthening CSAs.

Second, based on the first study above, nanoindentation is further used to study the early-stage radiation-induced damage on NiCo, NiFe and NiCoFeCr. Understanding the defect nucleation and accumulation at the nascent stage is important but challenging due to the difficulty of quantifying point defects induced by low-dose irradiation at this regime. It is hypothesized that the interactions between radiation-induced defects and deformation-induced dislocations can be used to quantify the radiation-induced defects. The distinct radiation-induced hardening observed in three CSAs can be explained by two factors: the formation of radiation-induced defects and the increased density of geometrically necessary dislocations (GNDs) related to the indentation size effect (ISE). Quantitative analysis reveals significant hardening caused by radiation-induced defects in NiFe and NiCoFeCr sample, but not in the NiCo sample. Meanwhile, the irradiation results in a higher GND density in NiCo and NiFe, but not in NiCoFeCr, which is attributed to the volume change of the plastic zone.

Lastly, conventional nanoindentation cannot produce data that can be converted into a uniaxial stress-strain curve for easy evaluation of materials properties. Therefore, in the final part, we strive to achieve uniaxial stress-strain curves of unirradiated and irradiated CSAs by 1-μm flat punch indentation. The protocol is developed based on Hay's method with consideration of thermal drift and successfully capture strength and work hardening of CSAs. The radiation hardening is pronounced in both NiCo and NiCoFeCr, though NiCoFeCr exhibits less hardening and a lower dependency on radiation dose. In addition, strain hardening capability degrades due to irradiation in both NiCo and NiCoFeCr with the degradation being less obvious in NiCoFeCr. This suggests that flat punch nanoindentation could be a promising tool for understanding radiation-induced property degradation and accelerating the development of new alloys.

DEDICATION

To my grandma

She raised me, but cannot witness this moment

She was not well-educated, but she was the wisest person I have ever seen in my life.

She did not have the chance to get an education even though she was eager to.

ACKNOWLEDGEMENTS

I would like to first thank my advisor, Dr. Youxing Chen. I still remember the first day we met, everything new to me and I was feeling nervous but more excited. I am fortunate to be his first student and I am always happy to work with him. The completion of my PhD journey would have been impossible without your invaluable assistance and guidance.

I am also grateful to Dr. Terry Xu for her guidance and warm support. I really appreciate her time to talk with me and share her experiences with me.

I also would like to express my gratitude to my defense committee members, Dr. Harish Cherukuri, Dr. Qiuming Wei, Dr. Yong Zhang and Dr. John Shingledecker for their guidance and precious suggestions on my research work and thesis.

Many thanks to my friend Dr. Manira Akter (my first friend in the United States) and thanks for her delicious meals, snacks and milk tea. Also, thanks to my close friend Dr. Yue Xin, we support each other to spend the long PhD journey.

I am greatly indebted to my parents, grandparents and all family members for their complete and continued love. Special appreciation to my elder sister, she is always my role model and inspired me to explore the world.

Special thanks to Junxiao Liu, who always gave me greatest support in this PhD journey. Without her support, I would never have the courage to keep going.

It’s time to say goodbye and hope everyone has a happy summer!

TABLE OF CONTENTS

List of figures x
List of tables xiv
List of abbreviations xv
Chapter 1 : Introduction and literature review 1
1.1 Novelty of CSAs compared to conventional alloys 1
1.1.1 High entropy effect 2
1.1.2 Lattice distortion 3
1.1.3 Sluggish diffusion effect 4
1.1.4 Cocktail effect 5
1.2 Superior mechanical properties and radiation tolerance of CSAs 6
1.2.1 Mechanical properties of CSAs 7
1.2.2 Deformation mechanisms in CSAs 9
1.2.3 Strengthening mechanisms in CSAs 13
1.2.4 Radiation response of CSAs 21
1.3 Nanomechanical characterizations on surface properties 24
1.3.1 Nanomechanical studies of high-entropy alloys 24
1.3.2 Advancement of nanoindentation techniques 27
1.3.3 Current challenges on nanomechanical study 28
1.3.4 Specific challenges in nanoindentation 30
1.4 Research motivations and hypotheses 35
Chapter 2 : Experimental 37
2.1 Fabrication and preparation of Ni-containing concentrated solid solution alloys 37
2.2 Ion irradiation 38
2.3 Microstructural characterizations: SEM and TEM 40
2.4 Surface topography imaging 42
2.5 Berkovich indentation 43
2.6 Flat punch indentation 46
Chapter 3 : Deformation mechanisms in single crystal Ni-based concentrated solid solution alloys by nanoindentation 48

3.1 Overview 48
3.2 Introduction 49
3.3 Materials & methods 54
3.4 Results and discussion 55
3.4.1 Nanoindentation hardness correction 56
3.4.2 GNDs and SSDs in CSAs 62
3.4.3 Strain rate sensitivity and activation volume in CSAs 64
3.4.4 Deformation mechanisms of CSAs under indentation 67
3.5 Conclusions 72
3.6 Acknowledgements 74
Chapter 4 : Nanoindentation study on early-stage radiation damage in single-phase concentrated solid solution alloys 75
4.1 Overview 75
4.2 Introduction 76
4.3 Materials and methods 78
4.4 Results 82
4.4.1 Estimated radiation damage profile 82
4.4.2 Nanoindentation analysis 82
4.4.3 Pile-up examination 85
4.4.4 Corrected hardness and modulus analysis 87
4.5 Discussion 90
4.5.1 Radiation-induced hardening 90
4.5.2 Radiation-induced dislocation density changes 92
4.5.3 The volume of plastic zone in irradiated CSAs 94
4.6 Conclusions 97
4.7 Acknowledgments 98
Chapter 5 : Investigation of radiation response and mechanical behavior of Ni-concentrated solid solution alloys by flat punch indentation 99
5.1 Overview 99
5.2 Introduction 99
5.3 Experimental 101

5.3.1 Materials synthesis and ion irradiation 101
5.3.2 Flat punch indentation 102
5.4 Results 103
5.4.1 Thermal drift correction and contact point determination 103
5.4.2 Corrected indentation properties of NiCo and NiCoFeCr 106
5.4.3 Acquisition of stress-strain curves 108
5.4.4 Construct stress-strain curves 109
5.5 Discussion 111
5.5.1 Radiation hardening in NiCo and NiCoFeCr 111
5.5.2 Radiation-induced change in strain hardening 113
5.6 Conclusions 113
5.7 Acknowledgements 114
Chapter 6 : Conclusions and future work 115
6.1 Conclusions 115
6.2 Future work 116
Supplementary Materials 118
References 123

LIST OF FIGURES

Figure 1.1 Ball and stick models of different alloy systems show extent of lattice distortion. (a) pure metal (b) dilute alloy (c) high entropy alloy. This figure is from Ref. [2]. 4
Figure 1.2 Diffusion coefficients of D_{Ni} in a series of HEA FCC alloys against the temperature T_m/T. The figure is from Ref. [2] including NiCo [19], NiFe [19], NiCoFe [19], NiCoCr [19], NiCoFeCr [19], NiCoFeCrMn [19], NiCoFeCrPd [19], CoCrFeMnNi [20], CoCrFeNi [20], and $FeCoCrNiMn_{0.5}$ [21, 22]. 5
Figure 1.3 The effect of four core effects on physical metallurgy and mechanical properties of HEAs. Solid lines indicate the direct influence and dash lines represent the indirect influence. This figure is from Ref. [23]. 6
Figure 1.4 (a) ultimate tensile strength – ductility map of HEAs in the context of traditional alloys. This figure is from Ref. [2]. (b) the comparison of HEAs to other traditional alloy systems. This figure is from Ref. [33]. 9
Figure 1.5. Representative TEM bright-field micrographs from the gauge sections of interrupted tensile test specimens of the coarse-grained CoCrFeMnNi alloy after relatively small tensile strains: (a) 1.7% at 873 K, (b) 2.4% at 77 K and (c) 2.1% at 293 K. Planar slip of ½ <110>-type dislocations on {1 1 1}-type fcc planes is a dominant feature at all three investigated temperatures. The figure is from Ref. [25]. 10
Figure 1.6 TEM observations of dislocation slip-twinning transition in NiCoFeMn at 77 K. The figure is from Ref. [26]. 11
Figure 1.7 Schematics descriptions of the (a) Fleischer model and (b) Labusch model. The figure is from Ref. [67]. 16
Figure 1.8 Schematic descriptions of precipitation hardening mechanisms. (a) shearing mechanism. (b) bow-out mechanism. This figure is from Ref. [84]. 20
Figure 1.9 (a) the length scales related to structural defects and dislocation systems span from the micrometer down to the nanometer scale. (b) examples of commonly used nanomechanical techniques: nanoindentation, micropillar compression, microcantilever bending, micro-tensile tests, and nanopillar compression (from left to right). These images are from Ref. [119]. 25
Figure 1.10 Schematic map shows the size dependence of flow shear stress to shear modulus upon characteristic size for five orders of magnitude. Inset presents a diagram of theoretical strength. This figure is from Ref. [125]. 29
Figure 1.11 Various mechanical testing methods for micron to sub-micron length samples. This figure is from Ref. [132]. 30
Figure 1.12 Nanoindentation on NiCo sample with pyramidal indenter that shows clear indentation size effect. 31
Figure 1.13 Dislocations created by a rigid conical indentation. It is idealized as circular dislocation loops. The figure is from Ref. [136]. 32

Figure 1.14 (a) The plot of H^2 versus 1/h for (111) Cu and (b) the fitting result of (110) Ag both obtained in nanoindentation experiments with the Berkovich indenter. The figure is from Refs. [134, 137]. 33
Figure 1.15 (a) schematic demonstration of pile-up and sink in during nanoindentation. (b) contact area of pile up (c) contact area of sink in. These figures are from Ref. [141]. 34
Figure 2.1 Buttons of NiCo, NiFe, $Ni_{80}Cr_{20}$, $Ni_{80}Mn_{20}$ and NiCoFeCr after careful polishing. All specimens present "mirror-like" surfaces. 38
Figure 2.2 Photographs of ion irradiation beamlines at the Ion Beam Materials Laboratory (IBML) at the University of Tennessee [146]. 39
Figure 2.3 Sample arrangements for ion irradiations: total 6 portions with different radiation exposure conditions. #V is the un-irradiated portion for reference. 39
Figure 2.4 SRIM predicted profile for radiation damage (purple) and implanted Ni ion distribution (blue) of NiFe sample. 40
Figure 2.5 TEM (JEOL 2100) installed in UNC Charlotte 42
Figure 2.6 Photographs of Nano Indenter G200 (MTS). 43
Figure 2.7 A typical load-depth curve for NiCo samples. 44
Figure 2.8 Typical hardness-displacement and modulus-displacement recorded by using CSM method. 46
Figure 2.9 Photographs of Hysitron PI-88 picoindenter installed inside of SEM chamber. 47
Figure 2.10 Screenshots of in-situ nanoindentation testing process performed on Si. 47
Figure 3.1 Bright-field TEM image of the region underneath the indenter for NiCo. The inset of the selected-area diffraction pattern confirms the single-crystal structure after indentation and the surface normal of <100> crystallographic direction. 56
Figure 3.2 (a) a comparison of nanoindentation hardness (H) evolution of Ni, NiCo, $Ni_{80}Mn_{20}$, $Ni_{80}Cr_{20}$, NiFe and NiCoFeCr as a function of displacement (h, penetration depth); (b) a plot of H^2 vs. 1/ h with linear fitting on Ni and CSAs; (c) a summary of slopes and intercepts of fitting lines in (b). 57
Figure 3.3 AFM micrographs of indentation imprints for Ni, NiCo, NiFe, $Ni_{80}Mn_{20}$, $Ni_{80}Cr_{20}$, and NiCoFeCr. Pile-ups exist in all samples. 58
Figure 3.4 (a) AFM image of an indentation imprint on $Ni_{80}Cr_{20}$ displays apparent pile-ups; (b) the surface profiles of ideal and real pile-up profiles are schematically shown to determine the contact periphery of the indenter (ai) and height of pile-up (h_i); (c-d) the three surface profiles in (a) show a_i and h_i (i=1-3). 61
Figure 3.5 A summary of nanoindentation hardness at 2 μm (H_{IT}), macro-hardness (H_0) from Nix-Gao model, pile-up corrected H_{IT} (H_{IT_C}), pile-up corrected H_0 (H_{0_C}) hardness. 62
Figure 3.6 Densities of Statistically Stored Dislocations (SSD, ρ_S) and Geometrically Necessary Dislocations (GND, ρ_G) for Ni and CSAs calculated from the Ma-Clarke model. 63
Figure 3.7 Depth dependence of GND density in Ni and CSAs. The inset schematically shows GNDs distributed within a hemispherical volume underneath an indenter. 64

Figure 3.8 (a) determination of strain rate sensitivity by considering the hardness change rate (unit: Pa/s) during nanoindentation strain rate jump tests. Nominal nanoindentation strain rates are 0.05/s, 0.007/s and 0.001/s. (b) the values of strain rate sensitivity and corresponding activation volume for Ni and CSAs. 67
Figure 4.1 Representative load-depth curve of un-irradiated NiCo with maximum indentation depth of 1000 nm. Insets present the schematic demonstration of CSM method. 80
Figure 4.2 (a) SRIM predicted profile for radiation damage and implanted Ni ion distribution of NiFe sample. (b) the magnified region in (a) for a depth less than 1000 nm. 82
Figure 4.3 Summary of continuous and scattered (a-c) hardness and (d-f) elastic modulus results of NiCo, NiFe and NiCoFeCr before and after irradiation. The shade areas represent the standard deviation of six indentations. 84
Figure 4.4 AFM micrographs of indentation imprints for NiCoFeCr sample penetrated to 500 nm (a) before irradiation and (b) after irradiation. 85
Figure 4.5 Pile-up correction factors and tendencies of various samples at 300, 500, 700 and 1000 nm penetration depths: (a) NiCo (b) NiFe (c) NiCoFeCr. 87
Figure 4.6 Comparisons of (a-c) nanoindentation hardness and (d-f) elastic modulus results before and after pile-up corrections for NiCo, NiFe and NiCoFeCr, respectively. Error bars are provided in all data points. 88
Figure 4.7 Nanoindentation results plotted by H^2 versus $1/h$ for un-irradiated and irradiated samples before and after pile-up correction: (a) NiCo (b) NiFe (c) NiCoFeCr. The shade areas represent the standard deviation of six indentations. 89
Figure 4.8 (a-c) Nix-Gao fitting results of NiCo, NiFe and NiCoFeCr samples after pile-up corrections. (d) summarization of macro-hardness values H_0 and characteristic depth h* of NiCo, NiFe and NiCoFeCr. 90
Figure 4.9 Hardness induced by the change in GND density in irradiated NiCo, NiFe and NiCoFeCr. 92
Figure 4.10 GND densities in NiCo, NiFe and NiCoFeCr samples before and after irradiation. 94
Figure 4.11 Schematic drawing of plastic zone underneath the indenter during indentation, including an ideal hemi-sphere with radius of a prior to irradiation and the "effective radius" of irradiated NiCo, NiFe and NiCoFeCr. 97
Figure 5.1 Sample arrangements for ion irradiation in this study: total 6 portions with different radiation exposure conditions. 102
Figure 5.2 Two steps of corrections of load-depth curves (datapoints from NiCo). (a) demonstration of thermal drift correction. (b) comparison of raw data and thermal drift corrected results. (c) criterion of contact point determination. (d) curves after reset the zero point. 105
Figure 5.3 Load-depth curves of flat punch indentations on virgin and irradiated regions with 5 different doses for (a) NiCo and (b) NiCoFeCr samples. The shadow areas represent the standard deviations of measurements. 107

Figure 5.4 (a) an example of stiffness-depth curve in NiCo sample. (b) demonstration of determination of fitted range and yield point based on stiffness criterion. 110
Figure 5.5 Stress-strain curves by flat punch indentation. (a) NiCo and (b) NiCoFeCr. The shadow areas represent the standard deviations of measurements. 111
Figure 5.6 The yield strength and strain hardening exponent of NiCo and NiCoFeCr as the function of radiation dose. (a) yield strength. (b) strain hardening exponent. 112

LIST OF TABLES

Table 1.1 A summary of recent experimental results of HEAs studied by various mechanical techniques. 26
Table 1.2 Main testing modes are involved in nanoindentation. The table is from Ref. [125]. ... 28
Table 3.1 A summary of stacking fault energies (SFEs) yield and ultimate tensile strengths (σ_Y and σ_{UTS}) and estimated strain during nanoindentation for Ni and CSAs 69
Table 3.2 Solid Solution Strengthening in Ni and CSAs. 72
Table 5.1 Summary of strain hardening exponents and yield strength of NiCo and NiCoFeCr sample in six different areas. 112

LIST OF ABBREVIATIONS

AFM	Atomic Force Microscope
BCC	Body-Centered Cubic
CCA	Complex, Concentrated Alloy
CSA	Concentrated Solid-solution Alloy
CSM	Continuous Stiffness Measurement
EBSD	Electron Backscatter Diffraction
EDM	Electro Discharge Machine
FCC	Face-Centered Cubic
FIB	Focus Ion Beam
GND	Geometrically Necessary Dislocation
HEA	High Entropy Alloy
ISE	Indentation Size Effect
MPEA	Multi-Principal Element Alloy
MEA	Medium Entropy Alloy
PAS	Positron Annihilation Spectroscopy
SAD	Selected-Area Diffraction
SFE	Stacking Fault Energy
SGP	Strain Gradient Plasticity
SRIM	Stopping and Range of Ion in Matter
SRO	Short-Range Order
SSD	Statistically Stored Dislocation
TEM	Transmission Electron Microscopy
A	Geometrical Contact Area
Ac	Corrected Contact Area
A_{pu}	Pile-up Area
a	Contact Radius of Indenter
a_i	Contact periphery of the indenter
b	Burgers Vector
c_i	Atomic Percentage of Component
E	Elastic Modulus
E_i	Elastic Modulus of Indenter
E_r	Reduced Elastic Modulus
h	Penetration Depth

h^*	Characteristic Depth
h_c	Contact Depth
h_i	Height of pile-up
h_m	Maximum Depth During Loading
h_S	Height of Spherical Cap
H	Nanoindentation Hardness
$\dot{H}$	Hardness Change Rate
H_0	Macro-hardness
H_{0_C}	Pile-up Corrected H_0
$H_{0_{irradiated}}$	Macro-hardness of Irradiated Material
$H_{0_{un-irradiated}}$	Macro-hardness of Un-irradiated Material
H_C	Pile-up Corrected H
H_{IT}	Nanoindentation Hardness
H_{IT_C}	Pile-up Corrected H_{IT}
$H_{irradiated}$	Hardness of Irradiated Material
$H_{un-irradiated}$	Hardness of Un-irradiated Material
$\dot{h}$	Displacement Rate
h	Instantaneous Displacement
l	Length of Dislocation Segment
m	Strain Rate Sensitivity
M	Taylor Factor
P	Indentation Load
P_{max}	Maximum Indentation Load
$\dot{P}$	Loading Rate
r_i	Atomic Radius of Component
S	Contact Stiffness
T	Absolute Temperature
V	Activation Volume
V_f	Activation Volume of Forest Hardening
V_{SS}	Activation Volume of Solid Solution Strengthening
V_n	Atomic Volume
$V_{irradiated}$	Volume of Plastic Zone in Irradiated Material
$V_{un\_irradiated}$	Volume of Plastic Zone in Un-irradiated Material
ΔH_0	Hardness from Radiation-induced Defects
ΔH_{GND}	Hardness Induced by Change in GND Density
w	Distance of Overcoming Energy Barrier

α	Dislocation Line Tension Parameter
γ	Average Shear Strain
ΔE_b	Total Energy Barrier
$\Delta \bar{V}_n$	Average Misfit Volume
δ	Lattice Distortion
δ_G	Lattice Distortion Calculated Using Goldschmidt Radius
δ_{rlx}	Lattice Distortion Calculated from Relaxed Structure
$\dot{\varepsilon}_\iota$	Strain Rate for Nanoindentation
κ	Boltzmann Constant
μ	Shear Modulus
ρ_G	Density of Geometrically Necessary Dislocation
$\rho_{G\_irradiated}$	Density of Geometrically Necessary Dislocation in Irradiated Material
$\rho_{G\_un-irradiated}$	Density of Geometrically Necessary Dislocation in Un-irradiated
ρ_S	Density of Statistically Stored Dislocation
σ	Strength
σ_Y	Yield Strength
σ_{UTS}	Ultimate Tensile Strength
σ_{ss}	Solid Solution-induced Strength
τ_{y0}	Zero-temperature Flow Stress
υ	Poisson's Ratio of Specimen
υ_i	Poisson's Ratio of Indenter

CHAPTER 1 : INTRODUCTION AND LITERATURE REVIEW

A new class of alloys composed of multiple elements in equiatomic concentrations was reported by two independent research groups in 2004. Unlike conventional alloys which are constrained by a limited number of element combinations due to their tendency to cluster at the corners or edges of phase diagrams, these new alloys are located near the centers of phase diagrams. This positioning allows for a significantly broader range of element combinations, particularly in quaternary, quinary, and higher-order systems. Yeh and co-workers introduced a new name, high entropy alloys (HEAs), for this new class of alloys which contain five or more elements in relatively high concentrations (5–35 at.%). The concept of HEA has created a wave of research to explore the extended materials design space for mechanical properties and radiation tolerance. The literature also references alternative terminologies with extended concepts, such as multi-principal element alloys (MPEAs), complex concentrated alloys (CCAs), and concentrated solid solution alloys (CSAs). Despite debates about the predominance of entropic stabilization, the HEA concept has inspired a re-evaluation of classical thermodynamic concepts as they apply to CSAs. In this study, the name of CSAs is adopted, as binary alloys without high entropy are included. However, it is noticed that many discussions on structure and properties of CSAs are based on studies of HEAs.

1.1 Novelty of CSAs compared to conventional alloys

The novelty of CSAs can be explained by HEAs. It was found that an increased mixing entropy can facilitate the creation of durable microstructures comprised of a single phase [1]. In the past decades, over 37 elements have been involved in fabrication of high entropy alloys. Ni,

Fe, Cr, Co, Al and Cu are most commonly used elements among these constituent elements, which are typically feasible to make HEAs with face-centered cubic (FCC) crystal structures [2]. In addition, refractory elements such as Ta, Nb, Mo, Zr and V are often used to make body-centered cubic (BCC)-structured refractory alloys [3]. Beside the crystal structure, four fundamental characteristics distinguish HEAs from other conventional alloys, which are widely recognized as high entropy effect, pronounced lattice distortion, slow diffusion, and cocktail effect [4, 5].

1.1.1 High entropy effect

HEAs with high entropy exhibit a tendency to form solid solutions rather than complex intermetallic compounds, as the high entropy effect considers the free energies of various states to determine the equilibrium structure and microstructure and drives the system towards the equilibrium state. The promotion of high entropy in the formation of simple solid solutions can be comprehended from the perspective of thermodynamic [6-8]. Generally, the determination of whether a reaction can outcompete others is governed by the Gibbs free energy associated with its mixing, which can be computed by Eqn. 1.1 as follows [9]:

$$\Delta G_{mix} = \Delta H_{mix} - T\Delta S_{mix} \tag{1.1}$$

where T is the temperature, ΔH_{mix} is the enthalpy of mixing, which is the measure of energy change under constant pressure and temperature, ΔS_{mix} is the entropy if mixing, which is the evaluation of randomness of a system. For the ideal solid solutions in the HEAs:

$$\Delta H^{ss}_{mix,ideal} = 0;\ \ \Delta G^{SS}_{mix,ideal} = -T\Delta S_{mix} \tag{1.2,1.3}$$

If assuming intermetallic compounds are perfectly ordered:

$$\Delta S^{IM}_{mix,ideal} = 0;\ \ \Delta G^{SS}_{mix,ideal} = \Delta H^{IM}_{mix,ideal} \tag{1.4,1.5}$$

It can be easily concluded that $\Delta G^{SS}_{mix,ideal} < \Delta G^{IM}_{mix,ideal}$, thereby formation of solid solution can win the competition and be preferred to compose phases rather than formation of complex intermetallic compounds.

1.1.2 Lattice distortion

The extent of lattice distortion can be observed by examining the hard-sphere model of the lattice for materials. As viewed in Fig. 1.1 [2], pure metals exhibit no lattice distortion as they have identical atoms occupying the lattice sites, while addition of a small amount of a second atomic species in conventional dilute alloys leads to minor lattice distortion. In the structure of HEAs, the solute matrix experiences significant lattice distortion because every atom on the lattice site has different first neighboring atoms, resulting in atomic size difference, non-symmetric bonding, and electron distribution-induced distortion [10-14]. In such a scenario, the distorted lattice of HEAs would exhibit crystalline imperfections such as vacancies, dislocations, stacking faults, which affect mechanical behaviors as well as the electrical conductivities of HEAs. Notice that profound lattice distortion has been detected by X-ray and neutron diffraction [12, 15] and lattice distortion is claimed to be responsible for strengthening in HEAs. Theoretically, differences in atomic size are often associated with lattice distortion, and Eqn. 1.6 is commonly utilized to evaluate this distortion [16].

$$\delta = \sqrt{\sum\nolimits_{i=i}^{N} c_i(1 - r_i / \sum\nolimits_{j=1}^{N} c_j r_j))^2} \tag{1.6}$$

where N is the number of the components in an alloy system, c_i is the atomic percentage of the ith component, $\sum_{j=1}^{N} c_j r_j$ is the average atomic radius, and r_i is the atomic radius.

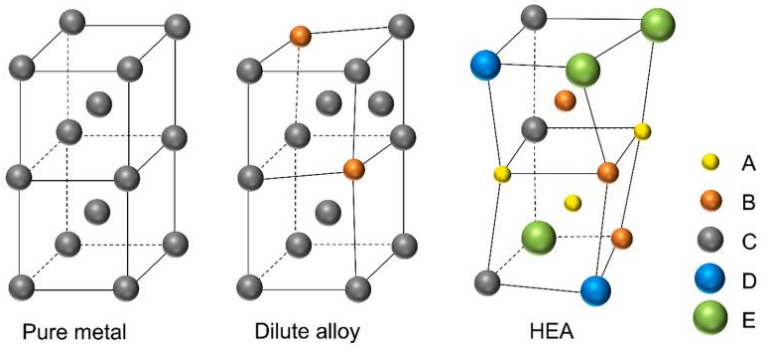

Figure 1.1 Ball and stick models of different alloy systems show extent of lattice distortion. (a) pure metal (b) dilute alloy (c) high entropy alloy. This figure is from Ref. [2].

1.1.3 Sluggish diffusion effect

The theory of phase transformation states that the creation of new phases from pre-existing ones necessitates the collaborative diffusion of numerous types of atoms to facilitate the separation of composition. On one hand, Due to the absence of a dominant element in HEAs, the diffusion efficiency is anticipated to be inferior to that of conventional alloys [17]. Subsequent studies have substantiated this characteristic by contrasting the observed diffusion rates of Ni in both HEAs and medium-entropy alloys, as outlined in Fig. 1.2 [2]. The trend shown in this figure illustrates the degree of sluggish diffusion effect to became more pronounced as a greater number of elements and increased concentrations are incorporated. On the other hand, the diffusion of a particular species in HEAs is anticipated to be slower because of lattice distortion, which produces fluctuations in lattice potential energy and an increase in activation energy along the diffusion pathway [11, 18].

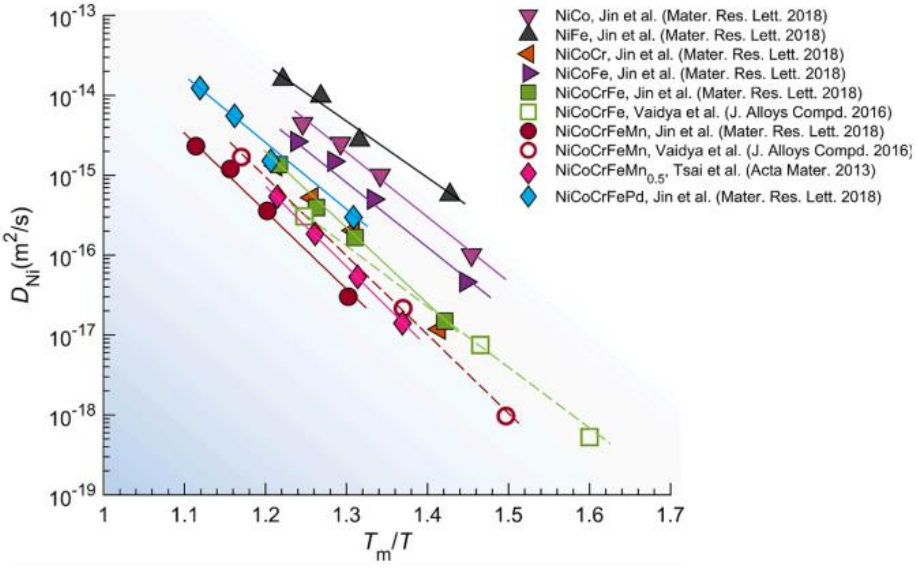

Figure 1.2 Diffusion coefficients of D_{Ni} in a series of HEA FCC alloys against the temperature T_m/T. The figure is from Ref. [2] including NiCo [19], NiFe [19], NiCoFe [19], NiCoCr [19], NiCoFeCr [19], NiCoFeCrMn [19], NiCoFeCrPd [19], CoCrFeMnNi [20], CoCrFeNi [20], and $FeCoCrNiMn_{0.5}$ [21, 22].

1.1.4 Cocktail effect

The cocktail effect is the synergistic effect encompasses the collective impact of composition, structure, and microstructure on material properties. HEAs typically contain more than four principal elements in roughly equal proportions, resulting in unique and sometimes unexpected properties that cannot be predicted from the behavior of individual elements.

Apart from the four core effects recognized above, there are surely some other factors affecting the crystal structure, microstructure, and properties of HEAs such as temperature and alloy design strategy [23]. But high entropy effect, severe lattice distortion, sluggish diffusion effect and cocktail effect still play critical roles in the discovery of HEAs.

Fig. 1.3 [23] systematically shows the comprehensive influence of these four core effects on physical metallurgy of HEAs and their properties. The solid arrows represent that the effect is direct, and the dash ones represent that the effect is indirect. First, to determine the equilibrium structure and microstructure and the driving force towards it, one must consider the high entropy effect on the free energies of various states. Second, the sluggish diffusion effect hinders the nucleation and growth rates during phase transformation. Additionally, the severe lattice distortion effect influences both mechanical properties (e.g., strength, ductility, and strain rate sensitivity) and physical properties (e.g., electrical resistivity and magnetism). Finally, the cocktail effect contributes to an excess amount of each property, owing to interactions between elements, distorted lattice, and phase distribution beyond the mixture rule based on composition.

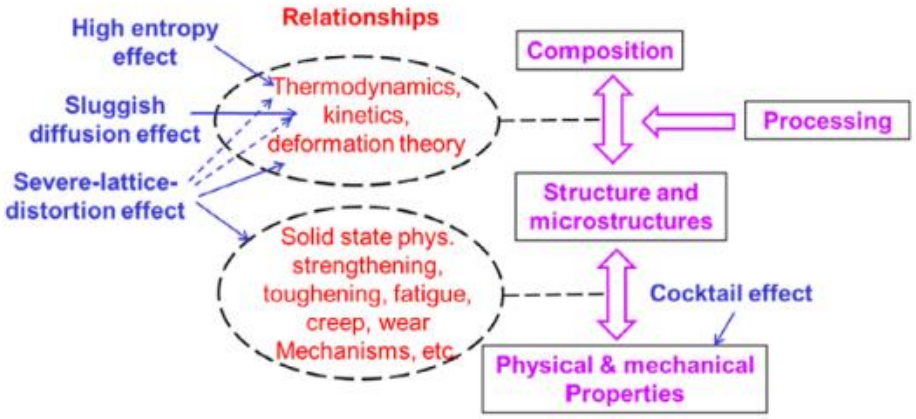

Figure 1.3 The effect of four core effects on physical metallurgy and mechanical properties of HEAs. Solid lines indicate the direct influence and dash lines represent the indirect influence. This figure is from Ref. [23].

1.2 Superior mechanical properties and radiation tolerance of CSAs

Research interests of HEAs are predominantly inspired by the outstanding properties and performance above the threshold of conventional alloys. On one hand, HEAs have been reported

to present excellent surface properties, including tolerance of high load, wear, and erosion resistance. On the other hand, some HEAs exhibited exceptional radiation tolerance at both ambient and elevated temperature, which are proposed as promising candidates for demanding structural materials in nuclear reactors.

1.2.1 Mechanical properties of CSAs

Key mechanical properties of structural materials include strength and ductility but there is a common strength-ductility tradeoff: higher strength is general along with sacrifice of ductility, which is not desired in applications. The discovery of HEAs provides a potential to breakdown the strength-ductility paradox because the HEAs offer a vast composition space along with highly tunable properties. The first-time tensile testing was performed on CoCrFeNiMn (Cantor alloys) by Gali *et al.* [24]. They reported some crucial features of Cantor alloys: the tensile strength and ductility of CoCrFeNiMn exceeds 1 GPa and 60% respectively when the operation temperature decreases to 77K. And the strength of these alloys shows a strong temperature dependence below 473K while it exhibits a weak dependence on higher temperature up to 1273K. This excellent strength-ductility property is attributed to the accelerated strain hardening rate at cryogenic temperatures. Consistently, this Canor alloy exhibits exceptional fracture toughness with ~ 220 MPa $m^{1/2}$. Subsequent studies further investigated the deformation mechanisms of Cantor alloys by characterizing the dislocation and microstructural evolution [25-27]. In addition, Li *et al.* [28] reported a dual-phase $Fe_{50}Mn_{30}Co_{10}Cr_{10}$ HEA shows potential to overcome long-standing strength-elongation tradeoff through martensite transformation to partially form hexagonal-close packed structures. Recently, G. Laplanche [29] claimed that a medium-entropy alloys NiCoCr shows superior tensile properties than Cantor alloys at 77K and

273K. Nevertheless, the strength and ductility of HEAs have not presented apparent advantages in comparison to various conventional alloying systems (Fig. 1.4a). Common strategies such as triggering twinning-induced plasticity and transformation-induced plasticity are also applied to reinforce the strength of HEA alloys.

The Ashby map shown in Fig. 1.4b [28, 30-32] summarizes the fracture toughness against the yield strength for a batch of HEAs with different microstructures. The general tendency of HEA systems can be collected as follows:

- HEAs with FCC microstructures generally have high fracture toughness but low yield strength.
- HEAs with BCC microstructures have moderately high yield strength but limited fracture toughness.
- Multi-phase HEAs have intermediate yield strength and fracture toughness.
- Metastable HEAs are analogous to FCC HEAs: high fracture toughness but relatively low yield strength.

In comparison to other material systems, a large portion of HEAs is distributed in the top-right part of Ashby map (Fig. 1.4b). This is the striving direction for material exploration to search for outstanding damage-tolerance properties. HEAs exhibit advantageous potential to break the long-standing strength-ductility tradeoff in alloying systems.

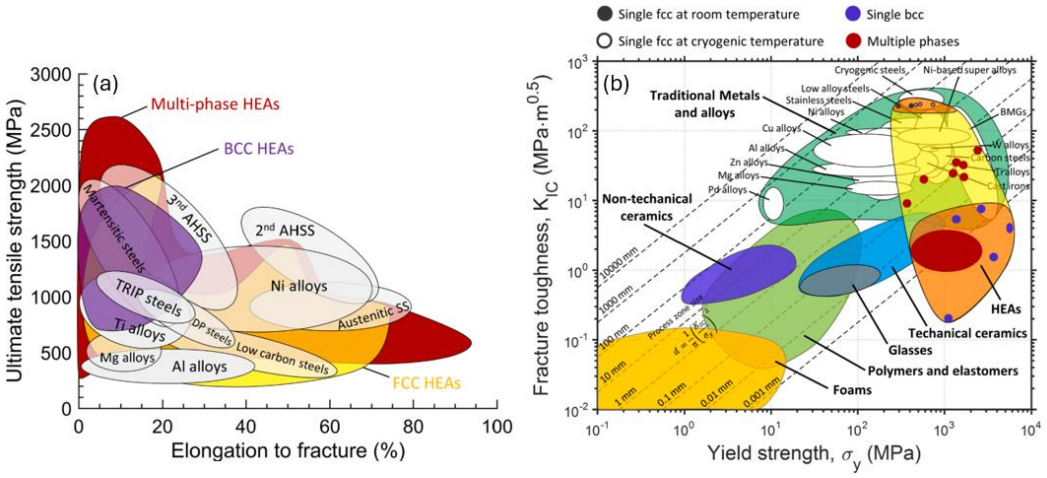

Figure 1.4 (a) ultimate tensile strength – ductility map of HEAs in the context of traditional alloys. This figure is from Ref. [2]. (b) the comparison of HEAs to other traditional alloy systems. This figure is from Ref. [33].

1.2.2 Deformation mechanisms in CSAs

Understanding the deformation mechanisms is important to pursue the enhancement of the mechanical performance of HEAs. Generally, the deformation mechanisms are dependent on alloying systems with respect to crystal structure and alloying elements, also as is in HEAs alloying systems. In this section, major deformation mechanisms governing the mechanical behaviors of HEAs will be reviewed including dislocation mediated deformation mechanism, nano-twining mediated deformation mechanism and phase-transformation mediated deformation mechanism and joint effect from multiple deformation mechanisms.

Dislocation-mediated deformation mechanisms: Most deformation mechanisms in FCC and BCC HEAs are same as conventional FCC and BCC metal. The wide option of alloying elements in HEAs provides more control on different contributing mechanisms. Meanwhile, complex composition in HEAs brings new mechanisms. In FCC HEAs, planar deformation involving ½ <110>-type dislocation arrays on {111} slip planes are often observed, e.g., the

study of NiCoFeCrMn in the early stage of plastic deformation by Otto et al. [25]. Same as in conventional FCC metals, these full dislocations often dissociate into partial dislocations (Fig. 1.5) and the dissociation could be modified by tuning the relatively low stacking fault energy in HEAs. The interaction of these dislocation cores could also react to form Lomer-Cottrell locks [34], which contribute to work hardening. However, the energy barriers for these dislocation activities are distinct with conventional alloys due to solute concentration fluctuations [35]. One the other hand, for the BCC HEAs, screw dislocations are dominant in deformation, e.g., TiZrHfNbTa HEA by Couzinie *et al.* [36], same as conventional BCC metals. However, the local compositional variations in BCC HEAs can modify the deformation by tuning intrinsic properties, such as stacking fault energies for different slip planes, which promotes jog formation [37].

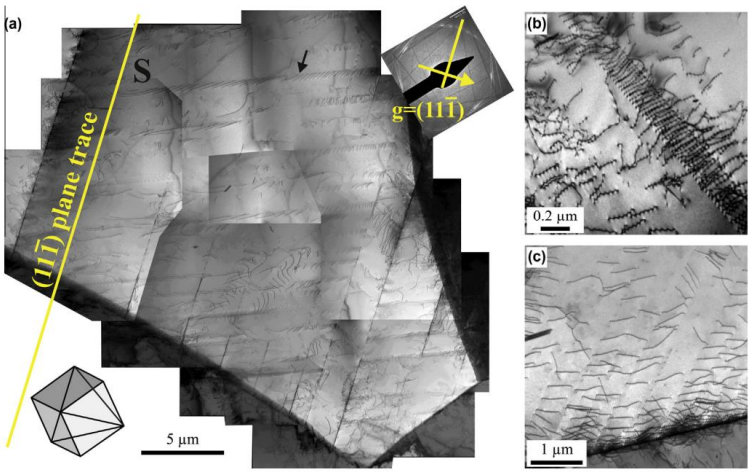

Figure 1.5. Representative TEM bright-field micrographs from the gauge sections of interrupted tensile test specimens of the coarse-grained CoCrFeMnNi alloy after relatively small tensile strains: (a) 1.7% at 873 K, (b) 2.4% at 77 K and (c) 2.1% at 293 K. Planar slip of ½ <110>-type dislocations on {1 1 1}-type fcc planes is a dominant feature at all three investigated temperatures. The figure is from Ref. [25].

Nano-twinning mediated deformation mechanisms: Nanoscale twinning is another common deformation mechanism observed in both conventional and HEAs. It has been observed that mechanical twinning is more often encountered in FCC HEAs but rarely seen in BCC and HCP HEAs. Typically, the formation of twinning in FCC HEAs is associated with the glide of a/6 <1 1 2> Shockley partial dislocations on {111} habit plane [38]. In addition, these HEAs show the clear transition from planar dislocation slip to twinning when the strain reaches a critical level (as shown in Fig. 1.6) [26]. Meanwhile, other researchers suggest the existence of critical stress for twinning formation.

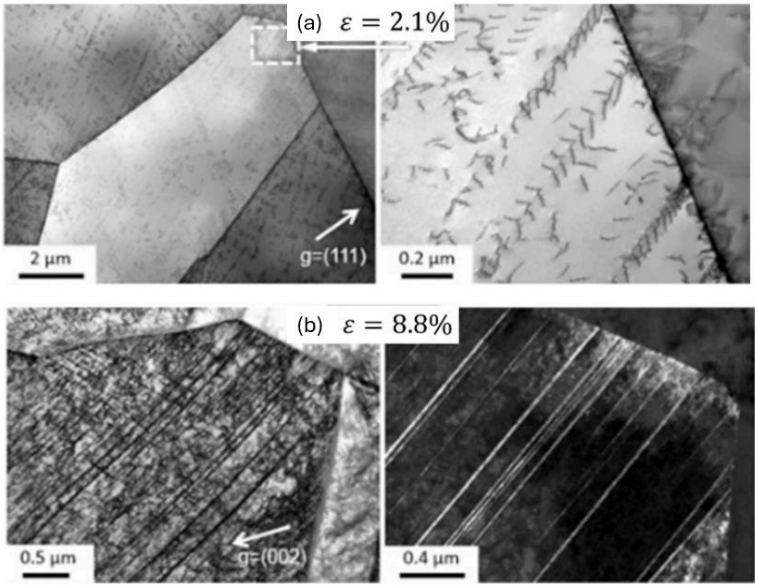

Figure 1.6 TEM observations of dislocation slip-twinning transition in NiCoFeMn at 77 K. The figure is from Ref. [26].

The critical shear stress for twining can be calculated by [39]:

$$\tau_{twinning} = \frac{\gamma}{F b_p} + \frac{k_T}{\sqrt{d}} \tag{1.7}$$

where γ is the stacking fault energy, F is the fitting constant and was determined to be 2 by Narita and Takamura [40]. b_p is the Burgers vector of partial dislocation, k_T is the Hall-Patch coefficient and d is the grain size.

Apparently, the values of stacking fault energy and grain size are two important parameters to determine the critical stress for twinning. The stack fault energy has been reported to be adjustable via varying the compositional elements. Therefore, the planer slip - twinning transition and deformation mechanisms are supposed to be controllable by adjusting the alloying elements. Liu *et al.* [41] found that the increased Co element effectively reduces the stack fault energy in NiCoFeCrMn, which promotes the twinning-mediated deformation mode. Deng *et al.* [42] also reported the decrease in Ni element can lower the stack fault energy in NiCoFeCrMn and the developed $Fe_{40}Mn_{40}Cr_{10}Co_{10}$ alloy presented the twinning-controlled deformation mode during tensile tests.

Phase-transformation mediated deformation mechanism: Recently, the promotion of plastic deformation through phase transformation-induced plasticity has also been introduced into HEAs to enhance the mechanical properties. Li *et al.* [43] reported that the quinary dual-phase $Co_{20}Cr_{20}Fe_{34}Mn_{20}Ni_6$ HEA exhibits a martensite transformation to HCP martensite phase upon tensile straining, which shows much higher tensile strength and strain hardening capacity. Meanwhile, it has also been shown that the γ (FCC phase) → ε (HCP phase) phase transformation in HEAs introduces superior fatigue resistance [44-46]. In addition, Huang *et al.* [47] successfully introduced BCC → HCP phase transformation in $Ta_xHfZrTi$ HEAs, the dynamic strain partitioning between two different phases induced significant strain hardening effect. Overall, the presence of extra phase interface introduced by phase transformation further

increases the dislocation slip resistance and the ductility is also enhanced by the increase of strain hardening ability. Similarly, the phase transformation mediated deformation mode is also adjustable via varying compositional elements, as reported in Ref. [28, 48-52].

Deformation mediated by multiple mechanisms: Beside the aforementioned deformation mechanisms, the mechanical twinning mediated deformation and phase transformation mediated deformation behaviors have been reported to be triggered simultaneously in dual phase HEAs. For instance, dual-phase $Fe_{50}Mn_{30}Co_{10}Cr_{10}$ alloy exhibits a twinning mediated deformation mechanisms in HCP phase while the martensitic transformation dominated deformation in the FCC phase [53]. This combination of persisting transformation induced plasticity and through twining deformation contributes to the continuous work hardening of HEAs without strength-ductility trade-off. Many researchers reported a novel strategy to active joint twinning – and transformation-mediated plasticity by compositional tailoring elements, in particular, by incorporating the additional interstitial C element to tune the stacking fault energy [50, 54]. The C interstitial addition in $Fe_{50}Mn_{30}Co_{10}Cr_{10}$ (at%) alloy made it present a twice tensile strength without changing the ductility when compared to single-phase HEAs [54].

1.2.3 Strengthening mechanisms in CSAs

The strengthening mechanisms during deformation of HEAs are also dependent on the crystal structure and alloying elements. Like other conventional alloys, the strength of HEAs is determined by lattice friction to dislocations, and various incremental strength mechanisms such as dislocation strengthening, grain boundary strengthening, twin boundary strengthening, phase transformation induced strengthening, precipitation strengthening and solid solution

strengthening. Several strengthening contributions often co-exist, depending on specific design strategies. It is worth mentioning that new microscopy techniques provide more atomic-level structural characterization, such as short-range ordering in FeCoNiCrCuAl, FeCoCrNi and NbMoTaW [55-58], which allows more in-depth understanding of the strengthening and deformation. Major strengthening mechanisms existing in HEAs will be discussed in detail.

Lattice friction: In CSAs, all elements are randomly distributed and intermixed over lattice sites. The mismatch of atomic radius and elastic modulus among these alloying elements introduces a strong lattice distortion and strain field around, which hinder the dislocation movement upon deformation. This effect is special for HEAs and is one of the four core effects of HEAs alloying systems, as discussed in Section 1.1.2. And it is expected that lattice resistance will be improved when the mismatch in atomic radius and modulus of alloying elements enlarge. When the lattice friction in CSAs is assumed to be uniform, the lattice friction shear stress in concentrated HEAs can be calculated based on Peierls-Nabarro's model shown below [59, 60]:

$$\tau_{friction} = \frac{2G}{1-v} exp\left(\frac{-2\pi w_d}{b}\right) \tag{1.8}$$

where G is the shear modulus, v is the Poisson's ratio, b is the Burgers vector and w_d is the width of dislocation core. It is clear that the dislocation core width is a major determinant of lattice friction, and it was found to be a constant when the principal elements exceed three. The value of $\frac{w_d}{b}$ is 0.95 ± 0.03 for the BCC alloys and 1.33 ± 0.04 for FCC alloys, respectively. It has been proven that higher order equiatomic alloys exhibit smaller dislocation width thereby higher lattice friction, which further confined the dislocation glide [59].

Solid solution strengthening: Solid solution induced hardening is critical for the excellent mechanical properties of HEAs [61]. Many models have been developed to quantitative evaluate

the strengthening effect introduced by solid solution. The Fleischer model is the very first mathematical model to describe the solid solution strengthening in metallic alloys, which considered one low-concentrated solute species to be isolation and distinguished other solutes out. This isolated solute will work as the strong pinning to dislocation glide and the source of solid solution strengthening (as shown in Fig. 1.7a). The expression of Fleischer model [62] is as follows:

$$\sigma_{ss} = \frac{MG\varepsilon_s^{\frac{3}{2}} c^{\frac{1}{2}}}{700} \tag{1.9}$$

where M is the Taylor coefficient with value of 3.06, G is the shear modulus of matrix, c is concentration of solute spices in molar fraction, ε_s is the solvent-solute interaction factor and associated with the mismatch in elastic modulus and atomic size. ε_s can be defined as:

$$\varepsilon_s = \left| \frac{\eta_{em}}{1 + 0.5\eta} - 3\eta_{am} \right| \tag{1.10}$$

where η_{em} is the elastic modulus misfit and η_{am} is the atomic size misfit. The Fleischer model is expected to validate a $\sigma_{ss} - c^{1/2}$ relationship but this relation was challenged when dealing with some HEAs, as reposted in HfMoNbTaTiZr [63], MoNbTiVZr [64] and AlHfNbTaTiZr [65].

The Labusch model [66] steps forward based on Fleischer model, which considers medium-concentrated solute atoms (typically 1-20 at %) as the strengthening contributions. Owing to relatively higher concentrations, a forest of solute atoms acts together to exert friction on dislocation movement (as shown in Fig. 1.7 b). This constant interactions with dislocation induce weak pinning in comparison to strong pinning effect by single solute atom in the Fleischer model. The Labusch model originally consisted of solid solution strengthening in binary alloys with the following expression:

$$\sigma_{ss} = 3ZG \in_{mis}^{\frac{4}{3}} c^{\frac{2}{3}} \tag{1.11}$$

where Z is a constant, G is the shear modulus, $\in_{mis}$ is the misfit parameter with respect to elastic modulus and atomic size, and c is the concentration of solute. From Eqn. 1.11, the $\sigma_{ss} - c^{2/3}$ is expected to predict the solid solution strengthening from medium-concentrated solute atoms.

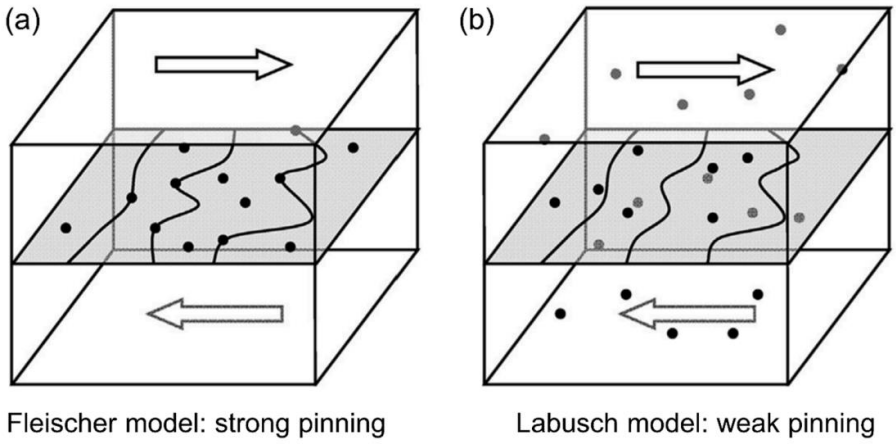

Figure 1.7 Schematics descriptions of the (a) Fleischer model and (b) Labusch model. The figure is from Ref. [67].

Recently, Varvenne *et al.* [68] proposed a predicted model to explain the solid solution induced strengthening in multicomponent alloys. In this model, each alloying element is considered the solute embedded in a matrix of surrounding atoms. In this model, lattice distortion induced by mismatch in atomic size plays a critical role in strengthening. And only elastic contribution to solute-dislocation interactions is considered. Two fundamental quantities, the zero-temperature yield stress τ_{y0} and total energy barrier ΔE_b are the determinants to evaluate solid solution strengthening, which are expressed as follows:

$$\tau_{y0} = 0.051\alpha^{-\frac{1}{3}}\mu\left(\frac{1+v}{1-v}\right)^{\frac{4}{3}} f_1(w_c) \times \left[\frac{\sum C_n\left(\Delta\bar{V}_n^2 + \sigma_{\Delta V_n}^2\right)}{b^6}\right]^{\frac{2}{3}} \quad (1.12)$$

$$\Delta E_b = 0.274\alpha^{\frac{1}{3}}\mu b^3\left(\frac{1+v}{1-v}\right)^{\frac{2}{3}} f_2(w_c) \times \left[\frac{\sum C_n\left(\Delta\bar{V}_n^2 + \sigma_{\Delta V_n}^2\right)}{b^6}\right]^{\frac{1}{3}} \quad (1.13)$$

The parameters are the same as reported in [69]: α is dislocation line tension parameter, $f_1(w_c)$ =0.35, $f_2(w_c)$=5.70. μ is the shear modulus and b is the Burger's vector.

Then the solid solution strengthening induced stress can be calculated by:

$$\sigma_{SS}(T, \dot{\varepsilon}) = M\tau_{y0}\exp\left(-\frac{1}{0.51}\frac{kT}{\Delta E_b}\ln\frac{\dot{\varepsilon_0}}{\dot{\varepsilon}}\right) \quad (1.14)$$

where M is Taylor factor with value of 3.06, k is the Boltzmann constant, T is the temperature and $\dot{\varepsilon_0}$ is the reference strain rate with value of 10000/s.

Dislocation strengthening: The plastic flow of crystalline materials during deformation is generally carried by the movement of pre-existing dislocations. And crystalline structures typically contain various slip planes, from which the dislocation interacts in different ways. One group of dislocations will act as the hinderance and pinning points for another group of dislocations from different slip planes. As a result, it requires higher applied stress to overcome this obstacle effect to maintain continuous plastic flow. The dislocation strengthening is primarily affected by density of dislocation, as described in classical Taylor hardening model [70]:

$$\sigma_{dis} = M\alpha Gb\sqrt{\rho_{dis}} \quad (1.15)$$

where M is the Taylor factor with a value of 3.06, α is a constant with an approximation as 0.2, G is shear modulus, b is the Burgers vector and ρ_{dis} is the dislocation density.

Grain boundary strengthening: The grain boundary strengthening arises from the hinderance of grain boundaries to dislocation movements. Due to the difference in grain orientations, dislocations need to deviate from initial slip plane/direction and a higher applied stress is required to penetrate the grain boundary. Furthermore, when previous dislocations are impeded at the grain boundary, the subsequent dislocation will continue to move forward but hindered by localized strain induced by previous dislocation and finally pile-up at grain boundaries. The grain boundary strengthening depends on the grain size, as proposed by Hall-Petch relation [71, 72]:

$$\sigma_{GB} = k_s d^{-\frac{1}{2}} \tag{1.16}$$

where k_s is the Hall-Petch strengthening coefficient and d is the grain size. Refined grains introduce more grain boundaries, which improves the barrier effect of grain boundaries and thereby results in the increase in the strength of materials.

Twin boundary strengthening: Although twin boundary is one type of grain boundary, twinning is often discussed separately due to its unique role in strengthening. Twinning during deformation continuously introduces additional interfaces, which act as pinning sites for dislocation movement and effectively reduce mean free path of dislocation thereby enhances strain hardening [73-76]. This process is commonly referred to as the "dynamic Hall-Petch" effect. For example, it is reported the high coherent twin boundaries ($\sum 3$ type) in CrMnFeCoNi effectively promote a high work hardening rate and enhance ductility by postponing the onset of necking [24].

Phase transformation induced strengthening: The phase transformation induced strengthening was originally found in high-strength steels and has been extended to application on HEAs to improve strength and ductility simultaneously. This is achieved by making the parent metastable phases through careful tuning of stacking fault energies by altering the chemical composition or controlling the deformation temperature. The two common types of phase transformation seen in HEAs include FCC to HCP and FCC to BCC, as reported in Refs [28, 43, 48, 77]. The enhanced strength of HEAs is due to the dynamically changing volume fraction of each phase during deformation, and improved ductility is attributed to the increase strain hardening during phase transformation.

Precipitation strengthening: Many attempts have been made to successfully improve the strength of HEAs including $Al_{0.3}CoCrFeNiC_{0.1}$ [78], $CoCrFeNiMo_x$ (x= 0, 0.1, 0.2) [79], $Cr_{15}Fe_{20}Co_{35}Ni_{20}Mo_{10}$ [80], FeCoNiCr [81] etc. Among these, $(FeCoNiCr)_{94}Ti_2Al_4$ is one of the most investigated precipitation-hardened HEAs, which introduces coherent nanosized L12-Ni3(Ti, Al) precipitates by aging and quenching [82]. The strengthening mechanism is explained by the shearing mechanisms (Fig. 1.8a) that the particle-matrix coherency and mismatch in modulus result in strengthening. This type of strengthening typically occurs in materials with small, coherent precipitates and quantitative evaluation of stress induced by precipitation hardening can be expressed as [82]:

$$\sigma_{pre} = M\alpha_{\varepsilon}(G\varepsilon_a)^{\frac{3}{2}}\left(\frac{rf_P}{0.5Gb}\right)^{\frac{1}{2}} \tag{1.17}$$

where $M = 3.06$ is the Taylor factor, α_{ε} is 2.6 for FCC structure, G is the shear modulus of matrix material, ε_a is the constrained lattice parameter mismatch, r is the particle radius, f_P is the volume fraction of the precipitates, b is the Burgers vector.

When the precipitates are large, incoherent and have a significant mismatch in modulus with the matrix, dislocations prefer to circumvent the precipitates instead of cutting through them. Dislocations bow out between precipitates and leave dislocation loops around the precipitates, which requires additional energy and contributes to strengthening (Fig. 1.8b). The contribution form this Orowan bow-out mechanism is calculated by [83]:

$$\sigma_{orowan} = 0.4MGb\frac{1}{\pi\sqrt{1-v}}\frac{\ln\left(\frac{2\bar{r}}{b}\right)}{\lambda} \tag{1.18}$$

where M the Taylor factor, G is the shear modulus, b is the Burger's vector, v is the Poisson's ratio, $\bar{r}$ is the mean particle radius and λ is the mean inter-particle spacing.

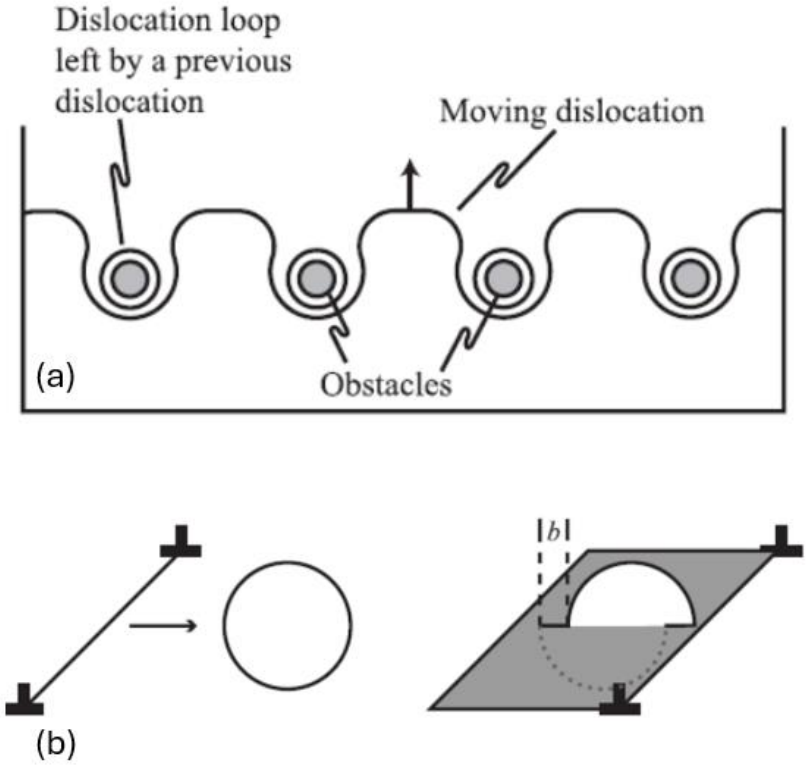

Figure 1.8 Schematic descriptions of precipitation hardening mechanisms. (a) shearing mechanism. (b) bow-out mechanism. This figure is from Ref. [84].

With respect to strengthening mechanisms in concentrated HEAs, the primary differences are the lattice resistance to dislocation movement, solid solution strengthening and unique short-range ordering when compared to conventional dilute alloys. The severe lattice distortion in HEAs due to mismatch in modulus and atomic size renders resistance to dislocation motion and induces strong hardening effect. Complex alloying and ambiguous boundary between solvent and solute atoms complicate the investigation on solid solution strengthening mechanisms in HEAs. More efforts are needed to predict and quantify the solid solution induced hardening in HEAs.

1.2.4 Radiation response of CSAs

The compositional complications in thermodynamically stable CSAs allows tunable properties by modifying alloying elements [85-87]. which makes CSAs promising candidates for structural materials at extremes of high temperature, radiation, etc. [88, 89]. Studies focus on the defect nucleation and accumulation, phase stability, void swelling, and radiation-induced segregation.

Early-stage radiation damage: The early-stage radiation damage are generally point defects, generated from displacement cascades and defect migration [90]. These point defects lead to microstructural defects, such as voids, precipitates and other complex clusters. Therefore, understanding the mechanisms of nucleation and accumulation of radiation-induced defects in this nascent stage is crucial. Regarding defect nucleation, recent studies [90, 91] indicate that the chemical complexity in Ni-based CSAs suppress the defect accumulation through enhancing vacancy-interstitial recombination at early stages of irradiation [92]. This may be ascribed to the

reduced electron free path and electrical and conductivity of CSAs [88, 93]. On the other hand, sluggish diffusion has been claimed by Granberg *et al.* [94, 95], lowering defect production. Lu *et al.* [96] presented a direct evidence that the defect clusters in Ni distribute in a larger depth than in Ni-based CSAs, which suggests a significantly lower defect mobilities. In addition, both experimental and simulation work studies [94] demonstrate more but smaller defects in Ni-based CSAs when compared to those in pure Ni. This sluggish defect diffusion is attributed to the more severe lattice distortion in CSAs, which could restrain the defect movement in CSAs. More generally, the characteristics in CSAs including lattice distortion, sluggish diffusion, chemical complexity and solid-solution effect contribute to the influence on defect evolution and migration.

At higher radiation dose and/or elevated temperature, point defects results in accumulation of vacancy- and interstitial-type clusters, solute segregation at grain boundaries and defects, void swelling, and phase instability, which seriously degrade the mechanical performance and shorten the lifetime.

Void swelling: When the work temperature reaches between 0.3 and 0.6 of absolute melting temperature, the growth of voids will accelerate and consequently cause pronounced volume swelling. In this case, swelling resistance under elevated temperature irradiation is crucial to maintain the performance of structural materials for advanced nuclear reactors. Lu *et al.* [89] investigated void swelling resistance of several Ni-based CSAs subjected to 3 MeV Ni ion irradiation at 500°C and discovered that the quinary NiCoFeCrMn exhibited relatively lower void swelling of ~0.02% when compared to ~ 1.8% in pure Ni. In pure Ni, interstitial clusters migrate in one direction from the high-dpa region to deeper low-dpa region, which leaves high concentrations of voids at high-dpa area. In contrast, in CSAs, interstitial defects typically

exhibit a random 3D migration behavior, which inhibits the accumulation of defects and instead facilitates the interstitial-vacancy annihilation. The other interesting study was done by Jin *et al.* [97] using optical profilometer to directly measure the volume swelling of Ni and Ni-based CSAs subjected to ~ 53 dpa of radiation damage at 500°C. NiCoFe and NiCoFeCrMn show the lowest volume swelling of less than 0.2% when compared to Ni that has volume swelling greater than 6%. They also concluded that Fe is the more effective element in retaining the swelling resistance. From the above results, CSAs present better radiation-induced swelling resistance, which is not solely determined by the number of alloying elements but influenced by the intrinsic properties of alloying elements.

Phase stability: The phase stability of some Ni-based CSAs have been examined and no obvious secondary phase was observed in NiCoFeCr and $NiCoFeCrAl_{0.1}$ alloys even under ~100 dpa radiation dose exposure at room temperature [98, 99]. CSAs including NiFe, NiCoFe, NiCoFeCr, NiCoFeCrMn also exhibit great stability without secondary phase formed under ion irradiation even at elevated temperatures [100]. Kumar *et al.* [101] also found no phase transformation and decomposition occurred in irradiated NiFeMnCr (~ 10dpa) at various temperature range between room temperature up to 700°C. However, He *et al.* [100] found that electron-irradiated NiCoFeCrMn and NiCoFeCrMn present NiMn-type ordering decomposition and spinodal decomposition even at a very low dose. These results suggest that the phase stability of CSAs at elevated temperatures is also affected by the irradiation conditions.

In summary, aggressive conditions such as high dose and elevated temperature typically accelerate the evolution of defects with respect to thermodynamic and kinetics. Structural damages in this case present complexity include accumulation of defects, void swelling, radiation-induced segregation and phase instability. Extensive studies on Ni-based CSAs have

shown that not only amount of alloying elements but intrinsic properties of alloying elements determine the resistance of CSAs to radiation damage and mechanical performances. Most importantly, the underlying mechanisms are still not well understood and both experimental and simulation work are ongoing.

1.3 Nanomechanical characterizations on surface properties

To date, numerous efforts to develop advanced structural materials focus on characterizing and understanding the mechanical behavior of materials from both fundamental and practical perspectives [2]. The invention of instrumented nanoindentation made significant advances in the fundamental understanding of mechanical behaviors of materials at micrometer and nanometer scales, especially inside scanning and transmission electron microscope. This precise probing capability of nanoindentation technique is especially important for characterization of thin films [102-104] and surface-modified materials (e.g., ion-irradiated materials and laser melted materials [97, 105-108]), of which the mechanical property measurement cannot be achieved by traditional mechanical tests (e.g., tensile tests) due to limited volume [109-111].

1.3.1 Nanomechanical studies of high-entropy alloys

This part of the review mainly focuses on the study of the mechanical behavior of HEAs at microscale and nanoscale levels. Fig. 1.9a shows the structural defects and dislocation systems from macroscopic to the nanometer scale [112, 113]. Nanomechanical techniques have been successfully applied to explore novel performance of HEAs by nanoindentation, micropillar

compression, microcantilever bending, micro-tensile tests, which often sit inside scanning electron microscope (SEM) and transmission electron microscope (TEM), as outlined in Fig. 1.9b [114-117]. It is worth mentioning that insight into the nucleation and propagation of dislocations and defects at the nanoscale is a critical research aspect of nanoindentation-based characterization [118].

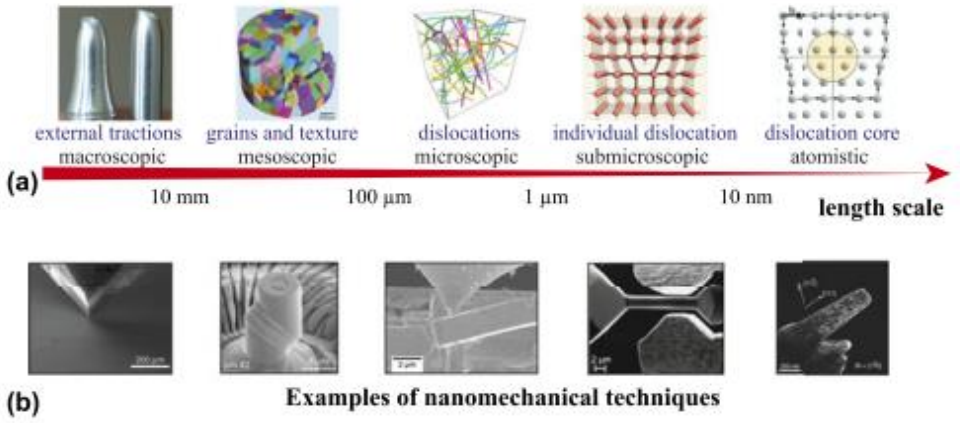

Figure 1.9 (a)the length scales related to structural defects and dislocation systems span from the micrometer down to the nanometer scale. (b) examples of commonly used nanomechanical techniques: nanoindentation, micropillar compression, microcantilever bending, micro-tensile tests, and nanopillar compression (from left to right). These images are from Ref. [119].

Table 1.1 [119] summarizes the various studies of HEAs using different nanomechanical methods. It illustrates various types of HEAs covering single crystal, nanocrystalline and coarse-grained structures as well as their properties including incipient plasticity, strain rate sensitivity, fracture toughness and creep property.

Table 1.1 A summary of recent experimental results of HEAs studied by various mechanical techniques.

Method	Mode	Structure	HEAs	Properties
Nanoindentation	Different loading rates	Fcc	FeCoCrMnNi (cg)	Incipient plasticity
Nanoindentation	Different loading rates	Bcc	TiZrHfNb (cg)	Incipient plasticity
Nanoindentation	Different indenter tips	Fcc	FeCoCrMnNi (cg & nc)	Annealing effect
Nanoindentation	Strain-rate jump	Fcc	FeCoCrMnNi (cg & nc)	SRS, activation volume
Nanoindentation	Holding	Fcc	FeCoCrMnNi (cg & nc)	Creep property
Nanoindentation	Wear & friction	Bcc	TiZrHfNb (cg)	Wear rate, COF
Microcompression	Micropillars	Fcc	FeCoCrMnNi (cg)	Size dependence of strength
Microcompression	Micro/nanopillars	Fcc & bcc	$Al_{0.8}$CoCrCuFeNi; $Al_{0.7}$CoCrFeNi (cg)	Strength; size dependence
Microcompression	Micropillars	Bcc	NbMoTaW (sx)	Size dependence of strength
Microcompression	Micropillars	Bcc	NbMoTaW (nc)	Size dependence of strength
Microcompression	Strain-rate jump/ High-temperature	Bcc	NbMoTaW (sx & nc)	Size effect, SRS, activation volume
Micro straining	In situ TEM	Fcc	FeCoCrMnNi (cg)	Fracture mechanism
Microcantilever bending	In situ TEM	Bcc	NbMoTaW (sx and cg)	Fracture toughness grain boundary effect
Nano-lattice compression	In situ SEM	Fcc	$CoCrFeNiAl_{0.3}$ (nc/composite)	Fracture behavior

* cg is the coarse grains, nc is the nanocrystalline, and sx is the single crystal. This table is from Ref[119].

Lastly, nanoindentation has also been tried to investigate more materials properties. For examples, wear resistance of laser-cladded FeNiCoAlCu HEA coatings has been studied by nanoindentation by Jin *et al.* [120], suggesting the friction coefficient decreased from the range of 0.8-0.9 to approximately 0.3 even above 600°C; Spherical nanoindentation has been used to examine the impact of grain size on the creep performance of the single-phase CoCrFeMnNi high-entropy alloy (HEA) at room temperature by Lee *et al.* [121]; Nanoindentation is also used to investigate temperature dependent creep behavior, considering the influence of grain orientation and solid solution in the CoCrFeMnNi and dual-phase $Fe_{18}Co_{18}Ni_{20}Cr_{18}Mn_{18}A_{l8}$ HEAs across the temperature range of 300-600 °C by Tsai *et al.* [122].

1.3.2 Advancement of nanoindentation techniques

In the early 1900s, Brinell [123, 124] conducted the first indentation tests using spherical and smooth balls from ball bearings as indenters to assess the plastic properties of materials. This testing technique constrains a minimum length scale for the indentation and necessitates optical imaging of the indentation. Towards the close of the previous century, advancements in instrumental design, primary data correction techniques, and digital technologies for processing and storage facilitated the modernization of the concept of continuously recording the P-h diagram during the process of loading and unloading the indenter [125]. The core of the nanoindentation involves testing setups equipped with accurate force actuators and displacement sensors that capture the force-displacement profile. For measurement process, the pyramidal or spherical diamond indenter is inserted and removed from a small area on the surface of to obtain the associated raw data [126]. In the last two decades, indentation testing has been expanded to the nanometer scale, primarily through the advancement of instrumentation [125]. In certain exceptional scenarios, the resolution for indenter displacement can attain values as low as tenths or even hundredths of nanometers. At the same era, the capacity for nanoindentation measurements at elevated temperatures has also undergone significant development [127]. Presently, commercially available systems can carry out stable indentation testing at temperatures of up to 800°C. The latest instruments can measure not just the normal load gauged on the indenter, but also the lateral force that arises when the indenter is moved in relation to the surface of the sample. Besides, the latest electronics advancements have repromoted the development of high strain rate nanoindentation test equipment [128]. Table 1.2 [125] summarizes various testing modes involved in nanoindentation and associated main features, including load control mode, strain rate test, creep test and nano scratching mode.

Table 1.2 Main testing modes are involved in nanoindentation. The table is from Ref. [125].

Mode name	Main features
Load-controlled (LC) mode/test	$\dot{P} = \text{const}$, $\dot{\varepsilon} \neq \text{const}$
Constant strain rate (CSR) mode/test	$\dot{\varepsilon} = \text{const}$; $\dot{\varepsilon} \approx \dot{P}/2P$
Continuous stiffness measurement (CSM) mode	Harmonic load $P_{osc} = P_a \sin(2\pi f)t$ at $P_a \ll$ P in addition to the main load and synchronous detection of displacement $h(t) = h_a \sin(2\pi f - \varphi)t$
Strain rate jumping (SRJ) mode	A set of discrete $\dot{\varepsilon}$ values ($\dot{\varepsilon}_1, \dot{\varepsilon}_2, \dot{\varepsilon}_3, \ldots$) in one loading–unloading cycle
Step load and hold (SLH) mode/test	Rapid jump of force up to $P = \text{const}$
Creep	$P = \text{const}$
Nanoscratching (NS)	Simulation of friction and wear at the level of a single nanocontact at given values of P_N and the lateral velocity of the probe

In-situ nanomechanical testing has also been quickly developed with the purpose of real-time imaging of deformation processes establishing correlations with load-displacement curves obtained through measurement. Rabe *et al.* [129] reported one of the earliest examples of an in-situ SEM nanoindentation system and further refinements were made to enable a more detailed examination of the process of shear-band formation [130, 131].

1.3.3 Current challenges on nanomechanical study

Size effects occurring at the nanoscale are the significant category of phenomena that form the foundation of nanoscience and nanotechnology. The key challenge in the field of nano mechanics is to uncover the phenomenological laws governing size effects and atomic mechanisms that affect the physical and mechanical properties of material due to scale factors. The map in Fig. 1.10 [125] schematically demonstrates the size dependence of τ/G (shear stress normalized to shear modulus) upon characteristic size R of five different magnitudes (from nanoscale to macro scale). Size effect increases as the sample dimension decreases and becomes prominent once certain critical dimensions are reached. In particular, the mechanical properties

of materials may differ significantly at the nanoscale compared to the bulk scale. This can lead to inaccurate measurements and make it difficult to predict the behavior of materials in real-world applications.

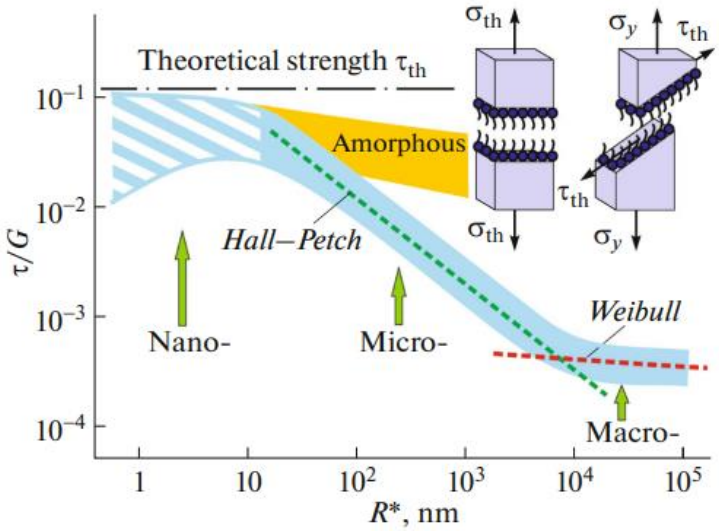

Figure 1.10 Schematic map shows the size dependence of flow shear stress to shear modulus upon characteristic size for five orders of magnitude. Inset presents a diagram of theoretical strength. This figure is from Ref. [125].

Versatility and ease of nanoindentation makes it popular to be employed to extract the local mechanical properties of materials. There is also a paradox in various mechanical testing techniques for miniaturized samples regarding the ease of sample preparation and data analysis (as shown in Fig. 1.11 [132]). Tensile and compression test are the most straightforward ways to directly obtain the mechanical properties including elastic modulus, yield/ultimate strength, and ductility. However, sample preparation requires the use of the Focus Ion beam technique. In contrast, nanoindentation technique is capable of collecting desired information in a relatively high-throughput manner. Nanoindentation typically does not require specific sample preparation and batches of tests can be conducted within a short period of time. But the common limitation

of nanoindentation is the complication of data analysis because the extraction of mechanical performance from nanoindentation needs aids with proper analytic models.

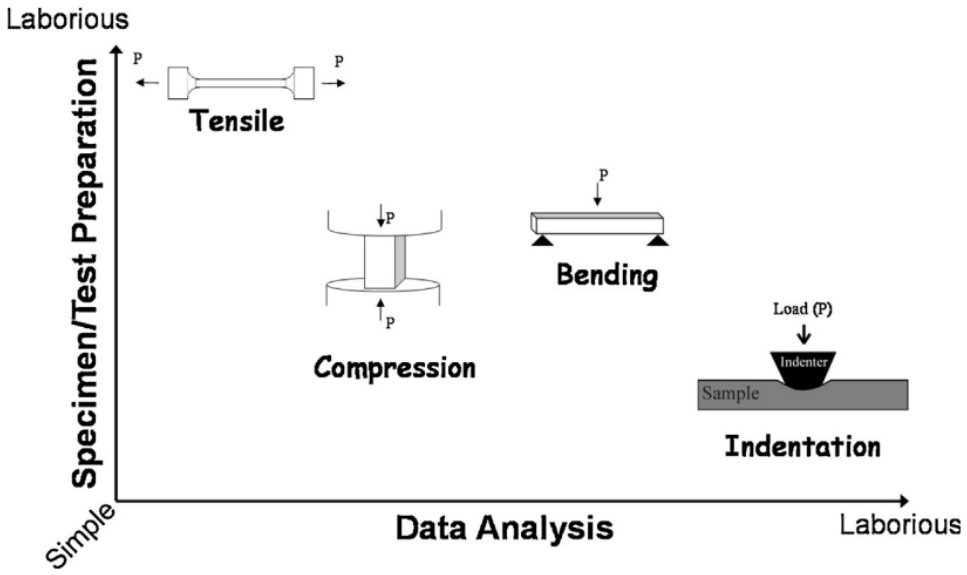

Figure 1.11 Various mechanical testing methods for micron to sub-micron length samples. This figure is from Ref. [132].

1.3.4 Specific challenges in nanoindentation

Nanoindentation also has the advantages of easy sample preparation and statistically rich data sets. However, when nanoindentation is applied to investigate the mechanical performance of materials, indentation size effect intrinsically makes nanoindentation overestimates the hardness values. Extrinsically, penetration of sharp indents usually induces severe pile up/sink in around indents [133]. And other external factors like surface preparation and thermal drift also influence the measurement. These effects significantly affect the measurement accuracy of nanoindentation and further complicate the post-data analysis.

Indentation size effect: An increase in yield strength or flow strength are frequently observed when the size of test specimen is reduced to dimensions of micrometer and nanometer

scale. This occurs when the dimensions of the specimen approach the average spacing between dislocations and when plastic deformation is governed by a restricted number of defects. Likewise, indentation testing exhibits scale-dependent behavior when the size of the hardness impression is small. Indentation size effect (ISE) is commonly observed in materials that are indented using geometrically self-similar indenters such as pyramids and cones (as shown in Fig. 1.12).

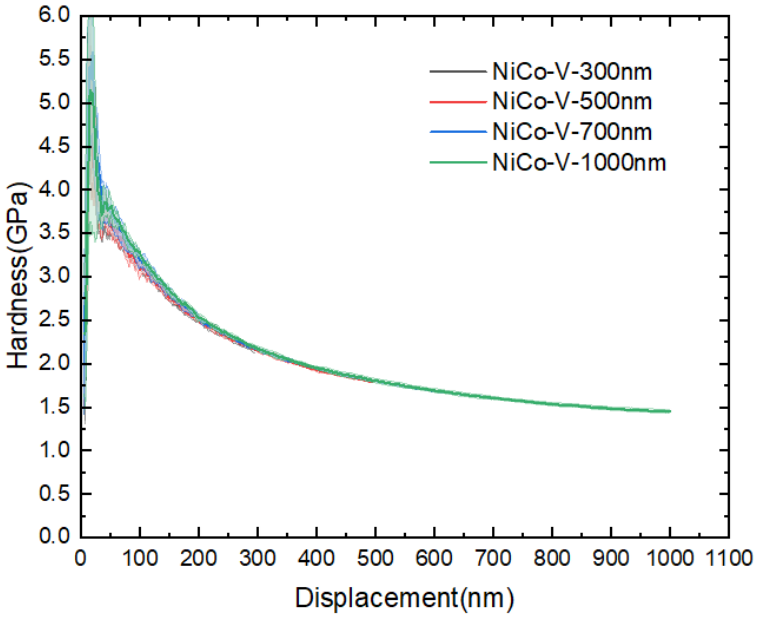

Figure 1.12 Nanoindentation on NiCo sample with pyramidal indenter that shows clear indentation size effect.

McElhaney *et al.* [134] demonstrated a significant ISE of Cu sample, whose hardness measured increases more than a factor of two from 1μm to 100nm. This deviation makes nanoindentation measurement with potential for misleading results. The higher hardness close to surface could be attributed to various reasons, including the quality of sample surface preparation, heterogeneous surface layer and ISE. Numerous mechanistic models have been established to explain the ISE and the most widely used is Nix-Gao model [135]. The

fundamental principle of the model is that geometrically necessary dislocations (GNDs) form in addition to the statistically stored dislocations (SSDs) created during uniform straining, resulting in an additional hardening component (as shown in Fig. 1.13 [136]).

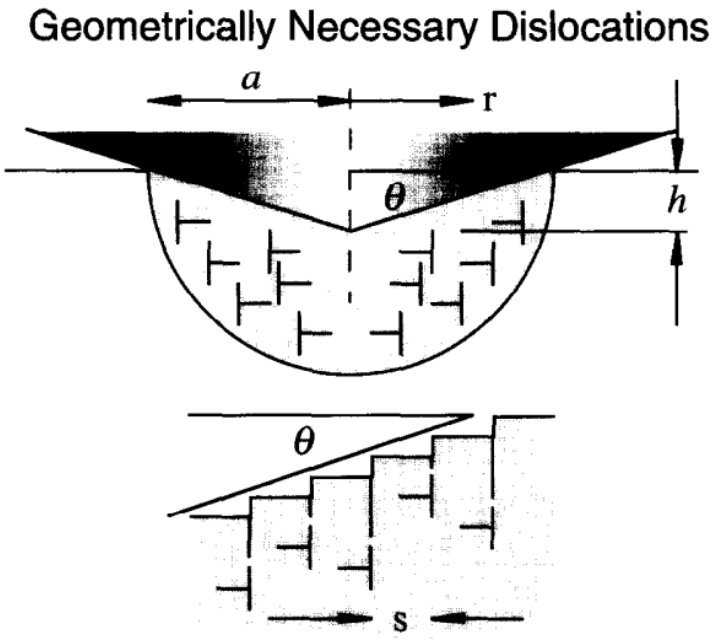

Figure 1.13 Dislocations created by a rigid conical indentation. It is idealized as circular dislocation loops. The figure is from Ref. [136].

The density of GNDs is inversely proportional to the depth and increases significantly when then penetration depth is shallow. Mathematically, Nix-Gao model can be expressed as:

$$H = H_0 \sqrt{1 + \frac{h^*}{h}} \tag{1.19}$$

where H_0 represents the macroscopic hardness that is asymptotically approached at the large depth. $h^*$is the characteristic depth below which the extra hardening becomes significant.

The remarkable linearity of fitting curves for (111) single-crystal Cu [134] and (110) single crystal Ag [137] provide primary evidence for validity of Nix-Gao model, as shown in Fig. 1.14.

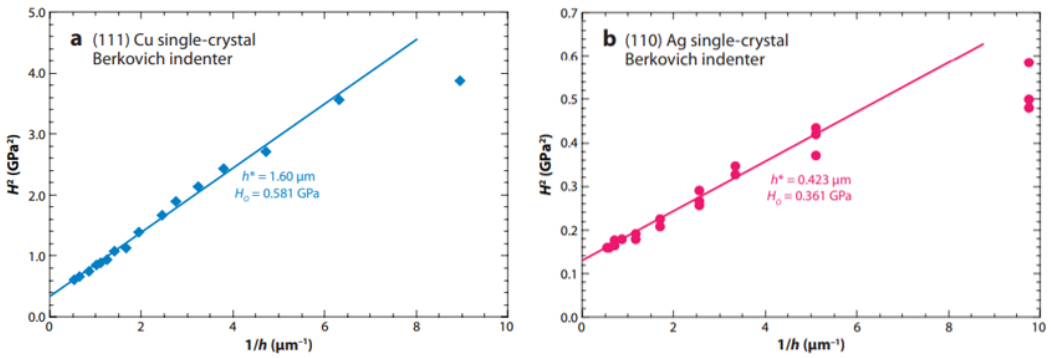

Figure 1.14 (a) the plot of H^2 versus 1/h for (111) Cu and (b) the fitting result of (110) Ag both obtained in nanoindentation experiments with the Berkovich indenter. The figure is from Refs. [134, 137].

However, the Nix-Gao model does have disadvantages although it is widespread applied. Some have received a great deal of attention:

- The linear behavior of Nix-Gao model deviated significantly at smaller penetration depth and liner extrapolation would considerably overestimate the value of H_0.
- The Nix-Gao model assumed the radius of hemispherical zone to accommodate GNDs is equal to the radius of the contact impression. Swadener *et al.* [138] argued that this model is mathematically tractable but artificially established, it ignores crucial physical processes that determine the size of accommodation zone.

Contact area determination: The computation of contact area used to determine hardness is another challenging aspect of nanoindentation methods. Ideally, the sample surface was assumed to be perfectly flat, area function of a known-shape indenter can be determined with the

penetration depths and contact stiffness. However, if the surface is rough at the contact dimension scale, the contact area determined using this method can be significantly erroneous [139]. Besides the influence of roughness, the occurrence of pile up/sink in around indents is another critical issue affects the determination of real contact area as shown in Fig. 1.15 [140]. The pile up/sink in would underestimate/overestimate the contact area thus overestimate or underestimate the hardness. Thus, more optical examination needs to be utilized to calculate the actual contact area, which critically complicates the data processing.

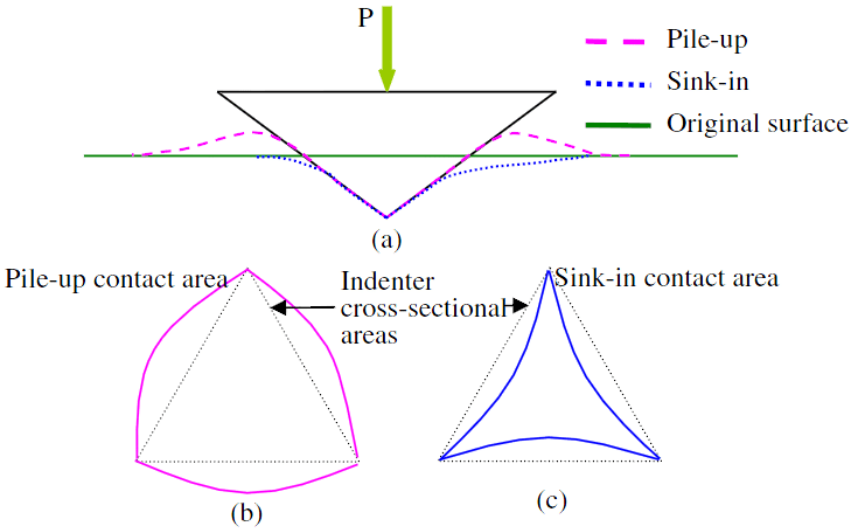

Figure 1.15 (a) schematic demonstration of pile-up and sink in during nanoindentation. (b) contact area of pile up (c) contact area of sink in. These figures are from Ref. [141].

Effect of sample preparation: Nanoindentation does not require high-cost techniques to prepare sample but asks for high-quality surface preparation. These are three main factors that affect the accuracy of nanoindentation measurements [142]: surface contamination on the surface including oxide layer and organic layer, surface roughness and mechanical damage from sample preparation. Contaminants can be cleaned, and experiments should be conducted in an environment free of contaminants and oxidation. Roughness of sample surface is a critical factor

in determining the contact of point and contact mechanics. This effect generally brings additional complications in data analysis and results in increased scatter in date points. Finally, the mechanical damaged layer introduced by polishing also leads to inaccuracy of measurement. Liu and Ngan's study [143] compared the effect of mechanical polishing and electropolishing on data collection from nanoindentation on (111) Cu, it was found that electropolishing reduced the ISE.

Thermal drift: It refers to change in instrument resulting from the temperature variation during the testing. The thermal drift rate is typically a few nm/second over a cycle of test period but can result in large errors in the acquisition of load-displacement curves. Because the depth sensor of indentation is at the same level as length scale. These errors directly affect the measurement of modulus and hardness measurements. The thermal drift could be mitigated by controlling the testing environment. Meanwhile, once the drift rate is calculated from depth sensor, it can be corrected manually. This procedure is theoretically reasonable but not straightforward to utilize practically especially the thermal drift is dynamic throughout the test.

1.4 Research motivations and hypotheses

CSAs, with a huge material design space, have created a wave of research to explore new materials for better property combinations (e.g., simultaneous mechanical properties and radiation tolerance) that cannot be achieved by conventional alloys. Due to the large material design space and newly discovered mechanisms of deformation and radiation response (e.g., lattice distortion and sluggish diffusion), the acceleration of new alloy development requires fast property evaluation methods and fundamental understanding to guide the material design for aerospace and nuclear industries. Therefore, this thesis includes both nanoindentation

methodology development and the study of the role of alloying effects in deformation mechanisms and radiation tolerance.

We select Ni-based CSAs with the addition of 3d transition metal elements including Co, Cr, Mn, and Fe as the focus as these elements have shown effective modification of electron band structure and promising property improvement. This includes a broad spectrum of CSAs, Ni, NiCo, NiFe, $Ni_{80}Cr_{20}$, $Ni_{80}Mn_{20}$, and NiCoFeCr. More specifically,

(a) We first develop nanoindentation methodologies to accurately obtain the hardness, modulus, and strain rate sensitivities of various CSAs. As such, the role of alloying effects on deformation mechanisms is investigated and we hypothesize that the type of elements is more important than the number of elements.

(b) Second, we develop a procedure to understand and quantify the early-stage radiation damage in Ni-based CSAs by nanoindentation. It has been a long-standing challenge to quantify radiation-induced defects at low dose regimes due to the difficulties in quantitatively measuring point defect population and dislocation density. It is hypothesized that the amount of low-dose radiation damage in different alloys near the surface can be correlated to the radiation-induced hardening and indentation size effect (ISE).

(c) Third, the uniaxial stress-strain curve provides more information for mechanical behavior, such as yielding strength and work hardening. We hypothesis that flat-punch nanoindentation will provide an opportunity to exact surface stress-strain curve as the contact area is fixed and the change in deformation volume is less for flat punch geometry. Moreover, combined with Berkovich and flat punch nanoindentation, the radiation-induced hardening and work hardening are compared in different alloys with different radiation damage.

CHAPTER 2 : EXPERIMENTAL

2.1 Fabrication and preparation of Ni-containing concentrated solid solution alloys

The design and fabrication of a series of concentrated solid solution alloys were accomplished in Oak Ridge National Laboratory. Ni-based single-crystal concentrated solid solution alloys including pure Ni, binary $Ni_{80}Cr_{20}$, $Ni_{80}Mn_{20}$, NiCo, NiFe (with 20 at.% Cr, 20 at.% Mn, 50 at.% Co and 50 at.% Fe, respectively) and quaternary NiCoFeCr were prepared by arc melting the high-purity (>99.9% pure) Ni, Co, Fe, Cr and Mn starting materials. The ingots were flipped and remelted five times to ensure homogeneity before drop casting to mold. The growth of single crystals from drop-cast ingots were controlled by the floating-zone furnace, where the diameter of molten zone was reduced to prevent grain propagation [144]. ~ 1mm-thick discs were cut normal to <100> crystallographic direction using the electro-discharge machine (EDM). Prior to irradiation, all specimens were mechanically ground by using SiC sandpaper up to #4000 grit size, followed by a careful electro-chemical polishing with 0.05 um colloidal silica suspension to eliminate the damage layer from EDM machining. Finally, “mirror-like” surfaces were achieved with roughness below 3nm. And NiCo, NiFe, $Ni_{80}Cr_{20}$ and NiCoFeCr samples have been confirmed as (100) single-crystal FCC structure with eminent crystal imperfections. $Ni_{80}Mn_{20}$ has a polycrystalline FCC structure with an average grain size of 100 – 200 μm [145], in which the grain boundary effects are negligible. Fig. 2.1 below shows buttons of five samples after careful polishing.

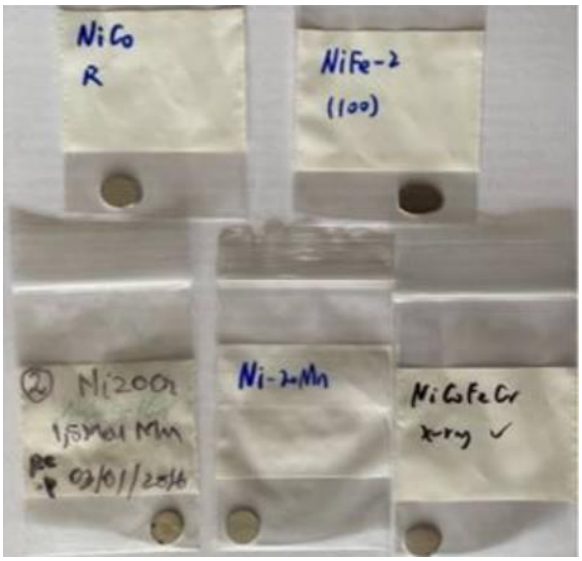

Figure 2.1 Buttons of NiCo, NiFe, $Ni_{80}Cr_{20}$, $Ni_{80}Mn_{20}$ and NiCoFeCr after careful polishing. All specimens present "mirror-like" surfaces.

2.2 Ion irradiation

The irradiation process was accomplished at the Ion Beam Materials Laboratory (IBML) at the University of Tennessee in partnership with the Oak Ridge National Laboratory (Fig. 2.2) [146].

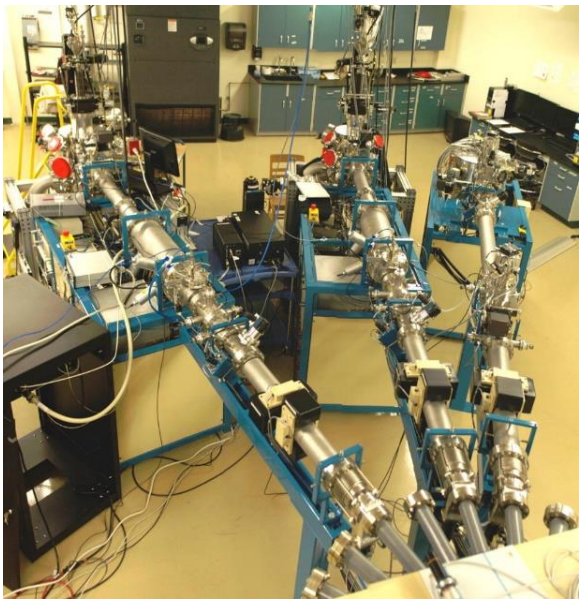

Figure 2.2 Photographs of ion irradiation beamlines at the Ion Beam Materials Laboratory (IBML) at the University of Tennessee [146].

These single specimens were irradiated with 8 MeV Ni ions under ambient temperature. The ion fluences were 1×10^{12} cm^{-2} , 5×10^{12} cm^{-2} , 2.5×10^{13} cm^{-2} , 1×10^{14} cm^{-2} and up to 5×10^{14} cm^{-2}. The samples were partially covered by TEM grids during ion irradiations to let a portion of the sample surface was exposed to irradiation (as shown in Fig. 2.3). Using this method, five irradiated regions with different ion influences were made in one sample as shown in Fig. 2.3 below. The un-irradiated region without irradiation was kept for reference and #1-#5 regions were irradiated with ion influence from 1×10^{12} cm^{-2} to 5×10^{14} cm^{-2}, respectively.

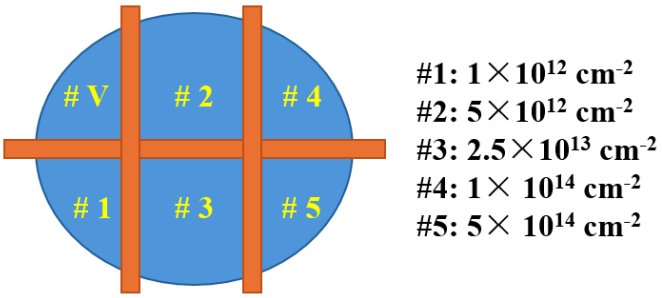

Figure 2.3 Sample arrangements for ion irradiations: total 6 portions with different radiation exposure conditions. #V is the un-irradiated portion for reference.

The corresponding damage profiles of radiation dose and implanted ion distribution were estimated by using Stopping and Range of Ion in Matter (SRIM) software. Full cascade option was employed with 40 eV as the threshold displacement energy and *vacancy.txt* was used to calculate the radiation dose in the unit of displacement-per-atom (dpa) by:

$$dpa = D\left(\frac{1}{\text{Å}}\cdot \text{ion}\right)\times\frac{ion\ fluence\left(\frac{ions}{cm^2}\right)}{N\left(\frac{atoms}{cm^3}\right)} \tag{2.1}$$

where D is the displacement estimated from SRIM calculation and N is the density. Meanwhile, the implanted Ni ion concentration can also be calculated by:

$$Ni\% = Ni\left(\frac{atom}{\text{cm}} \cdot \text{ion}\right) \times \frac{ion\ fluence\left(\frac{ions}{cm^2}\right)}{N\left(\frac{atoms}{cm^3}\right)} \tag{2.2}$$

A representation of radiation dose profile at 1×10^{14} cm^{-2} fluence is displayed in Fig. 2.4.

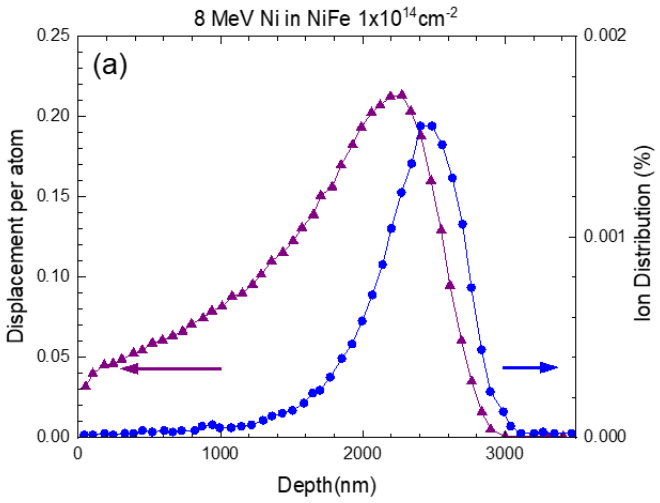

Figure 2.4 SRIM predicted profile for radiation damage (purple) and implanted Ni ion distribution (blue) of NiFe sample.

2.3 Microstructural characterizations: SEM and TEM

SEM-EDS (JEOL 6180, Oxford Xplore): Scanning Electron Microscopy is a powerful tool to probe the structure of materials and produce high resolution images of the surface of materials and study morphological evolution. Secondary electron (BE) and backscattered electron (BSE) modes are widely used in SEM. In SE imaging, the SEM detects low-energy secondary electrons emitted from the top few nanometers of the specimen's surface. Due to this characteristic, SE mode tends to emphasize surface topography and texture. In BSE imaging, the

SEM detects higher-energy electrons that are backscattered from the specimen because of collisions between the incident electron beam and atoms in the specimen. BSE is more sensitive to variations in atomic variation and elements with higher atomic number tend to backscatter more electrons. BSE imaging mode is particularly useful in studying compositional variations, phase distributions and elemental contrasts although it provides lower resolution compared to SE imaging mode. In addition, the energy-dispersive X-ray spectroscopy (EDS) detector can detect the characteristic X-rays emitted by a specimen when bombarded with electrons in the SEM. The characteristic energies are unique to each element, which enables the identification and quantification of elements present in the specimen.

EBSD: Electron backscatter diffraction (EBSD) is a powerful technique to analyze crystallographic orientation and phase information at the microscopic level. A scanning electron microscope is used to generate the high-energy electron beam directly onto the surface of polished sample. EBSD detector collects and records the characteristic diffraction patterns produced by backscattered electrons, which contains the cryptographic orientation and phase information.

TEM (JEOL 2100): Transmission electron microscopy can provide both morphological and crystallographic information of materials at micro and nano scales (as shown in Fig. 2.5). Bright filed and dark field modes are two common modes in imaging function of TEM. The contrast during imaging arises from differences in the interaction of transmitted electrons with the specimen. The first type is the mass-thick contrast which arises from variations in mass and thickness of specimen. Regions of heavy elements or denser structures appear dark and meanwhile thicker regions of specimen attenuate more electron beam, resulting in darker area in the image. The second type of contrast originates from diffraction, because crystals satisfy the

Bragg reflection conditions to varying degrees, imaging with a transmitted beam or some kind of diffracted beam also produces contrast differences. Finally, the phase of the electron wave passing through the specimen contributes to contrast differences. Phase shifts caused by variations in refractive index or thickness produce changes in interference patterns, resulting in contrast variations in the image. Selected area diffraction pattern in TEM can provide crystallographic information based on Bragg's law. Selected-area diffraction (SAD) patterns of single crystals generally present scattered points, polycrystalline materials typically contain a couple of rings and amorphous materials demonstrate diffusive rings.

Figure 2.5 TEM (JEOL 2100) installed in UNC Charlotte

2.4 Surface topography imaging

Atomic force microscopy (AFM) is widely used for imaging the topography of sample surface with nanoscale resolution, which can investigate surface features like steps, terraces, and roughness. AFM generally operates on the principle of scanning sharp probes over the sample

surface and measuring the interaction forces between the tip and the sample to produce high-resolution images of surface topography. AFM assembles the sharp tip attached to a flexible cantilever and tip typically has a radius in the order of nanometers, which allows for imaging at the atomic scale. The cantilever serves as a spring-like mechanism and deflects in response to the interaction force between the tip and sample. AFM can operate in main three modes including contact mode and tapping mode. In contact mode, the tip continuously contacts with the sample surface whereas the tip oscillates close to the surface in the tapping mode.

2.5 Berkovich indentation

The surface mechanical properties including hardness and elastic modulus were obtained from Agilent Nanoindenter G200 (MTS) with a Berkovich diamond tip (Fig. 2.6). The continuous stiffness measurement (CSM) method proposed by Oliver and Pharr was selected to record hardness and elastic modulus in a continuous way.

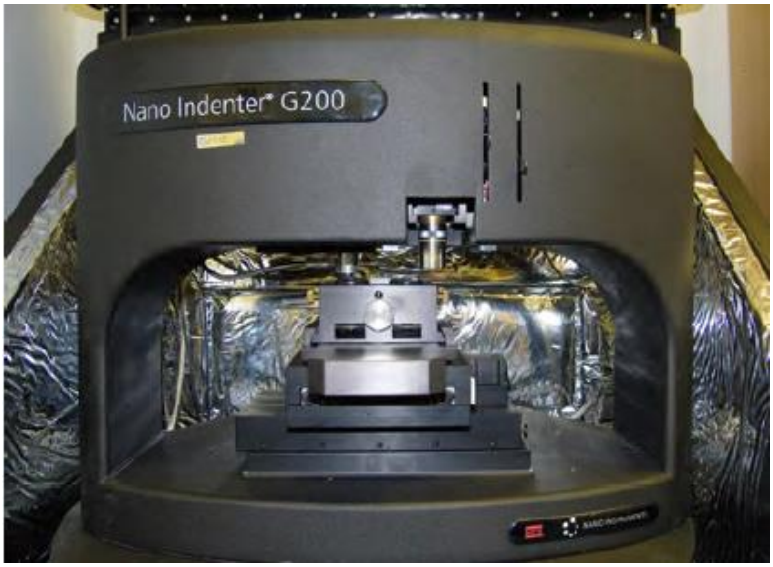

Figure 2.6 Photographs of Nano Indenter G200 (MTS).

Fig. 2.7 below provides a typical load-depth curve recorded by CSM method for NiCo sample with informative parameters indicated.

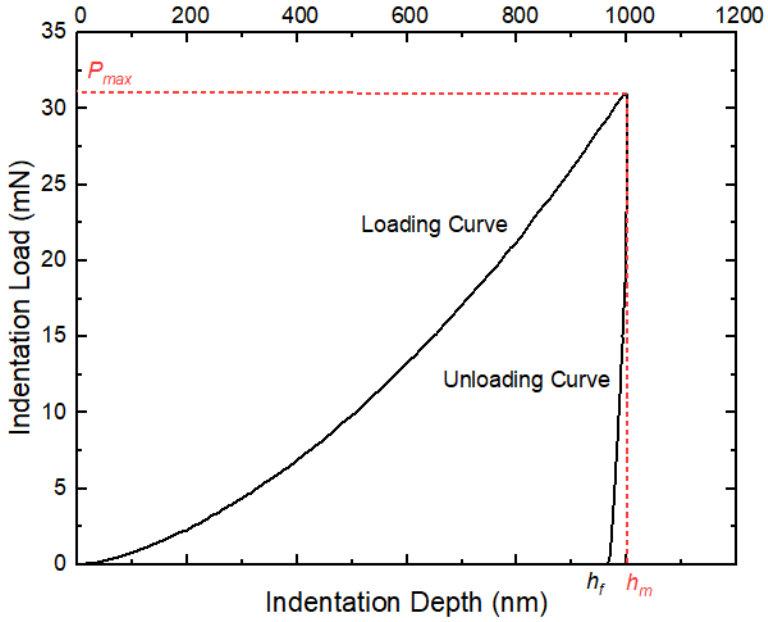

Figure 2.7 A typical load-depth curve for NiCo samples.

Where, h_m corresponds to the displacement observed at the peak load P_{max}. h_f signifies the final displacement that occurs following complete unloading. S denotes the initial contact stiffness during unloading and can be calculated by:

$$S = \left(\frac{dP}{dh}\right)_{unloading} \tag{2.3}$$

where h_c is the contact depth, which refers to the depth at which the indenter is in contact with the sample while under load. The contact depth can be estimated based on Oliver-Pharr method:

$$h_c = h_{max} - \varepsilon \frac{P_{max}}{S} \tag{2.4}$$

In this study, the tip area function was corrected on a fused silica sample and

$$A = 22.3852{h_c}^2 + 493.1381h_c \tag{2.5}$$

Now, the indentation hardness can be obtained from:

$$H = \frac{P_{max}}{A} \tag{2.6}$$

Based on relationships developed by Sneddon, reduced elastic modulus can be expressed as follows:

$$E_r = \frac{\sqrt{\pi}}{2} \cdot \frac{S}{\sqrt{A}} \tag{2.7}$$

where E_r is the reduced modulus, which accounts for elastic deformation for both the indenter and sample. It can be expressed as:

$$E_r = \frac{1 - v^2}{E} - \frac{1 - v_i^2}{E_i} \tag{2.8}$$

After obtaining this reduced modulus, elastic modulus of sample E can be derived:

$$E = (1 - v^2)\left[\frac{1}{E_r} - \frac{(1 - v_i^2)}{E_i}\right]^{-1} \tag{2.9}$$

Different from the conventional method, the CSM method involves applying a harmonic force into the increasing load. During the testing procedure, the depth-dependent displacement response of the indenter is continuously monitored at the excitation frequency (as shown in Fig. 2.8).

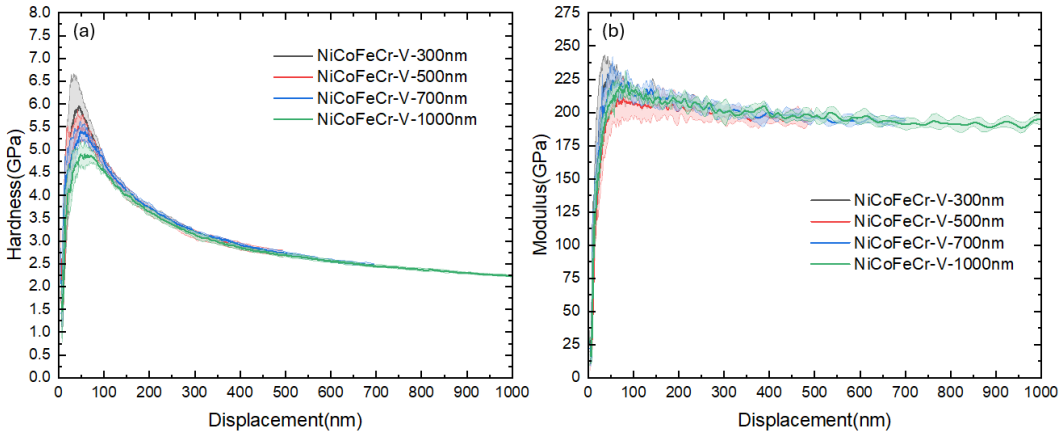

Figure 2.8 Typical hardness-displacement and modulus-displacement recorded by using CSM method.

In addition, the strain rate sensitivity can also be obtained based on the nanoindentation strain jump tests and was defined as:

$$\dot{\varepsilon}_i = \frac{\dot{h}}{h} = \frac{1}{2}\left(\frac{\dot{P}}{P} - \frac{\dot{H}}{H}\right) \tag{2.10}$$

where h and $\dot{h}$ are instantaneous displacement and displacement rate of the indenter, P and $\dot{P}$ are the current load and loading rate during indentation.

2.6 Flat punch indentation

Hysitron PI-88 picoindeter system was utilized and in-situ nanoindentation was performed inside of the SEM chamber as shown in Fig. 2.9. This technique allows for real-time monitoring of indentation-induced deformation and load-depth curves will also be recorded at the same time. This simultaneous capture enables the correlation between mechanical properties and physical behaviors. Fig. 2.10 shows a representative in-situ nanoindentation testing process

performed on Si. Load-depth curves are recorded and along with the instant monitoring of deformation process.

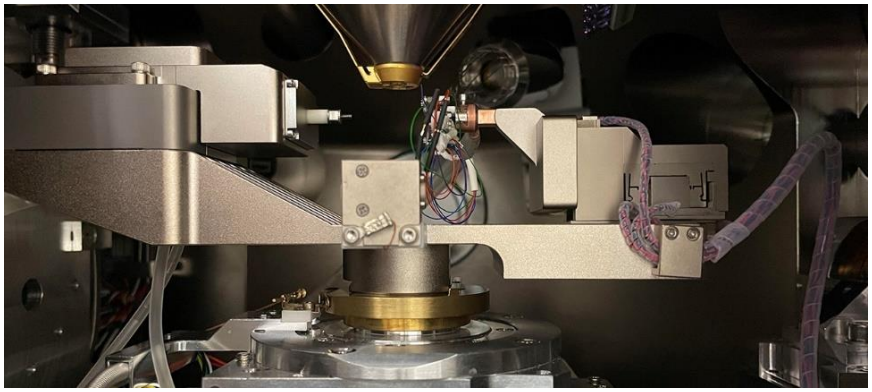

Figure 2.9 Photographs of Hysitron PI-88 picoindenter installed inside of SEM chamber.

Figure 2.10 Screenshots of in-situ nanoindentation testing process performed on Si.

CHAPTER 3 : DEFORMATION MECHANISMS IN SINGLE CRYSTAL NI-BASED CONCENTRATED SOLID SOLUTION ALLOYS BY NANOINDENTATION*

3.1 Overview

Nanoindentation is a critical technique to probe mechanical properties at the micrometer and sub-micrometer scales, accompanied by challenges from indentation size effect, pile-up/sink-in effect, and strain rate sensitivity. In this study, different nanoindentation techniques have been employed to explore Ni-based concentrated solid solution alloys (CSAs) with the addition of 3*d* transition metal elements including Co, Cr, Mn, and Fe, including unique single-crystal Ni, NiCo, NiFe, $Ni_{80}Cr_{20}$, and NiCoFeCr samples with (100) surfaces. A procedure of nanoindentation tests and data analysis/correction have been developed, and a data set of hardness, elastic modulus, strain rate sensitivity, and activation volume for Ni-based CSAs are provided, including the less explored binary alloys such as $Ni_{80}Cr_{20}$ and $Ni_{80}Mn_{20}$. The results show that the type of alloying elements is more critical than the number of elements in strengthening: Co does not provide strengthening in NiCo, while Cr, Mn, and Fe are effective strengthening elements. Cr is the most effective among all the 3*d* transition metal elements. Furthermore, atomic-level lattice distortion is responsible for the strengthening and the role of stacking fault energy is insignificant in Ni-based CSAs at room temperature. In summary, nanoindentation shows increasing promise as a reliable and fast tool to provide comprehensive mechanical information for new alloy design and development.

---

* This chapter is reprinted with permission from “Deformation mechanisms in single crystal Ni-based concentrated solid solution alloys by nanoindentation” by L. Yang, Y. Chen, J. Miller, W.J. Weber, H. Bei, Y. Zhang, Materials Science and Engineering: A 856 (2022) 143685.

3.2 Introduction

A new class of alloys containing multiple elements in near-equiatomic concentrations was reported by two groups [147, 148] independently in 2004. In contrast to conventional alloys with a limited number of possible element combinations because of the tendency to cluster around the corners or edges of phase diagrams, these new alloys near the centers of phase diagrams provide significantly more element combinations, especially in quaternary, quinary and higher-order systems. Yeh and co-workers proposed a new name, high entropy alloys (HEAs), for this new class of alloys containing five or more elements in relatively high concentrations (5–35 at.%). They reasoned that, as the number of elements in an alloy increased, the entropic contribution to the total free energy would overcome the enthalpic contribution and stabilize solid solutions. The concept of HEA has created a wave of research to explore the extended materials design space for mechanical properties [1, 149, 150] and radiation tolerance [85, 88, 151] that were hitherto thought to be unobtainable. Some alternative names with extended concepts were also used in literature, such as multi-principal element alloys (MPEAs), complex, concentrated alloys (CCAs)[152], and concentrated solid solution alloys (CSAs) [88]. As discussed in Ref. [85], the HEA concept has also inspired a re-evaluation of classical thermodynamic concepts as they apply to CSAs [152]. In this study, the name of CSAs is adopted, including binary and quaternary alloys.

The benchmark material, single-phase equiatomic CrMnFeCoNi “Cantor” alloy, demonstrates a break-up of the strength-ductility trade-off. The investigation of this alloy laid the foundation for the fundamental understanding of HEAs [85, 152, 153]. Later, it was discovered that besides configurational entropy (i.e., the number of alloying elements), the nature of the constituent elements also significantly affects mechanical properties [154]. For example, alloys

with the same number of elements may show different mechanical strengths [154]: Quaternary FeNiCoCr is much stronger than FeNiCoMn; Ternary CrCoNi is much stronger than MnFeNi; Binary FeNi is much stronger than NiCo. In addition, the ternary CrCoNi alloy has a higher strength than the quinary CrMnFeCoNi alloy and quaternary FeNiCoCr, NiCoCrMn, and FeNiCoMn alloys [154]. These surprising findings have triggered more generalized studies on CSAs with multiple principal elements.

The unique feature of atomic-level complexity [155, 156] in CSAs results in lowered and varying stacking fault energies (SFEs), atomic volume misfit and short-range order (SRO), which modify dislocation behavior (e.g., friction stress) and twinning activities. The fundamental plasticity mechanisms in CSAs such as dislocation nucleation/ propagation, dislocation-obstacle interaction, phase transformation and twinning are similar to those in conventional alloys [1, 149]. Therefore, many studies are devoted to incorporating the unique features of CSAs, such as lattice distortion, SRO, entropy, and sluggish diffusion, to the classic theories used for conventional alloys with only one principal element [149]. For instance, for high-entropy CrMnFeCoNi, a combination of high strength, great work hardening, and excellent ductility was ascribed to a synergy of multiple deformation mechanisms, including the easy motion of Shockley partial dislocations, dislocation interactions to form stacking-fault parallelepipeds, and dislocation arrest at planar slip bands of undissociated dislocations [157]; For medium-entropy CrCoNi, Laplanche *et al.* ascribed high strength and good ductility to nanoscale twinning [29] and Zhang *et al.* ascribed strength-ductility synergy of CrCoNi to localized face-centered cubic (FCC) – body-centered cubic (BCC) phase transitions due to SRO prior to the ultimate stress [158]; Wu *et al.* compared tensile properties of single-phase binary, ternary and quaternary CSAs at different temperatures and emphasized the critical role of constituent elements [154].

First-principles calculations have been used to study the origin of these unique features of CSAs. The key to bridging local electronic structure features and mechanical behaviors is to understand the behavior of deformation-associated defects in CSAs [159], such as dislocations and twins. For example, Zhao *et al.* discovered that in FCC CSAs, the variation of SFE is related to the electronic properties of the constituent elements, while its temperature dependence is governed by phonon properties [160]. Recently, it was reported that solid solution strengthening in FCC CSAs is ascribed to the configurational fluctuation of the atomic-level pressure originating from the charge transfer between neighboring elements [155]. However, this strengthening model overestimates the strength by a factor of four compared to the experimental results. Therefore, more delicate and robust descriptors are still needed to quantitatively describe the mechanical behaviors of CSAs from the perspective of the local electronic structure features [159, 161].

Hardness is widely used and technically relevant property of materials. As stated by Tabor [123], “hardness implies the resistance to deformation” and “the indentation hardness of metals may in general be expressed in terms of the plastic and, to a lesser extent, the elastic properties of the metals concerned”. Since the Brinell test was invented in the 1900s, various macro-/ micro-indentation tests and corresponding ASTM standards have been developed. For instance, ASTM E10, E18 and E92 have been used for Brinell, Rockwell, and Vickers tests of metallic materials, respectively.

To meet ever-increasing needs and interests in predicting material behaviors in the world of the small, nanoindentation is a critical technique to probe mechanical properties at the micrometer and sub-micrometer scales. It benefited from the development of instruments capable of continuously measuring load and displacement throughout an indentation [162, 163].

Nanoindentation has the advantage of easy sample preparation and statistically rich data sets [163, 164]. This technique is especially important for thin films [102-104] and surface-modified materials (e.g., ion-irradiated materials [97, 105-108]), of which the mechanical property measurement cannot be achieved by traditional mechanical tests (e.g., tensile tests) due to limited volume. The methods and applications have been recently reviewed [109-111].

Hardness and elastic modulus are the two most common properties obtained from nanoindentation., The hardness is usually defined as the ratio of the indentation load and either the surface or projected area of residual indents, in which the indentation load underneath the tip depends on elastic modulus, yield strength, Poisson's ratio, work-hardening exponent, and indenter geometry [165, 166]. Essentially, the hardness represents a flow state of materials underneath the indenter: Tabor [123] pointed out that the hardness is approximately 3 times the yield strength (σ_Y) for materials without work-hardening behavior; For fully hardened materials, the hardness is approximately 3 times the ultimate tensile strength (σ_{UTS}). Most metallic materials have hardness values between $3\sigma_Y$ and $3\sigma_{UTS}$. Tabor [123] also noted that bulk indentation hardness is approximately 3 times the flow stress at a representative strain of 8% - 10%. A detailed discussion of different types of relationships between hardness and strength is reported elsewhere [165]. A recent study showed that single-phase HEAs conform to the 3-times relation between Vickers hardness and σ_{UTS} [167]. However, size and scale effects for smaller sample dimension or volume have been observed in numerous studies and are critical to not only understand the new phenomena at the smaller scale but also quantitatively correlate materials behavior at this scale to that at a larger scale, such as in micro/macro-indentation and uniaxial tension. The influence of factors such as pile-ups/sink-ins and indentation size effects (ISE) needs to be considered [133].

More comprehensive material properties collected by nanoindentation techniques are required to accelerate the screening/investigation of new advanced alloys. In this study, Ni-based CSAs with the addition of 3*d* transition metal elements including Co, Cr, Mn, and Fe are the focus as these elements have shown effective modification of electron band structure and promising property improvement. The study is more comprehensive than previous studies on Ni-based CSAs for several aspects: (a) it includes unique single-crystal Ni, NiCo, NiFe, $Ni_{80}Cr_{20}$, and NiCoFeCr samples with the same crystallographic orientation that exclude microstructural and grain orientation effects; (b) it investigates a broad spectrum of CSAs, including the less explored NiCr and NiMn binary alloys. A direct comparison of Ni, NiCo, NiFe, $Ni_{80}Cr_{20}$, $Ni_{80}Mn_{20}$, and NiCoFeCr is available for insights to future materials design; (c) it provides a thorough procedure of nanoindentation data correction for indentation hardness and strain rate sensitivities of Ni-based CSAs, which is important but not previously available in the literature [154].

The structure of this paper is as follows: Hardness correction, including ISE and pile-ups in various CSAs (3.1), is performed and discussed; Two types of deformation related dislocations that can assist in the understanding of deformation mechanisms under nanoindentation are calculated and compared, i.e., geometrically necessary dislocations and statistically stored dislocations (3.2); The dislocation migration is discussed through the activation volume of dislocations in CSAs, which is calculated through strain rate sensitivity from nanoindentation strain rate jump tests with consideration of ISE (3.3); Finally, deformation mechanisms of CSAs including solid solution strengthening and forest hardening were discussed (3.4).

3.3 Materials & methods

Ni-based single-phase CSAs, including pure Ni, binary Ni-based alloys [96, 145] ($Ni_{80}Cr_{20}$, $Ni_{80}Mn_{20}$ NiCo, NiFe with 20 at.% Cr, 20 at.% Mn, 50 at.% Co and 50 at.% Fe, respectively), and quaternary Ni-based alloy (NiCoFeCr) [168], were prepared by arc-melting. The atomic percentages were chosen based on phase stability to maintain an FCC crystal structure. For instance, 20 at.% Cr was selected in $Ni_{80}Cr_{20}$ due to the fact that FCC phase is not stable at 500^{o}C once the Cr concentration exceeds 22 at.% [145, 169] according to the phase diagram. Similarly, 22% is the maximum Mn concentration for alloying Ni and Mn to form a stable FCC phase [145]. The purity of Ni, Fe, Cr, and Mn for arc melting is higher than 99.9%. The arc-melted buttons were flipped and re-melted at least five times before drop casting to ensure homogeneous mixing. A floating-zone directional solidification method was used for single-crystal growth.

The nanoindentation was performed on Agilent NanoIndenter G200 (MTS) with a Berkovich diamond tip. The continuous stiffness measurement (CSM) based on the Oliver-Pharr method [163] was chosen to record hardness and elastic modulus values as a function of penetration depth continuously. The tip area function was corrected on a fused silica sample. Eight indents were performed on each sample with a maximum penetration depth of 2 μm. In addition to standard hardness and elastic modulus measurement, strain rate sensitivity of samples was also obtained using nanoindentation strain rate jump testing technique. Three strain rates were selected: 0.05/s, 0.007/s and 0.001/s. As hardness decreases along with the depth, strain rate sensitivity was corrected to account for the hardness change rate (unit: Pa/s), which will be discussed later. To evaluate the amount of pile-ups around indents, an Atomic Force Microscope (AFM, Veeco Dimension 3100 Metrology AFM) was utilized to image indent topographies.

AFM micrographs were analyzed using Gwyddion software [170] and the correction method will be discussed later. The region underneath the indenter was lifted out by Focus Ion beam (FIB, model: FEI Quanta 3D workstation) and examined by Transmission Electron Microscopy (TEM, model: JEOL 2100).

3.4 Results and discussion

Ni, NiCo, NiFe, $Ni_{80}Cr_{20}$, and NiCoFeCr were confirmed as single-crystal FCC structure with (100) surfaces in our previous studies [96, 145, 168], and $Ni_{80}Mn_{20}$ has a polycrystalline FCC structure with an average grain size of 100 – 200 μm [145], in which the grain boundary effects are negligible. The bright-field TEM micrographs of these materials are summarized in Fig. S1. After indentation, one indented region in the NiCo sample was lifted out by FIB and subsequently examined by TEM. The bright-field TEM micrograph (Fig. 3.1) of the indented region in NiCo shows the single-crystal feature. Bend contours and dislocation loops from indentation and FIB damage can be observed. The inset of the selected-area diffraction (SAD) pattern confirmed that the NiCo sample has a single crystal FCC structure with (100) surface. No obvious subgrains were discovered in this indented region. Recently, electron backscatter diffraction and precession electron diffraction capable of mapping high-resolution crystallographic orientation revealed local crystal rotation near the indenter tip due to plasticity during nanoindentation [171, 172]. The orientation maps near the indenter for different Ni-based CSAs will be interesting to explore in the future, as they might suggest the difference in local plasticity in different Ni-based CSAs.

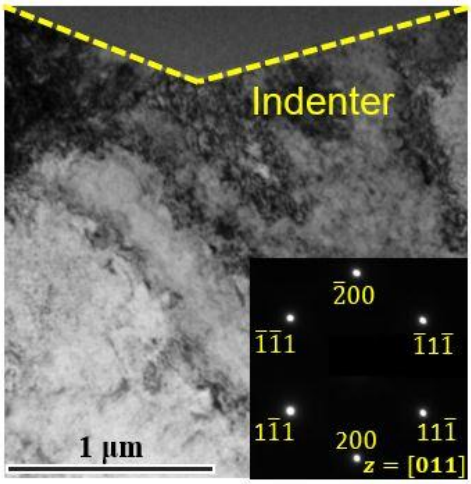

Figure 3.1 Bright-field TEM image of the region underneath the indenter for NiCo. The inset of the selected-area diffraction pattern confirms the single-crystal structure after indentation and the surface normal of <100> crystallographic direction.

3.4.1 Nanoindentation hardness correction

Figure 3.2a compares hardness variation as a function of depth up to 2 μm. At a depth of 2 μm, Ni and NiCo have close hardness values of about 1.2 GPa; $Ni_{80}Cr_{20}$ shows the highest hardness of 2.2 GPa; $Ni_{80}Mn_{20}$, NiFe, NiCoFeCr show close hardness values of 1.8 GPa, 1.7 GPa, 1.9 GPa, respectively. The elastic moduli of Ni, NiCo, $Ni_{80}Mn_{20}$, $Ni_{80}Cr_{20}$, NiFe, and NiCoFeCr are 184±4, 174±6, 191±5, 205±3, 153±5, and 186±2 GPa, respectively. ISE is obvious for all samples in Fig. 3.2a, i.e., an increase in hardness with decreasing penetration depth [173]. To understand the ISE, the classic Nix-Gao model using the concept of geometrically necessary dislocations (GND) was followed [136], which describes the relationship between nanoindentation hardness (H) and macro-hardness (H_0) as

$$H = H_0\sqrt{1 + \frac{h^*}{h}} \tag{3.1}$$

where h represents penetration depth and $h^*$is defined as characteristic depth. Following Eqn. 3.1, H versus h curves in Fig. 3.2a were replotted as H^2 versus $1/h$ in Fig. 3.2 b, in which H_0 and h^* can be obtained from the linear fitting: the intercept is H_0^2 and the slope is associated with the characteristic depth, h^*. The fitting range of 0.5 μm to 2 μm was selected to avoid the error from the blunt tip area. The intercepts and slopes for CSAs are summarized in Fig. 3.2 c. For H_0, $Ni_{80}Cr_{20}$ is the hardest sample with a hardness value of 1.9 GPa, followed by $Ni_{80}Mn_{20}$, NiFe and NiCoFeCr with H_0 of 1.5-1.6 GPa. H_0 is lower for Ni (1.1 GPa) and NiCo (0.9 GPa) (Fig. 3.2 a). NiCo has a stronger ISE than Ni. For comparison, the hardness at 2 μm without any correction is labeled as H_{IT} hereafter.

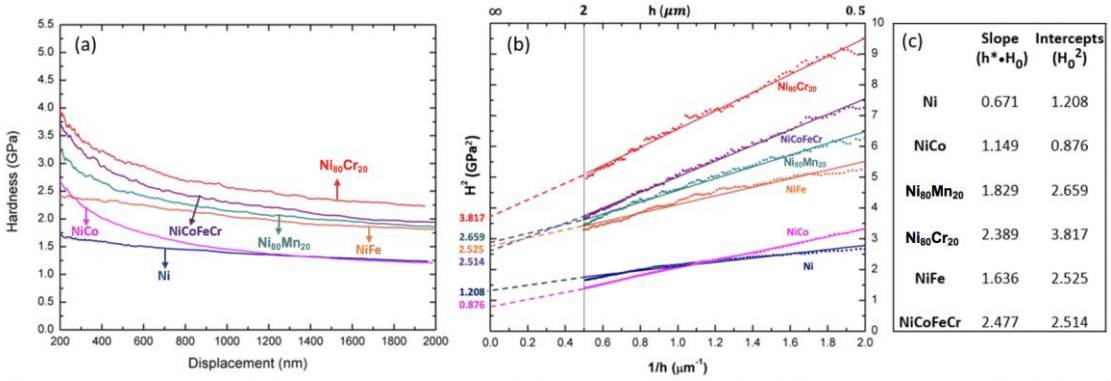

Figure 3.2 (a) a comparison of nanoindentation hardness (H) evolution of Ni, NiCo, $Ni_{80}Mn_{20}$, $Ni_{80}Cr_{20}$, NiFe and NiCoFeCr as a function of displacement (h, penetration depth); (b) a plot of H^2 vs. 1/ h with linear fitting on Ni and CSAs; (c) a summary of slopes and intercepts of fitting lines in (b).

In addition to ISE, pile-up/sink-in is another issue that underestimates/overestimates the contact area and therefore overestimates/underestimates the hardness. AFM micrographs (Fig. 3.3) of indentation imprints for Ni and CSAs demonstrate that pile-ups are obvious: qualitatively, pile-ups in Ni, $Ni_{80}Cr_{20}$ and NiFe are more obvious than those in $Ni_{80}Mn_{20}$, NiCo and NiCoFeCr. Quantitative pile-up corrections are discussed as follows.

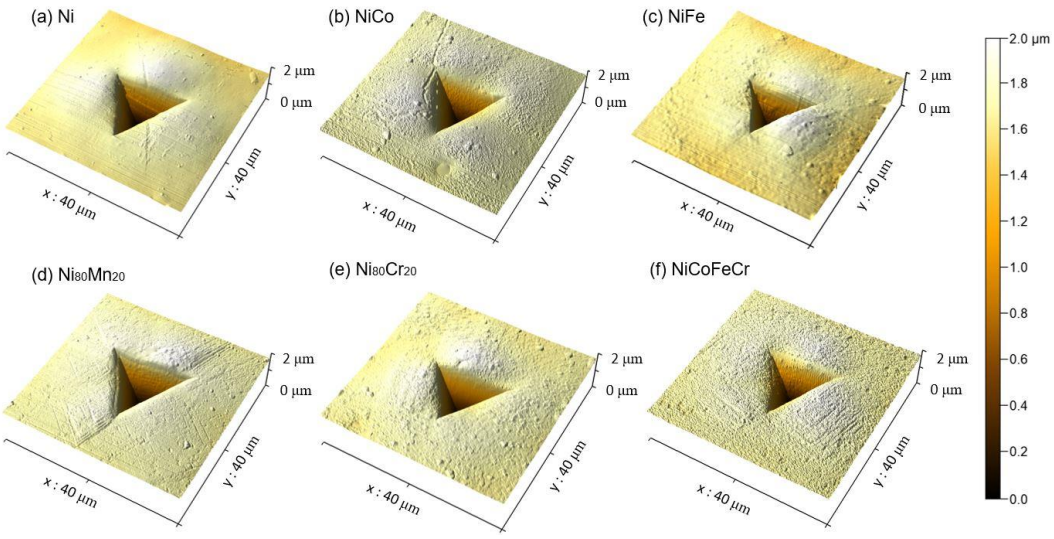

Figure 3.3 AFM micrographs of indentation imprints for Ni, NiCo, NiFe, $Ni_{80}Mn_{20}$, $Ni_{80}Cr_{20}$, and NiCoFeCr. Pile-ups exist in all samples.

There are several pile-up correction methods in the literature [174-176]. Kese's semi-ellipse method [177, 178] is employed in this study, as it is based on real surface morphology analysis near the imprints. Fig. 3.4a demonstrates an AFM micrograph of one representative pile-up in $Ni_{80}Cr_{20}$. Following Kese *et al*. [177], the corrected contact area (A_C) is composed of geometrical contact area (A) obtained from the Oliver and Pharr analysis of nanoindentation data and extra pile-up area (A_{pu}) as written as below,

$$A_C = A + A_{pu} \tag{3.2}$$

In this study, $A = 22.3852h^2 + 493.1381h$. A_{pu} is calculated as the sum of projection area along three edges following the work from Kese *et al*.[177]:

$$A_{pu} = \frac{\pi l}{4} \sum a_i \tag{3.3}$$

where l was the edge length of the residual imprint of the Berkovich indenter characterized by

AFM, a_i is the horizontal distance from the edge of the indent to the actual contact periphery (Fig. 3.4b).

Although this method of measuring a_i works well for high-strength and brittle materials, it introduces uncertainty when the pile-up peak is extended and broadened. As schematically shown in Fig. 3.4b, the usage of measured a_i is ideal (labeled as ideal) for calculating A_{pu} when the indenter tip is in contact with the peak of the profile. In such a case, a_i and h_i are correlated by $a_i = h_i \cdot tan65.3^{\circ}$ and the selection of either measured a_i or measured h_i for A_{pu} calculation is equivalent. However, if the pile-up extends further away, as schematically shown in Fig. 3.4b (labeled as real), A_{pu} is overestimated using the measured a_i for Eqn. 3.3. Surface profiles along three lobes in $Ni_{80}Cr_{20}$ (Fig. 3.4a) are shown in Fig. 3.4c and the pile-up region is magnified in Fig. 3.4d. When the Berkovich tip with three-fold rotational symmetry is in contact with (100) surface with four-fold rotational symmetry, the deformation near three sides is not equivalent and the pile-ups at three lobes are different: #1 (a_1=2.42 μm, h_1 = 0.26 μm); #2 (a_2=2.42 μm, h_2 = 0.20 μm) and #3 (a_2=4.68 μm; h_3 = 0.08 μm). It is noted that the selection of measured h_i for calculating A_{pu} is more reasonable than the selection of a_i based on three observations: (a) a_1 and a_2 are both equal to 2.42 μm, but their pile-up profiles are different; (b) #2 has a plateau, instead of a peak, and a_2 could vary from 2.42 μm to 3.93 μm (labeled as a_2' in Fig. 3.4d), which introduces a large uncertainty of A_{pu} calculation; (c) #3 has the largest a (a_3 = 4.68 μm), but the pile-up height (h_3=0.08 μm) is small and the profile shows a minimum pile-up. Therefore, A_{pu} for all indents is calculated using the measured h_i, and a_i is calculated by $h_i \cdot tan65.3^{\circ}$ for Eqn. 3.3. With the calculated A_c/A (Ni: 1.17$\pm$0.02; NiCo: 1.13 $\pm$0.02; $Ni_{80}Mn_{20}$: 1.12 $\pm$0.02; $Ni_{80}Cr_{20}$: 1.16 $\pm$0.02; NiFe: 1.17 $\pm$0.01; NiCoFeCr: 1.13 $\pm$0.02), the hardness is corrected by:

$$\frac{A_c}{A} = \frac{H}{H_c} \tag{3.4}$$

The corrected hardness H_{IT} and macro-hardness H_0 (calculated from Nix-Gao model) are labeled as H_{IT_C} and H_{0_C}, and summarized in Fig. 3.5. The comparison of H_{IT}, H_{IT_C} and H_0 indicate that ISE and pile-up effect are the two major factors that cause the overestimation of hardness. It is interesting to note that whether ISE or pile-up effect is more dominant depends on the alloy compositions: pile-up effect plays a more dominant role in NiCo and NiCoFeCr. This indicates that NiCo and NiCoFeCr might have a lower work-hardening capability than the rest of the CSAs, which will be discussed in section 3.4.

Before the correction, the hardness values (H_{IT}) of Ni, NiCo, and NiFe are close to those reported in the literature [179]. After correction of the ISE and pile-up effects, H_{0_C} is the true macro-hardness values (Ni: 0.94 ± 0.08 GPa; NiCo: 0.83 ± 0.05 GPa; $Ni_{80}Mn_{20}$: 1.45 ± 0.01 GPa; $Ni_{80}Cr_{20}$: 1.65 ± 0.04 GPa; NiFe: 1.36 ± 0.02 GPa; NiCoFeCr: 1.40 ± 0.04 GPa). These alloys can be divided into two groups: Ni and NiCo have lower hardness of less than 1 GPa, while $Ni_{80}Cr_{20}$, $Ni_{80}Mn_{20}$, NiFe, NiCoFeCr have higher hardness of more than 1.35 GPa. $Ni_{80}Cr_{20}$ has the highest hardness. This suggests that Co does not have a strengthening effect. Mn, Cr, and Fe are effective elements in strengthening and Cr is the most effective, which will be discussed later.

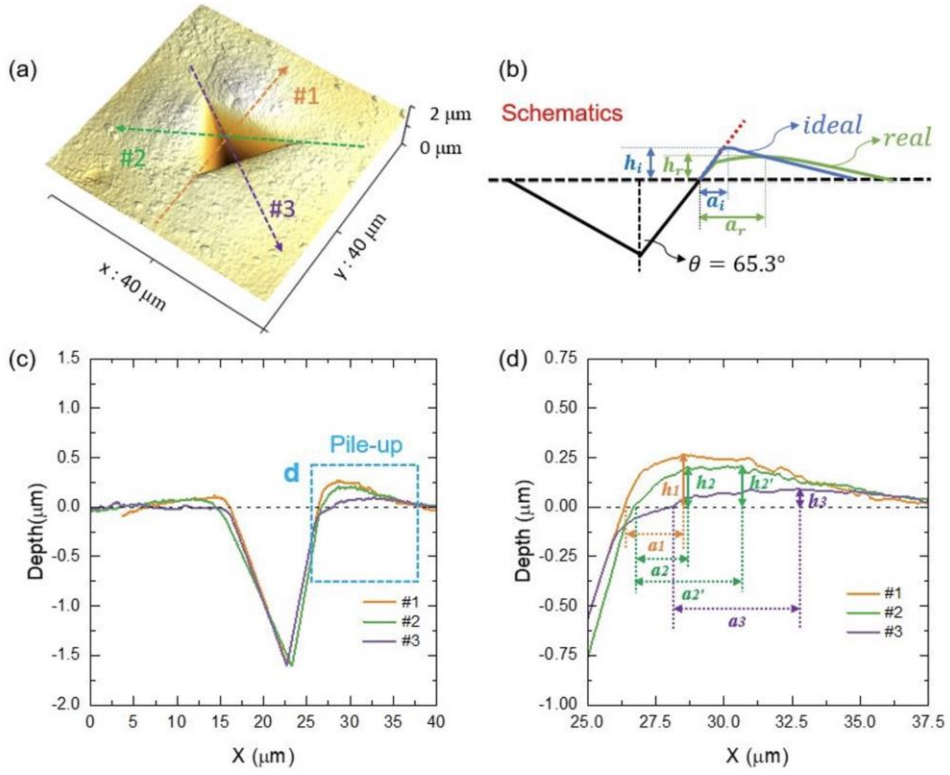

Figure 3.4 (a) AFM image of an indentation imprint on $Ni_{80}Cr_{20}$ displays apparent pile-ups; (b) the surface profiles of ideal and real pile-up profiles are schematically shown to determine the contact periphery of the indenter (a_i) and height of pile-up (hi); (c-d) the three surface profiles in (a) show a_i and h_i (i=1-3).

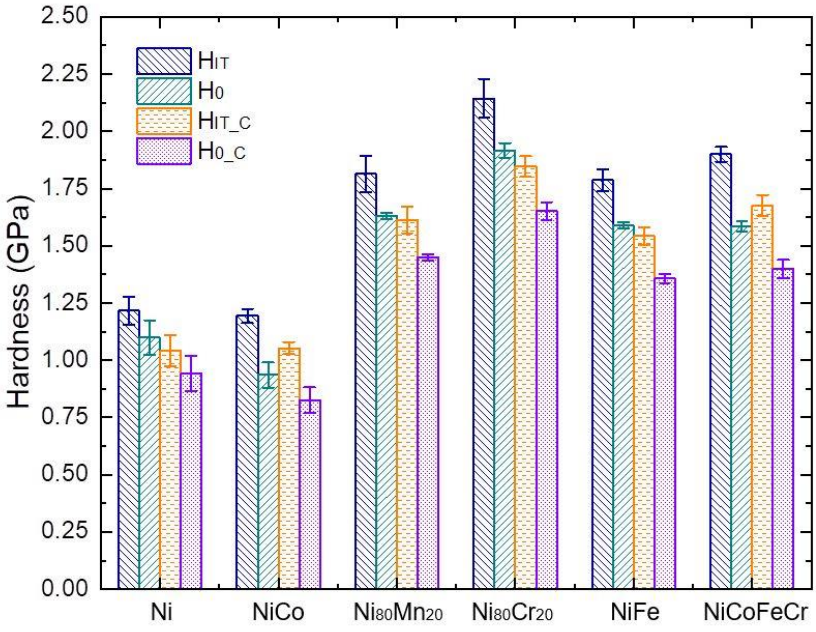

Figure 3.5 A summary of nanoindentation hardness at 2 μm (H_{IT}), macro-hardness (H_0) from Nix-Gao model, pile-up corrected H_{IT} (H_{IT_C}), pile-up corrected H_0 (H_{0_C}) hardness.

3.4.2 GNDs and SSDs in CSAs

For ductile materials such as Ni and CSAs in this study, the plastic deformation during indentation is carried by dislocations. The increase in dislocation density leads to higher flow stress of the materials. During nanoindentation, two types of dislocations are considered: geometrically necessary dislocations (GNDs) and statistically stored dislocations (SSDs) [180, 181]. The densities of GNDs (ρ_G) and SSDs (ρ_s) in Ni and CSAs are estimated to understand the different deformation behaviors of CSAs. The GND density is related to the strain gradient by compatibility requirements. The strain gradient has to be accommodated by a certain number of GNDs and Ma-Clarke model estimates the GND density as [70, 137]:

$$\rho_G = \frac{4\gamma}{bh} \tag{3.5}$$

where γ refers to average shear strain, b represents Burgers vector, and h is indentation penetration depth. Accordingly, combined with Taylor relation, hardness is approximated by ρ_s and ρ_G,

$$H \approx \mu b[\rho_s + \rho_G]^{\frac{1}{2}} \tag{3.6}$$

where μ is shear modulus from nanoindentation; ρ_s is estimated from corrected hardness by $(H_{0\_C}/\mu b)^2$, which is constant and depth independent. On the other hand, ρ_G is depth dependent: At the depth of 2 μm, the corrected hardness, H_{IT_C} was used as H in Eqn. 3.6 and therefore ρ_G can be obtained at h = 2 μm. ρ_s and ρ_G are summarized in Fig. 3.6. ρ_s is the largest in NiFe ($8.5 \times 10^{15}/m^2$), lower in $Ni_{80}Cr_{20}$ ($7.1 \times 10^{15}/m^2$), $Ni_{80}Mn_{20}$ ($6.2 \times 10^{15}/m^2$), and NiCoFeCr ($6.1 \times 10^{15}/m^2$), and lowest in Ni ($2.9 \times 10^{15}/m^2$) and NiCo ($2.4 \times 10^{15}/m^2$).

The comparison of ρ_S and ρ_G shows that at the depth of 2 μm, ρ_S plays a more dominant contribution to hardness.

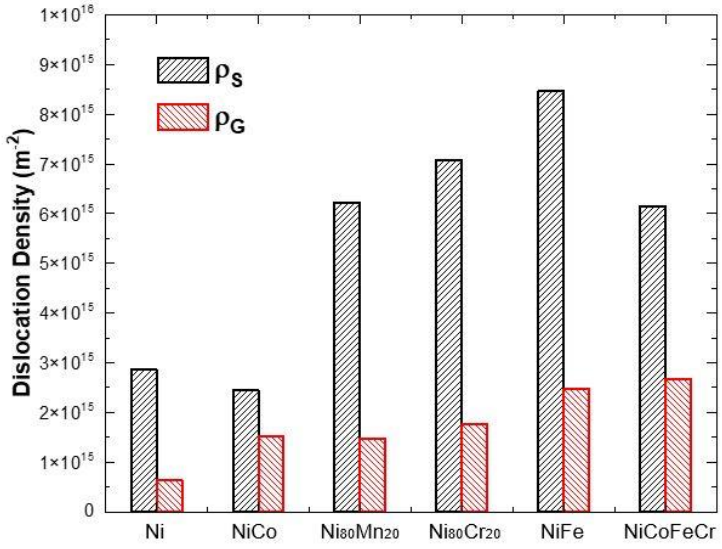

Figure 3.6 Densities of Statistically Stored Dislocations (SSD, ρ_S) and Geometrically Necessary Dislocations (GND, ρ_G) for Ni and CSAs calculated from the Ma-Clarke model.

As shown in Eqn. 3.5, ρ_G is depth dependent. With the known ρ_G at h = 2 μm, the only unknown parameter, the average shear strain, γ in Eqn. 3.5 can be obtained for all CSAs. ρ_G for all CSAs as a function of indentation depth is compared in Fig. 3.7. ρ_G decreases at a deeper penetration depth. ρ_G is the highest in NiCoFeCr, lower in NiFe and $Ni_{80}Cr_{20}$, and the lowest in Ni. NiCo and $Ni_{80}Mn_{20}$ have close ρ_G. This interesting observation can be reasoned as follows. It is assumed in the Nix-Gao model that the distribution of GNDs is constrained within the hemispherical shape underneath the indenter, as schematically shown in the inset of Fig. 3.7. If it is assumed that the total number of GNDs required to accommodate the compatibility requirements from indentation is the same for all samples, a higher ρ_G means a smaller volume accommodating GNDs. This implies that the migration of GNDs is easier in Ni, which allows a longer migration distance, but it is more difficult in CSAs. This is related to dislocation

migration kinetics and SSD density. This assumption is consistent with the discovery by molecular dynamics simulation that dislocations underneath the indenter migrate slower in NiFe than in pure Ni [182]. More information on dislocation migration can be reflected by the activation volume of dislocations, which will be studied by nanoindentation strain rate jump tests in the following section.

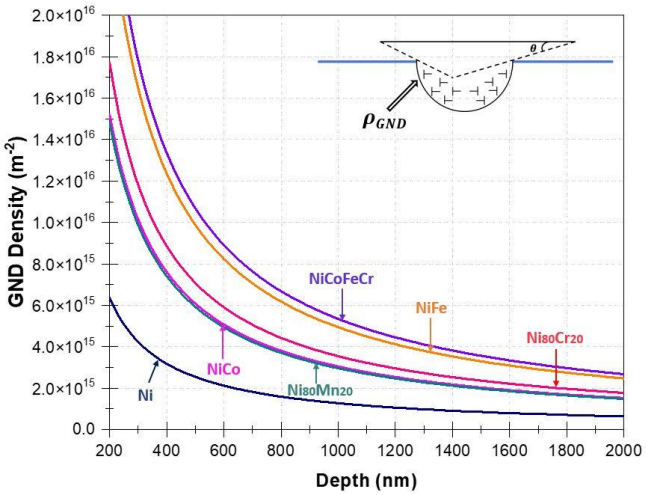

Figure 3.7 Depth dependence of GND density in Ni and CSAs. The inset schematically shows GNDs distributed within a hemispherical volume underneath an indenter.

3.4.3 Strain rate sensitivity and activation volume in CSAs

Strain rate sensitivity (m) and activation volume (V) are two key parameters that are useful for understanding the deformation kinetics [183, 184]. The activation volume is defined as the volume of a material involved in the process of overcoming the energy barrier. Here, the activation volume expresses the volume that is physically swept by a dislocation from a ground equilibrium state to an activated state after the deformation [185].

Nanoindentation strain rate jump tests, which abruptly vary the strain rate during indentation, have been demonstrated to be a reliable method for strain rate sensitivity by Maier *et al*. [69] . The strain rate for indentation ($\dot{\varepsilon}_i$) was defined by Lucas and Oliver [186]as:

$$\dot{\varepsilon}_i = \frac{\dot{h}}{h} = \frac{1}{2}\left(\frac{\dot{P}}{P} - \frac{\dot{H}}{H}\right) \tag{3.7}$$

where h and $\dot{h}$ are instantaneous displacement and displacement rate of the indenter, P and $\dot{P}$ are the current load and loading rate. This method has been successfully used for ultrafine-grained and nano-grained metals where H is constant with indentations depths larger than tens or hundreds of nanometers (i.e., $\dot{H}/H = 0$) [69]. In our Ni and CSAs, H keeps decreasing due to ISE *and* $\dot{H}/H$ is not negligible. Therefore, instead of using the conventional assumption of $\dot{H}/H = 0$ in literature, $\dot{H}/H$ is included in our calculation for indentation strain rate (Eqn. 3.7). Subsequently, the strain rate sensitivity of materials can be obtained with modified $\dot{\varepsilon}_i$. This technique was modified from CSM standard method, and several sudden changes in applied strain rates were conducted at several fixed indentation depths within one single test. Fig. 3.8a shows one example in our tests, in which the method to identify the hardness before and after strain rate jumps is labeled. Three strain rates ($\dot{\varepsilon}$ = 0.05/s, 0.007/s, 0.001/s) are selected for jump tests and the base strain rate is 0.05/s. The strain rate sensitivity, m can be calculated by [69]:

$$m = \frac{d(lnH)}{d(ln\dot{\varepsilon})} \tag{3.8}$$

Also, the activation volume, V can be calculated from m and H [69]:

$$V = \frac{3\sqrt{3}\kappa T}{m \cdot H} \tag{3.9}$$

where κ is the Boltzmann constant and T is the absolute temperature. Six indents were performed on each sample for repeatability and the average was taken. The calculated m and

corresponding V are summarized in Fig. 3.8. m is highest in NiCoFeCr (0.0088) and lowest in NiCo (0.0065). Overall, m increases with the increase in elements. V shows an opposite trend with m. The pure Ni and NiCo show larger V of respective 162.5 and 173.1b^3 (b is Burgers vector). V in $Ni_{80}Mn_{20}$, $Ni_{80}Cr_{20}$, NiFe and NiCoFeCr are 96.7, 91.7, 91.3 and 82.4 b^3, respectively. The close value of V in Ni and NiCo suggests that the addition of Co into Ni doesn't change the dislocation kinetics significantly. In contrast, the addition of Fe, Cr and Mn affects dislocation migration significantly. The activation volumes in the range of 82.4 -173 b^3 indicate that the mechanisms with a small V of ~ 1 b^3, such as the kink-pair mechanism, are not dominant in our study. As a reference, in conventional FCC metals with large grain sizes, the forest dislocation interaction dominates the plastic deformation and the activation volume is ~100 -1000 b^3 [187, 188].

In CSAs, both multiple principal elements and forest dislocations contribute to activation volumes of dislocations. Laplanche *et al*. [189] have demonstrated that the inverse activation volumes of solid solution strengthening and forest hardening are additive, i.e., $1/V=1/V_{SS}+1/V_f$. For activation volume for solid solution strengthening, a dislocation in the random alloy responds to the presence of spatially varying concentrations by adopting a wavy shape characterized by wavelength and amplitude. The selection of characteristic waviness is one that minimizes the total dislocation energy by enabling the dislocation to reside in regions of favorable (energy-lowering) regions of concentration fluctuations at the expense of the line tension cost of the wavy shape. The solid solution strengthening effects will be discussed in the next section and here forest dislocations are our focus. The activation volume for forest hardening is associated with the activation area, which is defined by the area swept out by a dislocation segment with a length (*l)* over a distance (*w*) by overcoming energy barriers. The

activation area and activation volume can be related by $V = bwl$ [190, 191]. It is assumed that the dislocation segment is pinned by two dislocation junctions and therefore the distance between two junctions (segment length l) is estimated by $\rho^{-1/2}$ for all CSAs as follows: Ni: 17 nm; NiCo: 16 nm; $Ni_{80}Cr_{20}$: 11 nm; $Ni_{80}Mn_{20}$: 11 nm; NiFe: 10 nm; NiCoFeCr, 11 nm. As a result, w is calculated as 7.5-11 nm, which is lower than l (10-17 nm). The lower w might be related to the local varying concentrations, which is beyond our focus here but deserve further investigations by atomistic simulations.

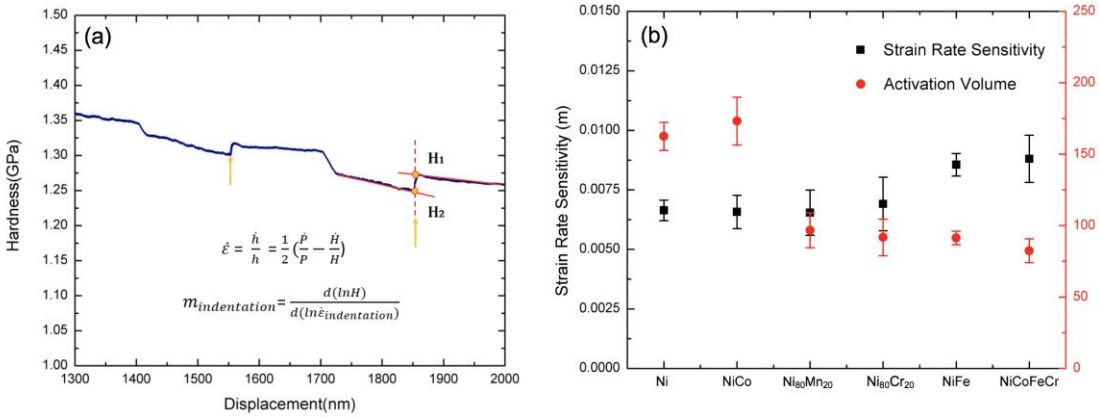

Figure 3.8 (a) determination of strain rate sensitivity by considering the hardness change rate (unit: Pa/s) during nanoindentation strain rate jump tests. Nominal nanoindentation strain rates are 0.05/s, 0.007/s and 0.001/s. (b) the values of strain rate sensitivity and corresponding activation volume for Ni and CSAs.

3.4.4 Deformation mechanisms of CSAs under indentation

As discussed in Section 3.1, the deformation in CSAs can be described under the framework of conventional strengthening mechanisms. In our study on Ni-based CSAs, twinning isn't significant at room temperature, and grain boundary strengthening doesn't exist. Therefore, our discussion focuses on solid solution strengthening and forest hardening.

First, SFEs of Ni and CSAs are compared as SFE often determines the dislocation core structure and corresponding migration kinetics. As summarized in Table 3.1, the addition of

alloying elements into Ni generally lowers SFE. The SFE decreases from 127 mJ/m^2 for pure Ni, to near or below 100 mJ/m^2 for CSAs. As chemical composition varies in CSAs beyond the dilute limit, SFE has a large variation depending on the local atomic environment: The local SFE can be very small and even negative at several sites even though the average SFE remains positive [192]. The negative SFE in FCC CSAs is caused by the energetic preference of hexagonal closed-packed stacking. Furthermore, SRO may also change SFE. For CrCoNi, first-principles calculation shows that intrinsic SFE can be tuned from -42.9 to 30 mJ/m^2 by adjusting SRO [193], which has also been confirmed by experiments [194]. In our study, SFE does not play a significant role in hardness. As shown in Table 1, a significant reduction in SFE from 127 mJ/m^2 in Ni to -10 mJ/m^2 in NiCo does not lead to a significant change in hardness; Also, NiFe and NiCoFeCr with distinct SFEs have a close hardness. Therefore, there is no obvious correlation between SFE and hardness in Ni-based CSAs at room temperature in this study. This observation is consistent with the finding that SFE is less important in CSAs when it is below 100 mJ/m^2 because the separation of two partial dislocations is larger than 10 b [68].

The hardness from nanoindentation reflects the flow stress, which includes solid solution strengthening and work hardening in our study. It is worth noting that hardness alone cannot be distinguished whether the strength is contributed by solid solution strengthening or work hardening. CSAs containing multiple principal elements have serious lattice distortion caused by a large atomic radius difference between different components, which is distinctive from that in pure metal and conventional alloys. The lattice distortion would affect both work hardening and solid solution strengthening.

(a) Work hardening: To understand the work hardening of CSAs during nanoindentation, hardness is compared to tensile properties (i.e., yield strength, σ_Y, and ultimate tensile strength,

σ_{UTS}) of Ni, NiCo, NiFe, and NiCoFeCr, available in literature [154], as summarized in Table 3.1. The strength of CSAs, estimated by *H*/3 [167] lies in between σ_Y and σ_{UTS}. Furthermore, strain during nanoindentation is estimated based on the reported tensile stress-strain curves in literature [11] and the strains to reach *H*/3 for Ni, NiCo, NiFe, and NiCoFeCr are estimated as 15%, 7%, 16%, and 7% (Table 3.1). The representative strains for Ni, and NiCoFeCr are close to the representative strain range between 8% and 10% suggested by Tabor [123] for ductile and work-hardenable metals. Ni and NiFe show higher representative strain of ~15%, indicating they are more work hardenable during indentation. Note that tensile properties in Ref. [154] were obtained from polycrystalline CSAs with a grain size of 24-85 μm and the grain boundary strengthening is not considered here.

Table 3.1 A summary of stacking fault energies (SFEs) yield and ultimate tensile strengths (σ_Y and σ_{UTS}) and estimated strain during nanoindentation for Ni and CSAs

Sample	**SFE (mJ/m^2)**	**σ_Y (MPa)**	**σ_{UTS} (MPa)**	**σ (=H/3) (MPa)**	**Estimated strain during indentation (using tensile data in[154])**
Ni	127 [160]	94 [154]	348 [154]	314	15%
NiCo	-10 [160]	110 [154]	542 [154]	275	7%
$Ni_{80}Mn_{20}$	--	--	--	483	--
$Ni_{80}Cr_{20}$	101 [195]	--	--	550	--
NiFe	105 [160]	188 [154]	512 [154]	452	16%
NiCoFeCr	22[160];20[196]; 34.3[197]	271 [154]	711 [154]	467	7%

(b) Solid solution strengthening: Compared to work hardening, solid solution strengthening is the main cause of the exceptional mechanical properties of HEAs [61] and many strengthening models have been developed, considering dislocation interactions with the random local concentration fluctuations. Starting from the solid solution strengthening models for binary

systems by Fleischer [62] and Labush [198], the theory has been extended to alloys with multiple principal elements [199, 200]. For FCC CSAs, Varvenne *et al*. [68] recently proposed a predictive model in which each element in CSAs is considered as a solute embedded in an effective matrix of surrounding atoms. One advantage of this model is that it does not include any adjustable parameters and allows all model parameters to be computed by experiments or simulations. In addition, the predictive model includes the temperature- and strain-rate dependence of the strength of FCC CSAs, which anticipates future studies on thermal and strain rate effects. The details of model implementations are as follows.

In this model, lattice distortion plays a central role in strengthening in CSAs [201]. The average misfit volume of n^{th} element ($\Delta\bar{V}_n$) is calculated from $\Delta\bar{V}_n = V_n - \bar{V}$, with $\bar{V} = \sum C_n V_n$ and V_n is atomic volume, measured from atomistic simulation or experiments. Since each element has its specific atomic size, severe lattice distortion can occur in CSAs. The lattice distortion (δ) (atomic-size difference) can be estimated by [202]:

$$\delta = \sqrt{\sum_{i=i}^{N} c_i \left(1 - \frac{r_i}{\sum_{j=1}^{N} c_j r_j)}\right)^2} \tag{3.10}$$

where *N* is the number of the components in an alloy system, c_i is the atomic percentage of the ith component, $\sum_{j=1}^{N} c_j r_j$ is the average atomic radius, and r_i is the atomic radius. To explicitly show the influence of lattice distortion (δ) in the solid solution strengthening, the key solute quantity ($\sum C_n \Delta\bar{V}_n^2$) in the model from Varvenne *et al.* was replaced by $9\bar{V}^2\delta^2$. Therefore, the solid solution strengthening can be calculated as [68]:

$$\sigma_{SS}(T,\dot{\varepsilon}) = M\tau_{y0}\exp\left(-\frac{1}{0.51}\frac{kT}{\Delta E_b}\ln\frac{\dot{\varepsilon_0}}{\dot{\varepsilon}}\right) \quad (3.11)$$

Where:

$$\Delta E_b = 0.274\alpha^{\frac{1}{3}}\mu b^3\left(\frac{1+v}{1-v}\right)^{\frac{2}{3}} f_2(w_c)\times\left(\frac{9\bar{V}^2\delta^2}{b^6}\right)^{\frac{1}{3}} \quad (3.12)$$

$$\tau_{y0} = 0.051\alpha^{-\frac{1}{3}}\mu\left(\frac{1+v}{1-v}\right)^{\frac{4}{3}} f_1(w_c)\times\left(\frac{9\bar{V}^2\delta^2}{b^6}\right)^{\frac{2}{3}} \quad (3.13)$$

where M is Taylor factor, 3.06; $\dot{\varepsilon}$ is strain rate, 0.05/s for nanoindentation; μ is shear modulus, estimated from nanoindentation by $\mu = E/2(1+v)$. The rest parameters are the same as [68] : α is dislocation line tension parameter, 0.123; $f_1(w_c) = 0.35$; $f_2(w_c) = 5.70$; $\dot{\varepsilon_0}$ is the reference strain rate, 10000/s; T = 293 K. Two different sets of atomic radii are selected for δ: one is by using Goldschmidt radius (δ_G); The other is by using atomic radius in the relaxed structure from atomistic simulation and experiments (δ_{rlx}), which are summarized in Table 3.2.

As shown in Table 3.2, The assumption that the atomic size is intrinsic to the element (e.g., Goldschmidt radius) is not applicable for CSAs in this study: δ_G and corresponding σ_{SS} for $Ni_{80}Mn_{20}$ are unrealistically high due to the distinct Goldschmidt radius for Mn, while σ_{SS} for $Ni_{80}Cr_{20}$, NiFe and NiCoFeCr are significantly lower than the experimental results. $\sigma_{SS}(\delta_{rlx})$ demonstrates that NiCo has negligible σ_{SS}, similar to pure Ni. The hardness values of Ni and NiCo are also close, which are obviously lower than the rest of the CSAs. From the ratio of σ_{SS}/σ, NiCoFeCr and $Ni_{80}Mn_{20}$ exhibit a higher portion of solid solution strengthening than the rest of the CSAs. Results for $Ni_{80}Mn_{20}$ and $Ni_{80}Cr_{20}$ are not compared with literature as these two CSAs are less explored. However, based on our study, they are promising as they demonstrated high hardness (from nanoindentation) and σ_{SS} (Table 3.1). This suggests that the selection of

component elements in CSAs is critical, and more efforts should be devoted to understanding element-specific deformation mechanisms in CSAs for better property combinations.

Table 3.2 Solid Solution Strengthening in Ni and CSAs.

Sample	***E* (GPa) Nanoindentation**	**σ (=H/3) (MPa)**	**δ_G ***	**$\sigma_{SS}(\delta_G)$ (MPa)**	**δ_{rlx} ****	**$\sigma_{SS}(\delta_{rlx})$ (MPa)**	**σ_{SS}/σ**
Ni	184±4	314	0.0000	0.0	0.0000	0.0	0.00
NiCo	174±6	275	0.0040	4.0	0.0027	1.2	0.00
$Ni_{80}Mn_{20}$	191±5	483	0.0425	457.2	0.0191	130.1	0.27
$Ni_{80}Cr_{20}$	205±3	550	0.0096	41.5	0.0155	98.5	0.18
NiFe	153±5	452	0.0119	33.5	0.0167	64.0	0.14
NiCoFeCr	186±2	467	0.0102	47.7	0.0167	109.6	0.24

* Goldschmidt radius: Ni: 1.25 Å; Co: 1.26 Å; Mn: 1.12 Å; Cr: 1.28 Å; Fe: 1.28 Å.

** Atomic radius calculated from atomistic simulations and experiments[60]: Ni: 1.25 Å; Co: 1.25 Å; Mn: 1.31 Å; Cr: 1.29 Å; Fe: 1.29 Å

3.5 Conclusions

A procedure for nanoindentation and nanoindentation strain rate jump tests and data analysis/correction has been developed for exploring Ni-based CSAs. Unique single-crystal FCC Ni, NiCo, $Ni_{80}Cr_{20}$, NiFe and NiCoFeCr, and coarse-grained $Ni_{80}Mn_{20}$ have been compared to understand the strengthening mechanisms, especially for the less explored binary alloys such as $Ni_{80}Cr_{20}$ and $Ni_{80}Mn_{20}$. A data set, including hardness, elastic modulus, strain rate sensitivity, and activation volumes, is provided for Ni-based CSAs. Major conclusions are listed as follows.

- The type of alloying elements is more critical than the number of elements in strengthening: Co does not provide strengthening in Ni, while Cr, Mn, and Fe are effective strengthening elements. Cr is the most effective among all the 3d transition metal elements. The alloying in CSAs simultaneously increases the densities of statistically stored dislocations and geometrically necessary dislocations.

- Pile-ups and indentation size effects are significant in Ni-based CSAs and a correction procedure for accurate hardness was developed. It is suggested that the measured height, h_i instead of contact periphery, a_i should be used to estimate pile-ups for Ni-based CSAs.

- A data set of activation volumes of Ni-based CSA is provided from nanoindentation strain rate jump tests: Ni and Co are similar with a low activation volume for dislocations, while the rest have higher activation volumes. The data are consistent with hardness and dislocation analysis. One special consideration of the indentation size effect is included, i.e., the hardness change rate (unit: Pa/s) is not negligible during strain rate jumping for Ni-based CSAs with strong ISE.

- That lattice distortion from atomic-size difference plays a central role in strengthening, including solid solution strengthening and work hardening, while the stacking fault energy is not critical in our study. The utilization of the solid solution strengthening model developed by Varvenne *et al.* shows that atomic-size difference should be calculated based on the appropriate atomic radius in a relaxed structure from experiments/simulations, instead of the intrinsic Goldschmidt radius.

3.6 Acknowledgements

L.Y. and Y.C. acknowledge financial support by NSF-CMMI 1728554. Y.Z. W.J.W and H.B. were supported as part of Energy Dissipation to Defect Evolution (EDDE), an Energy Frontier Research Center funded by the U.S. Department of Energy, Office of Science, Basic Energy Sciences, under contract number DE-AC05-00OR22725. This work was performed in part at the Analytical Instrumentation Facility (AIF) at North Carolina State University, which is supported by the State of North Carolina and the National Science Foundation (award number ECCS-2025064). L.Y. and Y.C. also acknowledge the discussion and support from Prof. Christopher Evans.

CHAPTER 4 : NANOINDENTATION STUDY ON EARLY-STAGE RADIATION DAMAGE IN SINGLE-PHASE CONCENTRATED SOLID SOLUTION ALLOYS*

4.1 Overview

Concentrated solid solution alloys (CSAs) comprising multiple components have unlocked novel pathways for materials design, particularly in enhancing radiation tolerance. It is imperative to detect early-stage radiation damage in CSAs to gain insights into damage initiation and accumulation mechanisms. In this study, nanoindentation is employed to assess the impact of irradiation on deformation mechanisms in single crystal CSAs, specifically NiCo, NiFe, and NiCoFeCr. It is discovered that pile-up behavior in CSAs significantly affected by irradiation: pile-up induces 10–20 % increase in the contact area before irradiation that is independent of the penetration depth but 20–30 % after irradiation, which substantially affects hardness analyses. Within the context of strain gradient plasticity theory, distinct radiation-induced hardening in three CSAs is interpreted by two components: one is from the radiation-induced defects, and the other is the increase in density of geometrically necessary dislocations (GNDs) associated with indentation size effect (ISE). Quantitative analysis shows that the radiation-induced defects produce obvious hardening in NiFe and NiCoFeCr sample, but not in the NiCo sample. Meanwhile, the irradiation induces a higher GND density in NiCo and NiFe, but not in NiCoFeCr, which is interpreted by the volume change of the plastic zone.

---

* This chapter is reprinted with permission from “Nanoindentation study on early-stage radiation damage in single-phase concentrated solid solution alloys” by L. Yang, Y. Chen, J. Miller, W.J. Weber, H. Bei, Y. Zhang, Materials Science and Engineering: A 908 (2024), 146746.

4.2 Introduction

Structural materials for advanced nuclear energy need to survive in extremely harsh environments of high temperatures, large time-varying stresses, chemically reactive environments, and intense neutron irradiation fields [84, 203]. Concentrated solid solution alloys (CSAs) with multiple components, particularly medium/high entropy alloys (M/HEAs) consisting of three or more elements, have opened up new avenues for materials design [147, 148, 153, 204, 205]. The enhanced mechanical properties [10, 28, 31, 149, 152, 153, 206, 207] and radiation tolerance [85, 151, 156, 208-212] make these alloys potential candidates for structural applications in high-temperature fission and fusion reactors. The mitigated radiation damage in CSAs can be attributed to an increase in chemical disorder, which leads to a substantial reduction in electron mean free path [88], and subsequent localized electron-electron interactions. As such, the electronic temperature in the vicinity of the collision cascades becomes higher and the thermal spike is prolonged, which strengthens the tendency of recombination between vacancies and interstitials (i.e., less survived Frenkel pairs) during radiation cascades, compared to the case of pure metals [213]. Furthermore, the recombination is also enhanced due to sluggish diffusion [94, 168, 214, 215], originating from intrinsic severe lattice distortion, as a consequence of the random distribution of several different-sized atoms in the crystal lattice [89, 92].

While high-dose radiation damage is important to examine the lifetime of new materials under irradiation, the early-stage defect generation and accumulation, which is critical to understanding radiation tolerances, is less experimentally explored. It has been a long-standing challenge to quantify radiation-induced defects at low dose regimes due to the difficulties in quantitatively measuring point defect population and dislocation density, especially when the

penetration depth from irradiation is shallow [216]. Transmission electron microscopy (TEM) can examine dislocation density, but the sample preparation by focused ion beam or ion milling often introduces surface defects (e.g., dislocation loops), which overshadows the low-density radiation-induced dislocations. Ion channel technique exhibits a much weaker response to low-dose irradiation, which is challenging to characterize the early-stage responses of materials [105]. Recently, positron annihilation spectroscopy (PAS) has shown great potential due to its capability of distinguishing an individual number of vacancies [217, 218], but it is not easily accessible. Testing in a high-throughput manner is still demanded.

Nanoindentation is a critical technique for probing mechanical properties at the micrometer and sub-micrometer scales, especially for irradiated surface regions due to the limited volume required for testing [97, 105-108]. Nanoindentation has the advantage of easy sample preparation and statistically rich data sets [163, 164, 219]. When using nanoindentation for in-depth surface property analysis, indentation size effect (ISE) is a critical phenomenon. Several strain gradient plasticity (SGP) theories have been used to interpret ISE [136, 137, 220], among which, the Nix-Gao model [136] as a mechanism-based SGP model is commonly used. In this model, a linear relation between the square of hardness (H^2) and the reciprocal of indentation depth ($1/h$) is predicted. However, irradiation on the surface complicates the nanoindentation measurement as the ISE is superimposed with the radiation effect [221]. This issue has been studied by different groups: Kasada *et al.* [222] showed the Nix-Gao model can be used to achieve the properties of irradiated ferritic alloys; Hosemann *et al.* [106] demonstrated that radiation-induced defects result in a smaller ISE in single-crystal Cu with an assumption that hardness contribution from irradiated and un-irradiated regions underneath the indenter tip is based on their volume fraction; Saleh *et al.* [223] showed that plastic strain contours in irradiated

316 SS exhibit a ‘double dished’ plastic zone profile, which would change hardness measured at different depths; Mattucci *et al.* [224] proposed that higher-density geometrically necessary dislocations (GNDs) are confined in the plastic zone underneath an indenter tip in the irradiated material when compared to that in the non-irradiated materials. Meanwhile, in these studies, a bi-linear relationship with a different slope for the irradiated shallow surface was often found on the H^2- *1/h* curves. It is worth noting that the bi-linear relationship also exists in unirradiated samples, showing different slopes at the microscale and nanoscale, interpreted by different theories [220, 225, 226].

In this study, we strive to understand and quantify the early-stage radiation damage in Ni-based CSAs by nanoindentation. It is hypothesized that the amount of low-dose radiation damage in different alloys near the surface can be correlated to the radiation-induced hardening and ISE. To examine this idea, we employed three single-crystal CSAs (NiCo, NiFe and NiCoFeCr) with same (100) surfaces, but with distinct properties: NiCo is less radiation tolerant than NiFe. NiCoFeCr is the most radiation tolerant. We used a high ion energy of 8 MeV to create an extended low-damage region, which allows a relatively uniform region of irradiation within 1000 nm. As such, radiation-induced hardening and the origin of the change in radiation-induced GND distribution are discussed.

4.3 Materials and methods

In this study, the equiatomic Ni-based single-phase CSAs include binary alloys NiCo and NiFe [96, 97] (with 50at. % Co and 50at. % Fe, respectively) and quaternary alloy NiCoFeCr (25 at.% for each element) were prepared by arc-melting. The arc-melted buttons were flipped and

re-melted at least five times before drop casting to ensure homogeneous mixing. A floating-zone directional solidification method was used for single-crystal growth. Prior to irradiation, all the specimens were mechanically ground using up to #4000 grit SiC sandpaper followed by chemical-mechanical polishing with up to 0.05 μm colloidal silica solution finally achieving the surfaces with roughness below 3 nm to conduct ion irradiations and following tests [168]. These NiCo, NiFe and NiCoFeCr samples have been experimentally confirmed as (100)-oriented high quality single FCC phase crystals with random elements arrangements and eminent crystal perfections [96, 168]. Afterward, radiation process was accomplished at the Ion Beam Material Laboratory (IBML) [146]. All three Ni-based samples (NiCo, NiFe and NiCoFeCr) were irradiated with 8 MeV Ni ions under ambient temperature at a fluence of 1×10^{14} cm^{-2} with a damage of ~ 0.06 dpa (displacements per atom, the unit for damage level) at 500 nm. The depth profiles of radiation damage dose (dpa), using vacancy output files, and implanted Ni ion concentration were obtained by using Stopping and Range of Ion in Matter (SRIM) software. Full cascade option was utilized [227] with 40 eV as the threshold displacement energy for all elements [228].

The nanoindentation was performed on Agilent NanoIndenter G200 (MTS) with a Berkovich diamond tip. The continuous stiffness measurement (CSM) based on the Oliver-Pharr method [163] was chosen to record hardness and elastic modulus values as a function of penetration depth continuously. Fig. 4.1 below shows a representative load-depth curve from an un-irradiated NiCo sample with maximum depth of 1000 nm. The CSM method is used with a frequency of 45 Hz. This technique allows for continuous recording of stiffness during loading, which is schematically demonstrated in the inset.

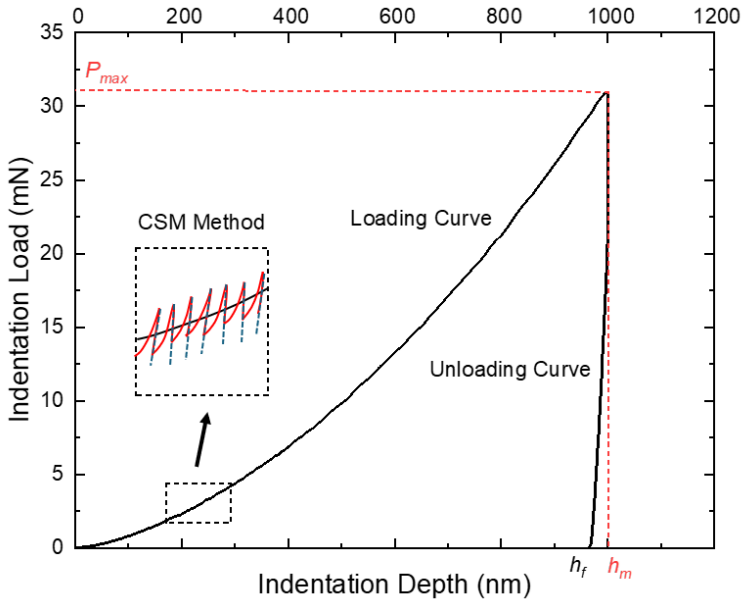

Figure 4.1 Representative load-depth curve of un-irradiated NiCo with maximum indentation depth of 1000 nm. Insets present the schematic demonstration of CSM method.

The contact stiffness (S) is monitored during the loading process, which is defined as the slope of the unloading curve from each dynamic oscillation:

$$S = \left(\frac{dP}{dh}\right)_{unloading} \tag{4.1}$$

The contact depth (h_c) of indentation can be obtained by following the Oliver-Pharr method as:

$$h_c = h_m - 0.75\frac{P_{max}}{S} \tag{4.2}$$

where h_m and P_{max} are maximum depth and maximum indentation load for each loading and unloading cycle. Then the geometrical contact area (A) can be directly calculated from:

$$A = f(h_c) \tag{4.3}$$

In this study, the tip area function was calibrated on a fused silica sample and $A = 22.3852{h_c}^2 + 493.1381h_c$. Therefore, the nanoindentation hardness H can be obtained by:

$$H = \frac{P}{A} \tag{4.4}$$

Meanwhile, the contact stiffness S and contact area A are used to compute the reduced modulus E_r by:

$$E_r = \frac{\sqrt{\pi}}{2}\frac{S}{\sqrt{A}} \tag{4.5}$$

After obtaining this reduced modulus, the nanoindentation modulus E of tested material can be extracted:

$$E = (1 - \upsilon^2)\left[\frac{1}{E_r} - \frac{(1 - \upsilon_i^2)}{E_i}\right]^{-1} \tag{4.6}$$

where υ_i is the Poisson's ratio of the indenter, which is equal to 0.007 and E_i is the elastic modulus of indenter with value of 1140 GPa for diamond. υ is the Poisson's ration of specimen and is set as 0.30 in this study.

For each sample with or without irradiation, four different final penetration depths (i.e., 300 nm, 500 nm, 700 nm, 1000 nm) were selected to correct the pile-ups by Atomic Force Microscopy (AFM, Veeco Dimension 3100 Metrology). Six repeated indents were performed for each experimental setup to evaluate the uncertainty and confirm repeatability. AFM results were analyzed using the open-source software Gwyddion [170].

4.4 Results

4.4.1 Estimated radiation damage profile

A representative damage profile of irradiated sample at 1×10^{14} cm^{-2} fluence is displayed in Fig. 4.2. The radiation damage in units of dpa is a function of radiation depth. The peak dpa in the damage profile is ~ 0.25 *dpa* at a depth of 2100 nm. The depth of interest (<1000 nm) exhibits low damage of less than 0.1 dpa: the radiation damage is 0.05 dpa, 0.06 dpa, 0.07 dpa, 0.08 dpa for interested penetration depths of 300, 500, 700 and 1000 nm, respectively. The composition change and impact on microstructural evolution from implanted ion (Ni) is negligible as the peak concentration of implanted Ni is 0.0017% at a depth of 2500 nm.

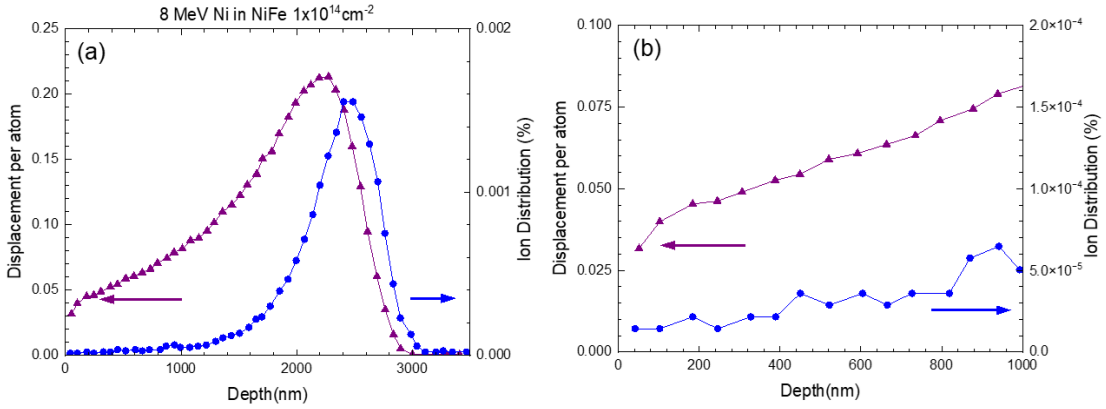

Figure 4.2 (a) SRIM predicted profile for radiation damage and implanted Ni ion distribution of NiFe sample. (b) the magnified region in (a) for a depth less than 1000 nm.

4.4.2 Nanoindentation analysis

The CSM method shows a continuous variation of hardness and elastic modulus values as a function of penetration depth. A custom stiffness value of 125 N/m was used as the threshold value for surface detection. The hardness of un-irradiated and irradiated NiCo, NiFe and NiCoFeCr are compared in Fig. 4.3a-c respectively. The continuous solid lines were obtained

from nanoindentation tests with a maximum displacement of 1000 nm, and the shadow areas represent the standard deviation. To examine the effect of penetration depth on pile-ups, indents at different final penetration depths (300, 500, 700 and 1000 nm) were examined by AFM. Although the tests were done by CSM, only the data at the final penetration depth from the tests are demonstrated for clarity (scattered points with error bars in Fig. 4.3). It is clear that the results collected from 300-700 nm final penetration depths are consistent with those finished at 1000 nm.

An obvious decrease in hardness with the increase in penetration depth is observed for un-irradiated and irradiated NiCo, NiFe and NiCoFeCr, which will be discussed later. Radiation-induced hardening is clear for three samples and is more obvious at shallow penetration depths; the general trend shows more significant hardening at shallower surfaces. Before irradiation, NiCoFeCr sample presents the highest hardness while NiCo is softest, consistent with our previous study [229]. Irradiation induces more severe hardening in NiCo at a shallower depth (e.g., 300 nm). The phenomenon that hardness decreases with depth is affected by three typical factors: (1) the ISE caused by strain gradient, (2) the evolution of pile-up amount, and (3) the change of intrinsic properties with depth, i.e., due to irradiation in this case. In this study, a high acceleration voltage (8 MeV Ni ions) and low Ni ion fluence created relatively uniform radiation damage to minimize the change of intrinsic properties with depth, and we assume the change of radiation-induced defects at the depth of interest is negligible.

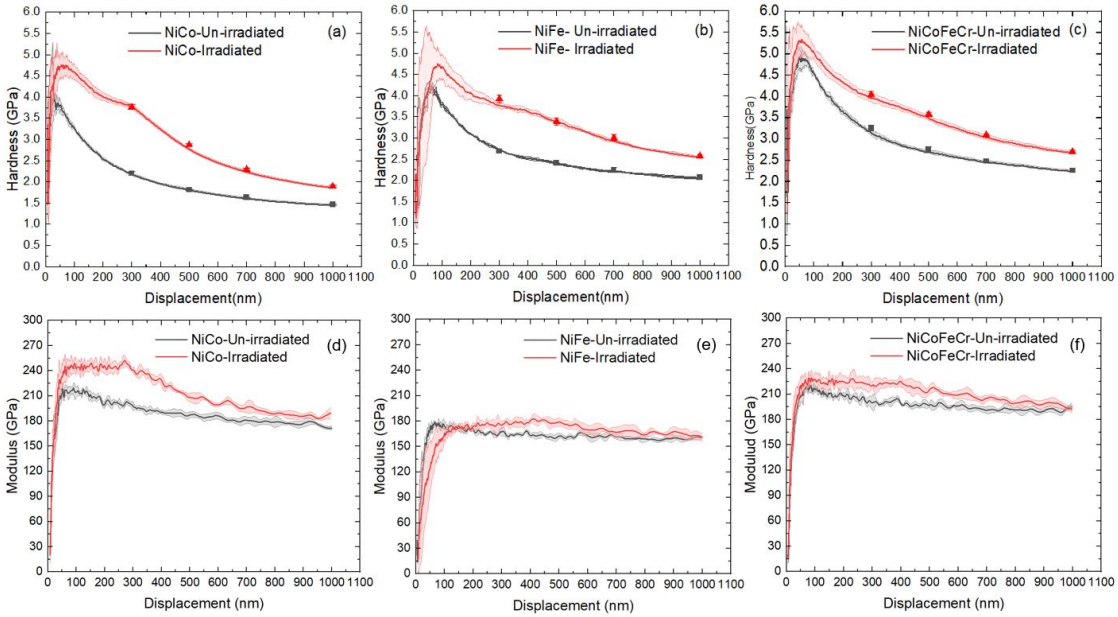

Figure 4.3 Summary of continuous and scattered (a-c) hardness and (d-f) elastic modulus results of NiCo, NiFe and NiCoFeCr before and after irradiation. The shade areas represent the standard deviation of six indentations.

Meanwhile, the continuous elastic modulus results were also collected from nanoindentation tests with a maximum depth of 1000 nm. The elastic modulus is a fundamental material property that reflects a material's resistance to elastic deformation, which is less sensitive to surface conditions than hardness. It is often provided to confirm the reliability of data collection. We noticed a decrease in modulus with depth, especially at depths below 500 nm (Fig. 4.3d-f). This might be from the pile-up behavior at different depths, which affects the actual contact area between the indentation tip and substrate and subsequently affects the measurement of hardness and modulus, especially for irradiated samples [174, 224, 229-232].

4.4.3 Pile-up examination

To investigate pile-up behavior under different penetration depths, irradiation, and alloying conditions, the surface morphology near the indentation imprints with penetration depths of 300, 500, 700, and 1000 nm was examined by AFM for un-irradiated and irradiated NiCo, NiFe and NiCoFeCr (complete AFM images are summarized in Supplementary). One pile-up example on NiCoFeCr sample before and after irradiation at 500 nm is shown in Fig. 4.4. Pile-ups are obvious in both samples, but a higher pile-up in irradiated NiCoFeCr can be observed. Quantitative characterization of pile-ups will be discussed as follows.

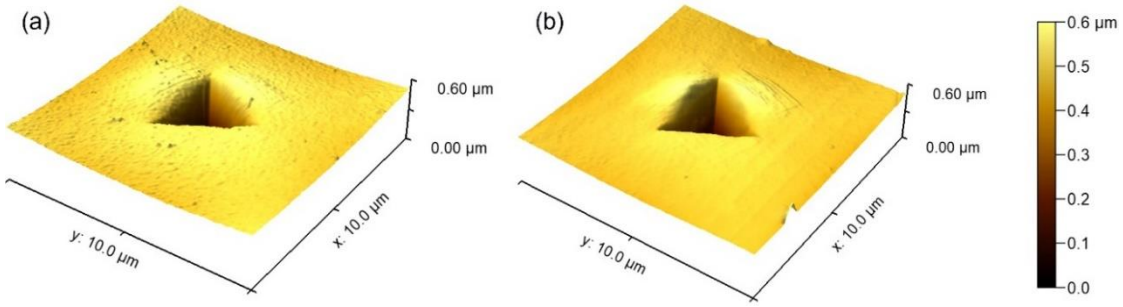

Figure 4.4 AFM micrographs of indentation imprints for NiCoFeCr sample penetrated to 500 nm (a) before irradiation and (b) after irradiation.

There are several pile-up correction methods in the literature [174-176]. In this study, Kese's semi-ellipse method [177, 178] based on real surface morphology analysis near the imprints is employed. The corrected contact areas A_C is composed of geometrical contact area (A) obtained from the Oliver and Pharr analysis of nanoindentation data and pile-up area (A_{pu}) as written as below,

$$A_C = A + A_{pu} \tag{4.7}$$

In this study, $A = 22.3852h^2 + 493.1381h$. A_{pu} is calculated as the sum of projection area along three edges following the work from Kese *et al*.[177]:

$$A_{pu} = \frac{\pi l}{4} \sum a_i \tag{4.8}$$

where l is the edge length of the residual imprint of the Berkovich indenter characterized by AFM, a_i is the horizontal distance from the edge of the indent to the actual contact periphery, which is estimated by $a_i = h_i \cdot tan65.3^{\circ}$.

As such, the pile-up can be quantified by A_C/A, which is often termed as pile-up correction factor to reflect the relative ability to form pile-up during the deformation. Fig. 4.5 shows that A_C/A reaches 1.1-1.2 for un-irradiated samples without an obvious dependence on penetration depth. After irradiation, A_C/A increases to 1.2-1.3 at shallow surfaces of less than 500 nm but retains a similar pile-up level beyond 500 nm. This significant change in contact area requires correction for subsequent hardness analyses. A higher amount of pile-up after irradiation is expected as irradiation usually lowers the work-hardening capability of alloys due to radiation-induced defects [224, 233]. A lower capability for work hardening is not able to drive plastic zone into deeper depths and thereby increase the amount of pile-up adjacent to indenter [234]. Besides, studies [166, 235] have reported the behavior of pile-up and sink-in depends on the factor E/σ_Y, where σ_Y is yield stress and E is elastic modulus. A higher E/σ_Y ratio of materials promotes the pile-up, particularly in materials with high work-hardening, while a lower ratio favors sink-in.

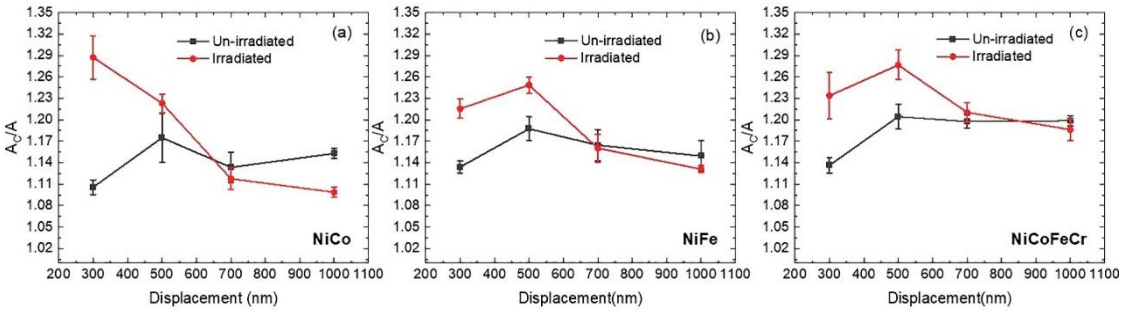

Figure 4.5 Pile-up correction factors and tendencies of various samples at 300, 500, 700 and 1000 nm penetration depths: (a) NiCo (b) NiFe (c) NiCoFeCr.

4.4.4 Corrected hardness and modulus analysis

With the calculated A_C/A at different depths for different alloys, the pile-up corrected hardness values H_C can be obtained by the relation:

$$\frac{A_C}{A} = \frac{H}{H_C} \tag{4.9}$$

And elastic modulus can be corrected via equation:

$$\frac{\sqrt{A_C}}{\sqrt{A}} = \frac{E}{E_C} \tag{4.10}$$

As shown in Fig. 4.6a-c, all hardness values are lowered after pile-up correction. The dash and solid lines represent the hardness values before and after pile-up correction. Meanwhile, after pile-up correction, the elastic modulus is less penetration depth dependent (Fig. 4.6d-f).

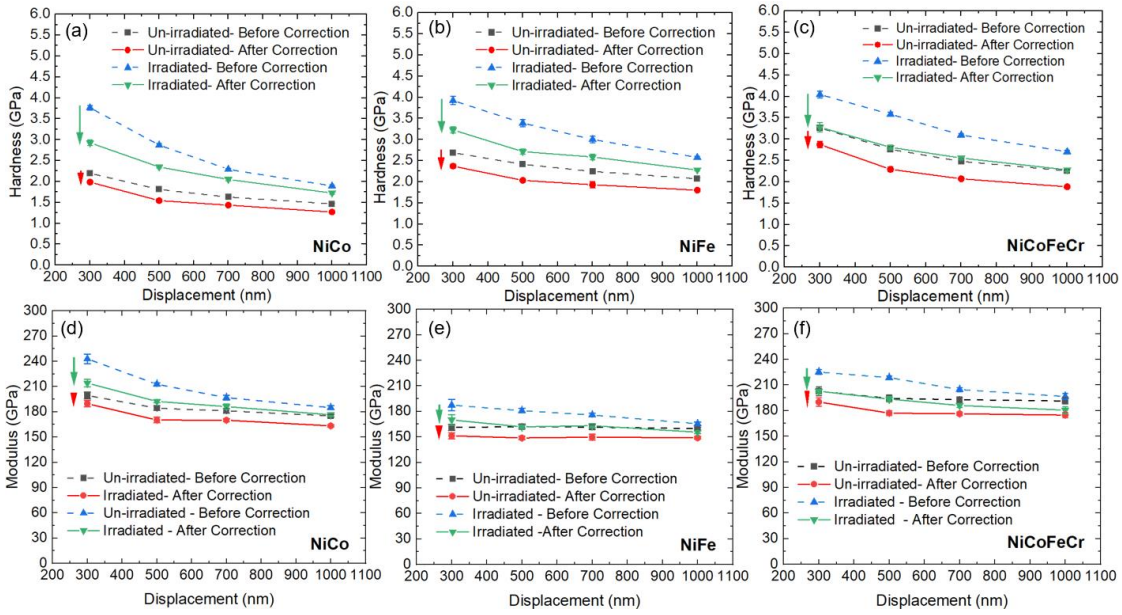

Figure 4.6 Comparisons of (a-c) nanoindentation hardness and (d-f) elastic modulus results before and after pile-up corrections for NiCo, NiFe and NiCoFeCr, respectively. Error bars are provided in all data points.

Nix-Gao model [136] describes the relationship between nanoindentation hardness (H) and macro-hardness (H_0) as

$$H = H_0\sqrt{1+\frac{h^*}{h}} \tag{4.11}$$

where h represents penetration depth and $h^*$is defined as characteristic depth. The equation can be rewritten as $H^2 = H_0^2 + H_0^2 h^*/h$ and the data are replotted as H^2 versus $1/h$. H_0^2 can be obtained from the linear intercept, and the slope is $H_0^2 h^*$. As shown in Fig. 4.7a-c, for the un-irradiated samples, a linear relationship is observed for three samples, which is anticipated [229]. However, all the fitting curves of irradiated samples before pile-up corrections present a bi-linearity. The bi-linearity in irradiated samples could be ascribed to the effect of a hard irradiated layer on a soft substrate, in which the plastic zone induced by the indenter is constrained within the irradiated layer at the early stage of nanoindentation measurement [222, 236]. However, this

does not apply in our cases; the bi-linearity of irradiated samples disappears after the pile-up correction. Therefore, for un-irradiated samples, pile-up correction lowers the hardness values but doesn't change the linearity of the plot, but irradiation induces the bi-linearity in three CSAs due to severe pile-ups in irradiated samples. For convenience of comparison, the corrected data are replotted and fitted in Fig. 4.8.

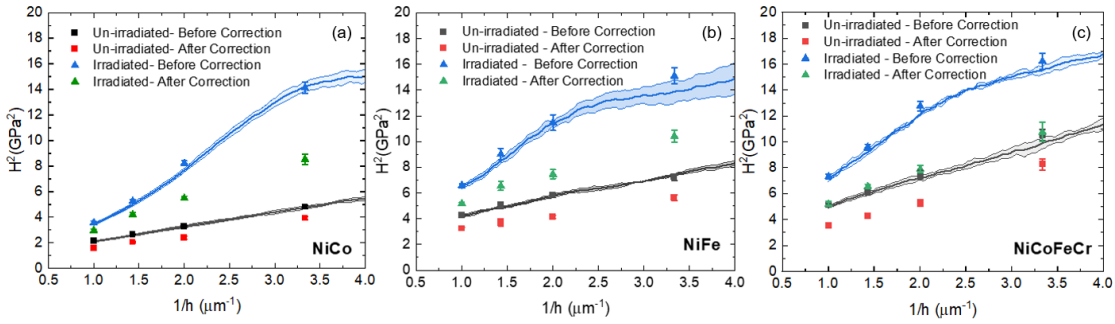

Figure 4.7 Nanoindentation results plotted by H^2 versus $1/h$ for un-irradiated and irradiated samples before and after pile-up correction: (a) NiCo (b) NiFe (c) NiCoFeCr. The shade areas represent the standard deviation of six indentations.

According to the Nix-Gao model in Eqn. 4.11, the intercept H_0^2 and the slope associated with the characteristic depth, h^* are obtained from the linear fitting. Fig. 4.8d summarizes H_0 and h^* based on Eqn. 4.11. Interestingly, three alloys show distinct features. For NiCo, the intercept only slightly changes after irradiation, while the slope changes dramatically from 0.97 to 2.47; For NiFe, the intercept mildly increases and there is also a significant change in slope (0.98 to 2.28); For NiCoFeCr, there is an obvious increase in the intercept, but the slope change is less significant (1.91 to 2.53).

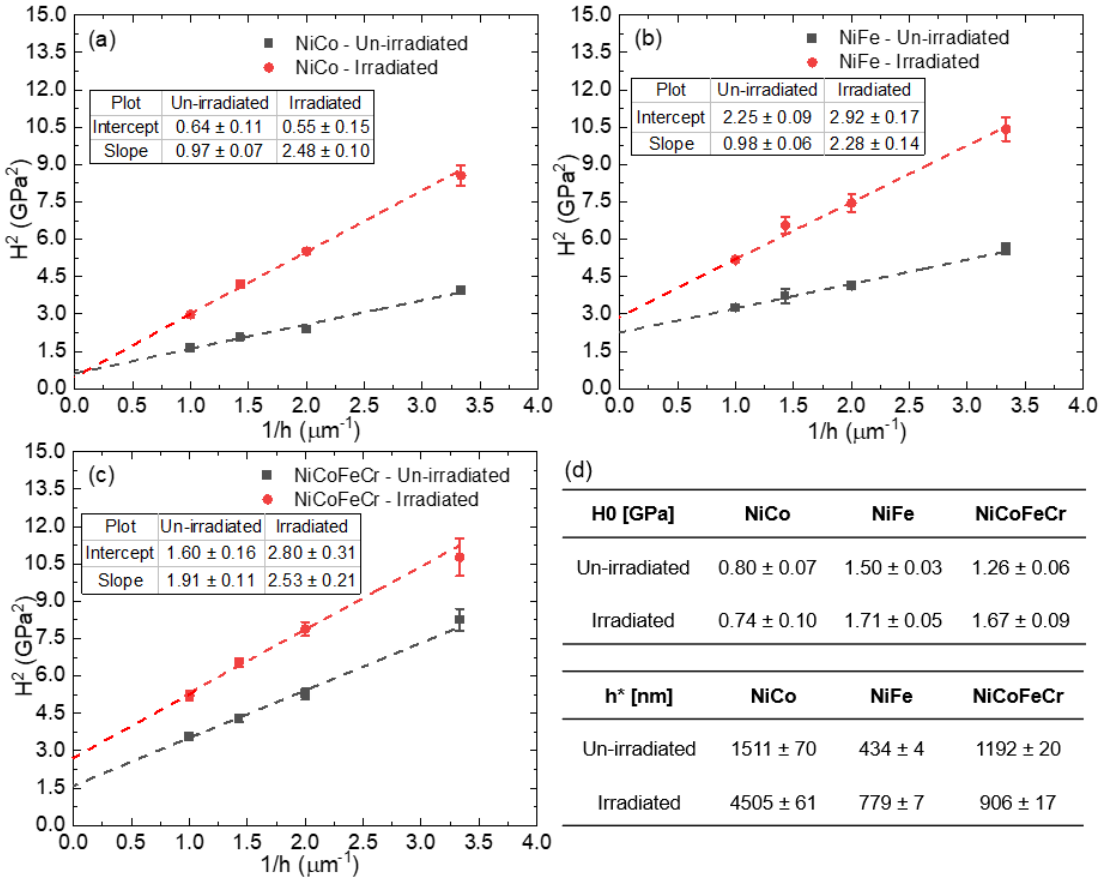

(d)

H0 [GPa]	NiCo	NiFe	NiCoFeCr
Un-irradiated	0.80 ± 0.07	1.50 ± 0.03	1.26 ± 0.06
Irradiated	0.74 ± 0.10	1.71 ± 0.05	1.67 ± 0.09

h* [nm]	NiCo	NiFe	NiCoFeCr
Un-irradiated	1511 ± 70	434 ± 4	1192 ± 20
Irradiated	4505 ± 61	779 ± 7	906 ± 17

Figure 4.8 (a-c) Nix-Gao fitting results of NiCo, NiFe and NiCoFeCr samples after pile-up corrections. (d) summarization of macro-hardness values H_0 and characteristic depth h* of NiCo, NiFe and NiCoFeCr.

4.5 Discussion

4.5.1 Radiation-induced hardening

The radiation-induced hardening has two components: (a) the strength from radiation-induced defects and (b) the additional hardness induced by the change in GND density due to irradiation. The first hardening component can be calculated from the discrepancy of H_0 before and after irradiation:

$$\Delta H_0 = H_{0_{irradiated}} - H_{0_{un-irradiated}} \tag{4.12}$$

These H_0 values have been pile-up corrected and summarized in Fig. 4.8. Note that radiation-induced defects are important in strengthening NiFe and NiCoFeCr, which produce 0.21 and 0.41 GPa hardness increments, respectively. However, there is no hardening from radiation-induced defects in NiCo samples.

Meanwhile, the second component, i.e., the additional hardness induced by the change in GND density (ΔH_{GND}) can be calculated by the relation:

$$\Delta H_{GND} + \Delta H_0 = H_{irradiated} - H_{un-irradiated} \tag{4.13}$$

where $H_{un\_irradiated}$ and $H_{irradiated}$ are the pile-up corrected harnesses of the un-irradiated and irradiated samples, respectively. Using Eqn. 4.13, ΔH_{GND} at different depths for three alloys is obtained (Fig. 4.9). Irradiation leads to a significant increase in ΔH_{GND} for NiCo, reaching as high as 1 GPa at a depth of 300 nm and 0.6 GPa at 1000 nm. Similarly, NiFe experiences an increase in ΔH_{GND} due to irradiation, with values of 0.6 GPa at 300 nm and 0.3 GPa at 1000 nm. However, irradiation has minimal impact on the behavior of GNDs in the NiCoFeCr sample, as ΔH_{GND} is close to 0.

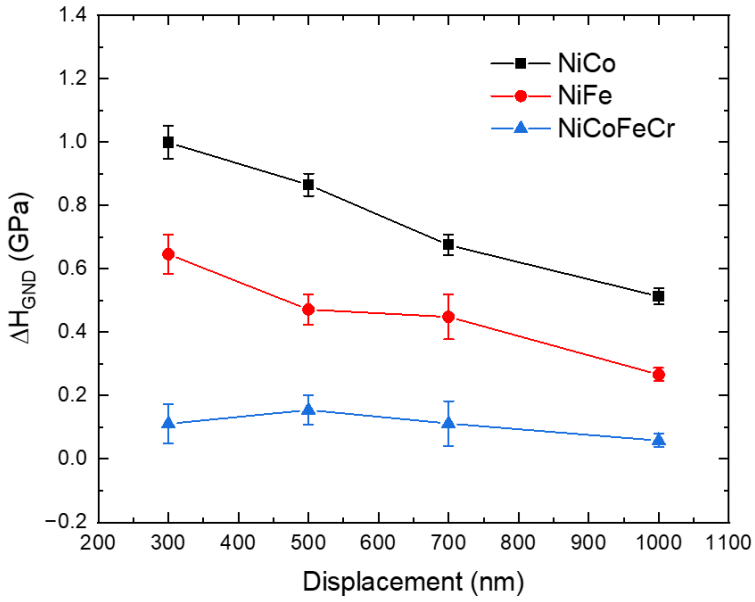

Figure 4.9 Hardness induced by the change in GND density in irradiated NiCo, NiFe and NiCoFeCr.

4.5.2 Radiation-induced dislocation density changes

The increase in dislocation density leads to higher flow stress of the materials. During nanoindentation, two types of dislocations are considered: GNDs and statistically stored dislocations (SSD) [180, 181]. The SSD density is often considered as a constant at different depths, while GND density increases when it is close to surface [225]. Combined with the Taylor relation [237], the hardness is estimated by SSD density, ρ_s and GND density, ρ_G [137] :

$$H \approx \mu b[\rho_S + \rho_G]^{\frac{1}{2}} \tag{4.14}$$

where, μ is shear modulus from nanoindentation and b represents Burgers vector. The hardness associated with ρ_s is denoted by H_0, which can be obtained directly from Nix-Gao model fitting (Fig. 4.8).

For irradiated samples, additional radiation-induced defects contribute to hardening. Mattucci *et al.* [224] provided a method to decompose different contributing factors, and based on the framework, the size dependent measured hardness of the irradiated material could be written as:

$$H_{irradiated} = \mu b[\rho_s + \rho_G]^{\frac{1}{2}} + \Delta H_0 \tag{4.15}$$

Here, the first term and second term in the bracket are SSD density and GND density after irradiation. ΔH_0 is the hardness from radiation-induced defects. Note that it is often assumed that SSD density doesn't change after irradiation[224], so the SSD density, ρ_s, associated with macro-hardness for both un-irradiated and irradiated samples can be directly calculated by $H_{0_{un-irradiated}}/\mu^2 b^2$. The ρ_s for NiCo, NiFe and NiCoFeCr samples are $2.3 \times 10^{15}/m^2$, $1.1 \times 10^{16}/m^2$ and $5.4 \times 10^{15}/m^2$ respectively. As such, ρ_G in irradiated CSAs at different depth can be computed by using Eqn. 4.15. The density changes of GNDs owing to irradiation are summarized in Fig. 4.10. Overall, the distribution of GNDs is depth dependent, with density increasing along with the decrease in depth. On the other hand, irradiation has different impacts on the GND density changes in different samples. The GND densities of NiCo and NiFe show a significant increase after irradiation. However, the irradiation had minimal influence on GND density of NiCoFeCr throughout the testing depths.

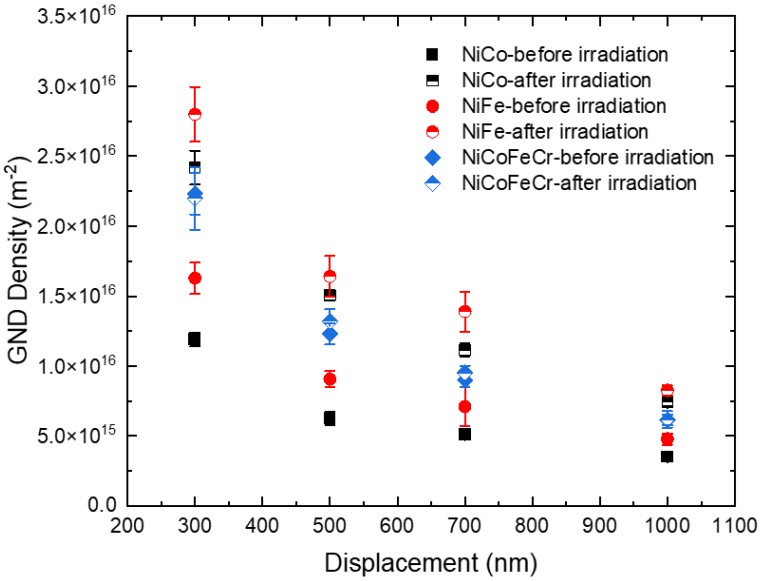

Figure 4.10 GND densities in NiCo, NiFe and NiCoFeCr samples before and after irradiation.

4.5.3 The volume of plastic zone in irradiated CSAs

The volume of the plastic zone is a critical value that determines the GND density (number of dislocations divided by the volume of plastic zone), which is reviewed as follows. The pioneering study of plastic zone is based on the expanding cavity model by Johnson [238], based on Hill's solution [239], in which the plastic volume is defined as the region where the strain level is high enough to initiate plastic deformation. The volume estimation is consistent with dislocation density from the TEM observation by Fivel *et al.* for shallow spherical indentation [240]. The Nix-Gao model, which is commonly used to capture ISE [136] assumes that the plastic zone is a hemisphere with a radius equal to the contact radius (a). Finite element simulations could provide a more accurate estimation of the radius of the plastic zone as fa, where f is a constant approximately ranging, depending on the material, from zero to 3.5 [180].

It is important to note that there has been a debate regarding the interpretation of ISE using strain gradient theory and GND density. Several research groups have investigated GND

density underneath indenter tip using different techniques, such as electron backscatter diffraction (Kiener *et al.* [241], Rester *et al.* [172] and Demir *et al.* [242]), transmission electron microscopy (McLaughlin and Clegg [243]) and atomistic simulation (Yaghoobi and Voyiadjis [244]), showing that GND density alone may not adequately capture ISE for small indentation depths. However, Feng *et al.* [245] used synchrotron X-ray microdiffraction to confirm that GND density can capture ISE. More recently, Ma *et al.* [171] show that in Ni, dislocations are relatively more far-reaching in shallower indents (50-200 nm) and become gradually confined as indentation depth increases. Beyond 300-400 nm, the hardness values follow the Nix-Gao fitting, which suggests that the hemispherical plastic zone underneath the indenter tip is still a valid simplification, although the influence of indenter tip geometry and anisotropy of materials properties are ignored.

Following the assumption of Nix-Gao model, the distribution of GNDs is constrained within a hemispherical zone with a volume of

$$V_{un-irradiated} = \frac{2}{3}\pi a^3 \tag{4.16}$$

We further assume that the plastic zone in irradiated sample upon indentation will be smaller, which is achieved by maintaining the surface contact area but reducing the migration distance. The plastic zone shape transforms into a spherical cap in irradiated samples (Fig. 4.11). The base surface area of spherical cap is same as that of ideal hemisphere, while the height of cap (h_S) varies due to materials and irradiation. As such, the volume of plastic zone becomes:

$$V_{irradiated} = \frac{1}{6}\pi h_S\left(3a^2 + {h_S}^2\right) \tag{4.17}$$

Therefore, radiation-induced volume change can be obtained from GND density by

$$\frac{V_{un\_irradiated}}{V_{irradiated}} = \frac{\rho_{G\_un-irradiated}}{\rho_{G\_irradiated}} \tag{4.18}$$

The ratio "h_S/a" is defined to quantitively compare the dimension decrease of plastic zone after irradiation. Combining with Eqns. 4.16 and 4.17, the effective radius of irradiated NiCo, NiFe and NiCoFeCr can be calculated and are demonstrated schematically in Fig. 4.11. As hypothesized, the plastic zone is the ideal hemi-sphere with radius of *a* prior to irradiation. After irradiation, the shape of plastic zone switches to smaller spherical cap, with height of 0.56a for NiCo and to 0.65a for NiFe, respectively. The cap height in NiCoFeCr is close to that prior to irradiation, with a value of 0.96a.

Lastly, it is interesting to find that irradiation leads to the smallest plastic zone in NiCo while the largest in NiCoFeCr. Meanwhile, note that at the early stage, irradiation induces point defects and dislocations might not have been generated yet. We observed that a lower strengthening from radiation-induced defects in NiCo, which is in contrast to the fact that NiCoFeCr has lower point defects due to enhanced point defect recombination [89]. More experimental evidence, particularly the microstructural evidence underneath the indenter tip at different depths for different alloys before and after irradiation, is needed for further understanding and validation of these models.

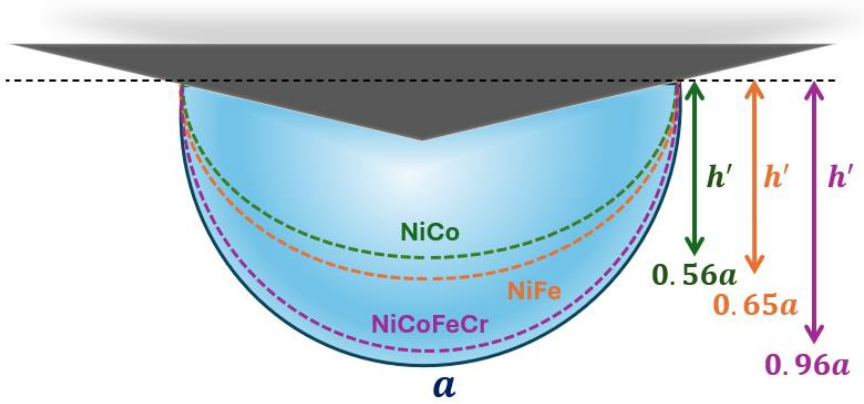

Figure 4.11 Schematic drawing of plastic zone underneath the indenter during indentation, including an ideal hemi-sphere with radius of a prior to irradiation and the "effective radius" of irradiated NiCo, NiFe and NiCoFeCr.

4.6 Conclusions

Nanoindentation is employed to detect and understand the early-stage radiation damage on single-crystal NiCo, NiFe and NiCoFeCr with (100) surfaces in a quantitative manner. The radiation damage is low, less than 0.1 dpa within 1000 nm of the surface. A nearly uniformly damaged surface is achieved by using a high energy (8 MeV) heavy ion irradiation. Major findings and conclusions are summarized as follows:

(a) Pile-ups are not negligible for both un-irradiated and irradiated alloys. The comparison of pile-ups at depths of 300, 500, 700 and 1000 nm for all alloys before and after irradiations shows that pile-up increases the contact area by 10-20% for un-irradiated NiCo, NiFe and NiCoFeCr that does not depend on penetration depth. However, irradiation results in a more severe pile-up, amplifying this effect to 20-30%.

(b) The radiation-induced phenomenon of bi-linearity in the depth range of 300-1000 nm using Nix-Gao fitting model is due to the more severe pile-ups in the shallow surface of irradiated samples. The linear relationship is restored after the pile-up correction.

(c) The radiation-induced hardening in concentrated solid solution alloys (CSAs) originates from two components: one is from the radiation-induced defects, and the other is the increase in GND density. The radiation-induced defects produce obvious hardening in NiFe and NiCoFeCr while not showing a positive effect in NiCo. Meanwhile, the irradiation induces a higher GND density in NiCo and NiFe, but not in NiCoFeCr, which is interpreted by the volume change of the plastic zone. The volume of the plastic zone is significantly smaller in irradiated NiCo and NiFe than in unirradiated ones, while for NiCoFeCr, irradiation doesn't change the plastic zone significantly.

4.7 Acknowledgments

L.Y. and Y.C. acknowledge partial financial support by NSF-CMMI 1728554. YZ is supported through the Laboratory Directed Research and Development Program at Idaho National Laboratory under the Department of Energy (DOE) Idaho Operations Office (an agency of the U.S. Government) Contract DE-AC07-05ID145142.

CHAPTER 5 : INVESTIGATION OF RADIATION RESPONSE AND MECHANICAL BEHAVIOR OF NI-CONCENTRATED SOLID SOLUTION ALLOYS BY FLAT PUNCH INDENTATION

5.1 Overview

Surface property detection is critical to understanding the materials performance, especially for nuclear reactor structural materials development as the ion irradiation damage is shallow and the volume is not sufficient for standard testing. Nanoindentation is capable of capturing hardness and modulus in a non-destructive and high-throughput manner. However, nanoindentation generally uses Berkovich indenter tip and cannot produce data to be converted into uniaxial stress-strain curve for easy evaluation of materials properties. In this study, flat-punch indentation with 1μm in diameter is employed to assess the mechanical behaviors and radiation response of two concentrated solid-solution alloys, NiCo and NiCoFeCr. We first successfully developed a protocol based on Hay's method to obtain a stress-strain curve when thermal drift is of concern. The radiation hardening is obvious in both NiCo and NiCoFeCr, but NiCoFeCr shows less hardening and less radiation dose dependence. Meanwhile, strain hardening capability degrades due to irradiation in both NiCo and NiCoFeCr, and the degradation is less severe in NiCoFeCr: the strain hardening exponents of NiCo reduce from 0.56 to 0.35 up to 0.3 dpa while that of NiCoFeCr slightly decrease from 0.49 to 0.41. This indicates that flat punch nanoindentation could be an important tool to understand the radiation-induced property degradation and accelerate new alloy developments.

5.2 Introduction

Nanoindentation has been widely used to probe the mechanical degradation of surface layers [246]. It is particularly attractive for studies on ion irradiation damage for nuclear

applications because the irradiation-damaged layer is typically thin, less than one micrometer [105, 230, 231, 247]. Hardness and elastic modulus are two mostly acquired mechanical properties from nanoindentation [163, 248]. However, it is demanding to exact more mechanical behavior during nanoindentation, especially when the conventional testing is not accessible due to the sample dimension.

Efforts have been devoted to employing different indenter tip geometry and dimensions to explore mechanical behavior at different stress states and length scales in a high-throughput manner. Researchers strive to obtain uniaxial stress-strain curves as they provide complete elastic and plastic regions. Tabor [123] and other following studies [238, 249-254] provides theoretical models to exact true stress-strain curves from spherical indentation. This was experimentally validated in 6061-T6 alloys by Herbert *et al.* [255] as well as other materials systems [256, 257]. Studies show that the elastic region is shorter in spherical indentation than in uniaxial tensile testing [132], and it is challenging to determine the onset of plasticity [132, 258]. It is worth emphasizing that the deformation volume in spherical nanoindentation grows quickly with depth. This is especially an issue for materials with heterogeneity, e.g., irradiated-damaged layers with defects.

Micro-pillar compression is a method developed to provide a uniaxial compressive stress-strain relationship [259-264]. However, this technique has its own issues, such as time-consuming focused ion-beam milling, surface ion damage, surface effect, and tapered pillar geometry. Recently, the flat punch indentation has attracted more attention as the fixed contact area simplifies the strain and stress analysis; the volume involved in deformation can be assumed as unchanged throughout the test. Hay *et al.* proposed a method to obtain a stress-strain curve by correcting the stress level using the ratio loading and unloading stiffness [258].

We strive to use flat punch nanoindentation to extract stress-strain curves to accelerate new alloy development for nuclear reactor structural materials. Ni-based concentrated solid-solution alloys (CSAs) without one dominant principal element, e.g., NiCo, NiCoFeCr, are new alloys that potentially have simultaneous great mechanical properties and radiation tolerance, especially at elevated temperatures [156, 168, 215]. The deformation mechanisms and the surface damage have been studied by Berkovich nanoindentation elsewhere [229, 265]. However, the stress-strain curve from nanoindentation is still required for better understanding the alloy strengthening and radiation-induced hardening. In this study, we will develop a procedure for extracting stress-strain curves based on the model developed by Hay [258].As the indenter tip in our study (1μm in diameter) is much smaller than Hay's experiments (10 μm), thermal drift will be additionally considered in our study. As such, the elastic-plastic deformation of different alloys and the role of radiation damage will be investigated.

5.3 Experimental

5.3.1 Materials synthesis and ion irradiation

In this study, the equiatomic Ni-based single-phase CSAs binary alloys NiFe [96, 168] (50at. % for each element) and quaternary alloy NiCoFeCr (25 at. % for each element) were prepared by arc-melting. And the floating-zone directional solidification method was used for single-crystal growth. These samples have been experimentally confirmed as (100)-oriented single FCC-phase crystals. [96, 168]. All samples were mechanically ground and chemically polished to produce damage-free surfaces to conduct ion irradiations and following tests. Afterward, radiation processes were accomplished at the Ion Beam Material Laboratory (IBML)

at the University of Tennessee, Knoxville. All samples were irradiated with 8 MeV Ni ions under ambient temperature to the fluence of from 1×10^{12} cm^{-2} to 5×10^{14} cm^{-2}. This MeV Ni ion irradiation induces a similar recoil spectrum to fast neutrons but will not introduce transmutations that leads to high radioactivity [266]. Here, we designed the radiation experiments to allow the un-irradiated/virgin area and irradiated region with 5 different radiation fluences close to each other, as schematically shown in Fig. 5.1. As such, the differences in different batches of samples can be avoided. The radiation damage levels were estimated by using Stopping and Range of Ion in Matter (SRIM) software assuming 40 eV as the threshold of displacement energy for all elements [228]. The corresponding estimated radiation damage values at 500nm for 5 radiated areas are ~0.0006 *dpa*, ~0.003 *dpa*, ~0.015 *dpa*, ~0.06 *dpa* and ~0.3 *dpa*, respectively.

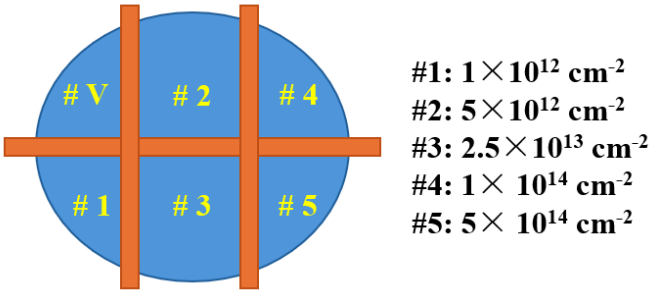

Figure 5.1 Sample arrangements for ion irradiation in this study: total 6 portions with different radiation exposure conditions.

5.3.2 Flat punch indentation

Flat punch nanoindentation was performed under room temperature using the SEM Pico indenter system (PI88, Hysitron) with a 1 μm-diameter flat punch indenter, sitting inside the SEM chamber (JEOL 6480, JEOL). The in-situ nanoindentation tests were conducted under the displacement control mode with the maximum displacement of 250 nm. The loading rate and

unloading rate were fixed at 5nm/sec, and the data acquisition rate was 200 points/sec. Five repeated indents were performed for each area to confirm the repeatability. In addition, the load-depth curves were automatically recorded by the TriboScan software. The hardness and modulus were collected by ex-situ nanoindentation on Agilent NanoIndenter G200 with the Berkovich tip, which has been reported in [229, 265]. The continuous stiffness measurement proposed by Oliver and Pharr [163] was employed to record the hardness values as a function of indentation depth. The tip area function was also carefully calibrated using fused silica sample. For each area with or without irradiation, six indentations were performed to minimize the uncertainty, and the maximum penetration depth was fixed at 2000 nm.

5.4 Results

5.4.1 Thermal drift correction and contact point determination

Thermal drift refers to the indenter drift due to the temperature variations, such as environmental temperature changes or the heat generated during indentation. Thermal drift rate has to be considered when it is close to the scale of penetration depth. For flat punch nanoindentation, the thermal drift rate of typically ~ 1 nm/sec would affect the strain significantly especially with a relationally small tip in 1μm diameter. Indentation instrumentation often includes a module to monitor the thermal drift rate and launch the test when it decreases to an acceptable value (like the Hysitron PI88 platform). Nevertheless, this is often not sufficient. For flat punch nanoindentation, the yielding occurs early due to the stress concentration underneath the tip. We propose that if the unloading cannot provide the correct stiffness, a correction is needed by using the accurate modulus acquired by Berkovich nanoindentation. Here, we assume that the drift rate doesn't change during the entire testing. As shown in Fig.

5.2a, the 90% (P_1, d_1) and 60% of peak load (P_2, d_2) datapoints in unloading part are used to manipulate the thermal drift rate. Now, the stiffness measured from indentation can be determined as:

Now, the stiffness measured from indentation can be determined as:

$$S_{measured} = \frac{P_1 - P_2}{d_1 - d_2} \tag{5.1}$$

And the theoretical stiffness is associated with elastic modulus, based on Sneddon's theory [267]:

$$S_{theoretical} = \frac{E \cdot 2a}{1 - v^2} \tag{5.2}$$

where E is the elastic modulus, a is the radius of indenter, v is the Poisson's ratio. With known elastic modulus as input, theoretical stiffness can be obtained.

By compensating the effect of thermal drift, the relation between measured depth and theorical depth can be expressed as:

$$d_{measured} = d_{theoritical} + \dot{\varepsilon}_T \Delta t \tag{5.3}$$

where $\dot{\varepsilon}_T$ is the thermal drift, which is simplified as a constant during indentation. And Δt is the duration of two datapoints. Combining Eqns. 5.1, 5.2 and 5.3, the thermal drift can be obtained.

Fig. 5.2b presents an example of load-displacement curves using NiCo sample before and after thermal drift correction. In this specific example, the calculated thermal drift rate $\dot{\varepsilon}_T$ is 1.78 nm/s. The stiffness is corrected back to the theoretical stiffness. The stiffness before drift is measured as ~ 98 μN/nm and after drift correction, it is measured as ~ 174 μN/nm, which is close to the theoretical stiffness value (189 μN/nm) obtained by Eqn. 5. 2. From this, it can be seen

that the thermal drift correction cannot be neglected, especially when nanoindentation is employed. The calculated thermal drift rates $\dot{\varepsilon}_T$ for our measurements is around 1-2.3 nm/sec.

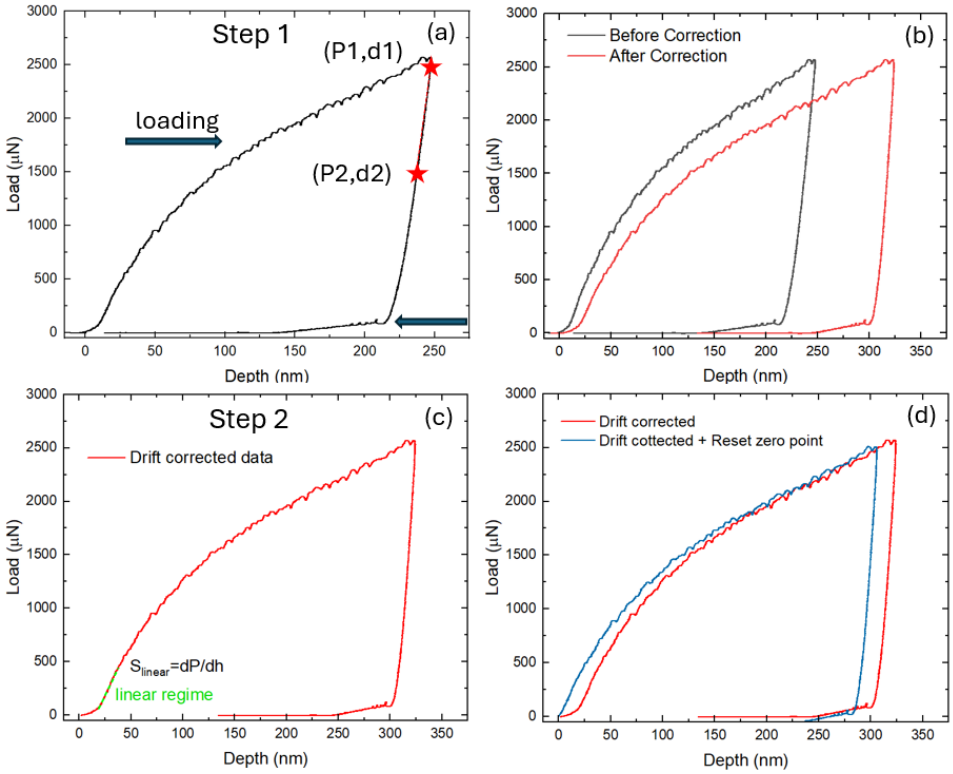

Figure 5.2 Two steps of corrections of load-depth curves (datapoints from NiCo). (a) demonstration of thermal drift correction. (b) comparison of raw data and thermal drift corrected results. (c) criterion of contact point determination. (d) curves after reset the zero point.

The other issue to address is the determination of a full contact point. A stiffness criterion is used in this study. Theoretically, at full contact, the stiffness reaches $2Ea$ during elastic deformation [267]. However, due to the unevenness of the indenter and sample surfaces, as well as the early plastic deformation due to stress concentration from the tip, the stiffness cannot reach $2Ea$. In this study, the stiffness will quickly increase to a maximum within 20 nm to achieve full contact. Therefore, we fitted the linear region with maximum stiffness (S_{linear}, green dash line in Fig. 5.2c) and selected the starting point as the point where the stiffness is greater

than 50% of S_{linear}. This contact point is reset as the zero point of the whole load-depth, as shown in Fig. 5.2d (blue line). After these two steps of corrections, corrected load-depth curves can be used to yield the stress-curve by using appropriate theory.

5.4.2 Corrected indentation properties of NiCo and NiCoFeCr

Fig. 5.3a and 5.3b show the corrected load-depth curves for the five nanoindentations for NiCo and NiCoFeCr sample in six different areas after two steps of corrections. The maximum displacement is fixed so the load at peak displacement reflects the different deformation resistance of materials. Indentation results show considerable sensitivity for detecting radiation-induced hardening though the radiation damage level is relatively low. Compared to the un-irradiated sample, irradiated areas present higher load values at the maximum displacement. The load values increase from ~2500 μN up to ~3800 μN with enhanced radiation damage for NiCo. This feature reflects the dependence of plastic behavior and hardening in materials on the radiation damage levels. Higher levels of radiation damage induce more hardening due to the denser distribution of radiation-induced defects. Some curves show the single discontinuity at shallow depths generally less than 50nm, this behavior should be associated with the uneven roughness of the sample surface.

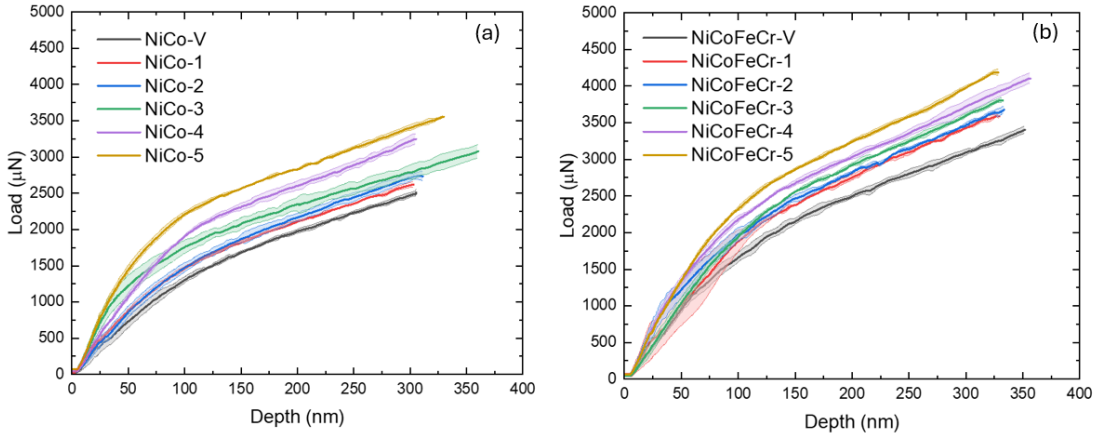

Figure 5.3 Load-depth curves of flat punch indentations on virgin and irradiated regions with 5 different doses for (a) NiCo and (b) NiCoFeCr samples. The shadow areas represent the standard deviations of measurements.

The observations of NiCoFeCr sample are displayed in Fig. 5.3b. Indentation results in all six areas show consistent properties of load-depth curves. Similar to NiCo samples, the load values at maximum depth also present radiation dependence that irradiated areas show higher load at 250nm displacement. The maximum load values upon indentation vary from ~3500 μN up to 4500 μN with the increase of radiation damage and radiation hardening is clearly reflected compared to un-irradiated area. Besides, the intrinsic properties of NiCo and NiCoFeCr alloys can also be compared from un-irradiated areas (Fig. 5.3a and Fig. 5.3b). The NiCoFeCr sample intrinsically has better deformation resistance to indentation owing to its chemical complexity and more severe lattice distortion. However, the effect of irradiation on elastic and plastic deformation behaviors of materials cannot be clearly reflected in load-depth curves.

5.4.3 Acquisition of stress-strain curves

Classical theories, including Sneddon's [267] and Hertzian's [268] methods, provide analytical solution of fully elastic contact between flat punch indentation and sample. However, plasticity cannot be solved directly. Hay [258] developed an empirical solution to obtain the stress-strain with the flat-punch nanoindentation system based on finite element analysis, which is briefly summarized below. The true strain is defined from Sneddon's solution for the elastic indentation with a flat punch [267]:

$$\varepsilon = \left(\frac{2}{\pi}\right) \cdot \left(\frac{h}{a}\right) \tag{5.4}$$

where h is the indentation depth and a is the effective radius of the flat punch indenter, which is of 500nm in this study.

And the true stress is defined by scaling the mean pressure underneath the indentation as:

$$\sigma = \zeta P_m \tag{5.5}$$

where the mean contact pressure P_m can be calculated through $\frac{P}{\pi a^2}$. ζ depends on the degree of plasticity, which is a function of the stiffness S^* defined by:

$$S^* = \frac{S_L}{S} \tag{5.6}$$

where S_L is the instantaneous stiffness, which was obtained as the slope of the curve between the immediate point and the prior point; S is the elastic contact stiffness, which is from unloading. This elastic contact stiffness was computed by fitting 60%-90% of the peak load from unloading curves. Based on finite element simulations with different materials with different work hardening rates, it is discovered that ζ has an empirical relation with S^* as [258]:

$$\zeta = 0.4436 * (S^*)^2 + 0.1202 * S^* + 0.3489 \quad (5.7)$$

As such, the stress can be determined using Eqn. 5. Note that this equation only applies to the plastic region. In the elastic region, ζ should be unity.

5.4.4 Construct stress-strain curves

The method above allows us to obtain the stress-strain curve in the plastic region. We propose to use the region that passes the elastic-plastic transition based on the slope of stiffness-depth curve. As shown in Fig. 5.4a, the stiffness-load curve shows a sharp increase and then decreases till a stable stage is reached. We use the point that has the peak stiffness as the yielding point (purple line). All samples show peak values of stiffness at around 0.02 of strain and become stable at 0.15. Therefore, we use $\sigma_{0.02}$ as the offset yield strength and select data points with the strain range of 0.15 – 0.30 to describe the plastic deformation behavior (as shown in Fig. 5b). Hollmon's constitutive law is used to fit data points [269]:

$$\sigma = k\varepsilon^n \quad (5.8)$$

where k is the strength coefficient, n is the strain hardening exponent. The elastic region uses a straight line with the slope equal to Young's modulus measured from Berkovich nanoindentation.

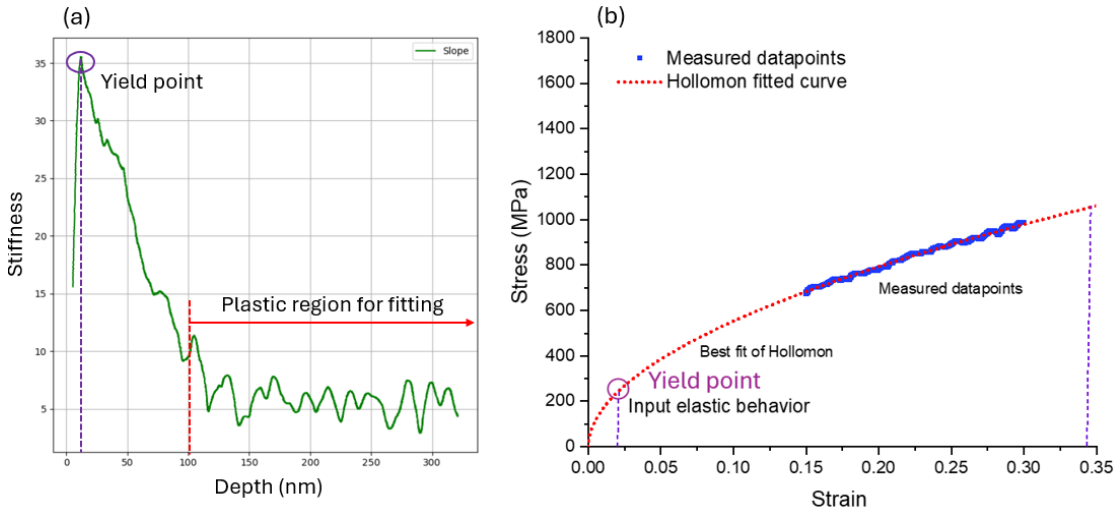

Figure 5.4 (a) an example of stiffness-depth curve in NiCo sample. (b) demonstration of determination of fitted range and yield point based on stiffness criterion.

Fig. 5.5 shows the corresponding stress-strain curves obtained from six different areas of NiCo and NiCoFeCr samples. For NiCo sample, the stress-strain curves show a similar tendency to load-depth curves. Radiation hardening is obvious, which increases with the radiation dose. The maximum strengths of NiCo sample increase with the enhanced radiation dose that increases from ~1000 MPa to ~1400 MPa (40% increase). The NiCoFeCr sample also shows a similar tendency. The maximum strengths increase from ~ 1600 MPa up to ~ 2000 MPa when the radiation dose gradually increases (25% increase). Note that NiCoFeCr samples always exhibit higher strength than NiCo samples for un-irradiated and under the same radiation conditions. Irradiation has a greater effect on hardening NiCo sample than NiCoFeCr sample. This is consistent with reported experimental work in Ni-CSAs, i.e., larger hardening induced by irradiation in NiCoFeCr than in the NiCo sample [97], which will be discussed later.

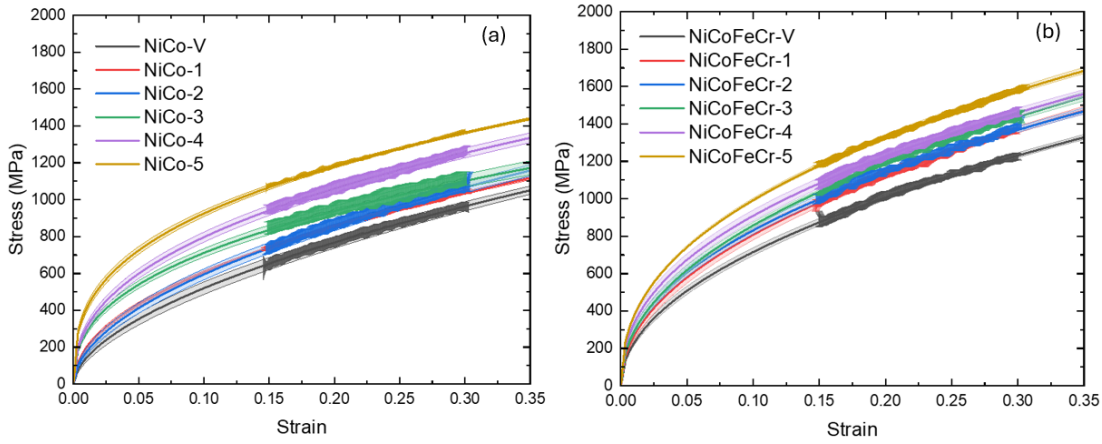

Figure 5.5 Stress-strain curves by flat punch indentation. (a) NiCo and (b) NiCoFeCr. The shadow areas represent the standard deviations of measurements.

5.5 Discussion

5.5.1 Radiation hardening in NiCo and NiCoFeCr

As defined in Fig. 5.4b, the offset value $\sigma_{0.02}$ is used to evaluate the yield strength of sample, as well as radiation hardening. The yield strength of NiCo and NiCoFeCr as the function of radiation dose is summarized in Table 5.1 and demonstrated in Fig. 5.6. The yield strength prior to irradiation is indicated in dash lines in Fig. 5.6 as reference. The yield strengths of unirradiated NiCo and NiCoFeCr samples are 225 MPa and 353 MPa, respectively. The irradiation induces hardening on both NiCo and NiCoFeCr sample but with different extent. For NiCo, irradiation induces a significant increase beyond 0.016 dpa, reaching ~ 570 MPa at 0.3 dpa. In contrast, the radiation hardening in NiCoFeCr is less severe than that in NiCo and there is gradual increase in radiation hardening. It indicates that NiCo and NiCoFeCr samples have different responses to irradiation and NiCoFeCr presents higher resistance to irradiation.

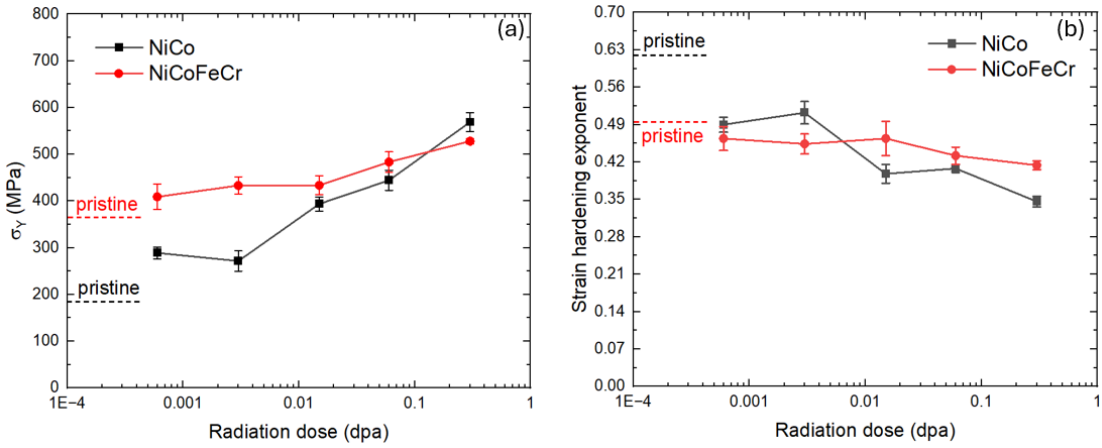

Figure 5.6 The yield strength and strain hardening exponent of NiCo and NiCoFeCr as the function of radiation dose. (a) yield strength. (b) strain hardening exponent.

Table 5.1 Summary of strain hardening exponents and yield strength of NiCo and NiCoFeCr sample in six different areas.

Area	Yield Strength (MPa) NiCo	Yield Strength (MPa) NiCoFeCr	Strain Hardening Exponent (NiCo)	Strain Hardening Exponent (NiCoFeCr)
#V	223.7 ± 22.9	353.5 ± 18.6	0.56 ± 0.03	0.49 ± 0.02
#1	289.2 ± 12.5	409.2 ± 27.2	0.49 ± 0.01	0.46 ± 0.02
#2	278.6 ± 21.5	433.2 ± 18.5	0.51 ± 0.02	0.45 ± 0.02
#3	393.8 ± 12.2	453.7 ± 20.2	0.40 ± 0.02	0.46 ± 0.03
#4	444.5 ± 21.3	483.4 ± 21.9	0.41 ± 0.01	0.43 ± 0.02
#5	569.2 ± 20.0	528.0 ± 5.4	0.35 ± 0.01	0.41 ± 0.01

5.5.2 Radiation-induced change in strain hardening

The deformation behavior can be described by different constitutive equations [269-271]. and as previously mentioned, the classical Hollomon's constitutive equation is used in this study by fitting strain range of 0.15 to 0.30. Table 5.1 summarizes the strain hardening exponent (Fig. 5.6b) of unirradiated and irradiated NiCo and NiCoFeCr samples. Irradiation has reduced strain hardening capability for both NiCo and NiCoFeCr with different amounts. For the NiCo sample, the value of the strain hardening exponent decreases from 0.56 for the un-irradiated area to 0.35 for the #5 irradiated area. This means the irradiation reduces the work hardening capacity of NiCo. In comparison, the values of strain hardening exponent of NiCoFeCr decrease from 0.49 to 0.41 in unirradiated and #5 irradiated area, which do not show the strong dependence of radiation dose. Therefore, the work hardening capability is reduced less in NiCoFeCr than in NiCo.

5.6 Conclusions

The study employed flat punch nanoindentation to probe the surface properties and study elastic-plastic deformation behaviors of ion-irradiated NiCo and NiCoFeCr materials. The near-homogeneous radiation-damaged surfaces are produced by high energy heavy ion irradiation with 5 different damage levels, from ~ 0.0006 dpa up to ~ 0.3 dpa within 500 nm of the surface.

(a) Flat punch nanoindentation with thermal drift correction based on Hay's method is proven to be able to capture strength and strain hardening to evaluate new alloys and radiation damage.

(b) The radiation hardening exists in both NiCo and NiCoFeCr, but NiCoFeCr shows less hardening and less radiation dose dependence. The radiation hardening is more obvious

in the NiCo than in NiCoFeCr: irradiation induces 40% and 25% increase in strength for NiCo and NiCoFeCr up to 0.3 dpa. At 0.3 dpa, the strength increases from 225 MPa to 570 MPa in NiCo, while it increases from 353MPa to 528 MPa.

(c) The strain hardening capability degrades due to irradiation in both NiCo and NiCoFeCr, and the degradation is less severe in NiCoFeCr: the strain hardening exponents of NiCo reduce from 0.56 to 0.35 up to 0.3 dpa while that of NiCoFeCr slightly decrease from 0.49 to 0.41.

5.7 Acknowledgements

L.Y. and Y.C. acknowledge partial financial support by NSF-CMMI 1728554.

CHAPTER 6 : CONCLUSIONS AND FUTURE WORK

6.1 Conclusions

This thesis developed different procedures for nanoindentation, nanoindentation strain rate jump tests, flat-punch nanoindentation and data analysis/correction for exploring un-irradiated and irradiated Ni-based concentrated solid solution alloys (CSAs). Different Ni-based CSAs, including NiCo, NiFe, $Ni_{80}Cr_{20}$, $N_{80}Mn_{20}$, and NiCoFeCr are involved. The major conclusions regarding materials developments are summarized as follows:

(a) The type of alloying elements is more critical than the number of elements in strengthening: Co does not provide strengthening in Ni, while Cr, Mn, and Fe are effective strengthening elements. Cr is the most effective among all the 3d transition metal elements. The alloying in CSAs simultaneously increases the densities of statistically stored dislocations and geometrically necessary dislocations. The hardness of this batch of Ni-based CSAs follows the tendency: $Ni_{80}Cr_{20}$ > $Ni_{80}Mn_{20}$ > NiCoFeCr > NiFe > NiCo. The lattice distortion from atomic-size difference plays a central role in strengthening, including solid solution strengthening and work hardening.

(b) The radiation-induced hardening in CSAs originates from two sources: one is from radiation-induced defects, and another is from the increase in geometrically necessary dislocations. But two strengthening components show different hardening effects on different concentrated solid solution alloys. The radiation-induced defects induce obvious hardening effects in NiFe and NiCoFeCr while these defects do not show positive hardening effect in NiCo. Meantime, the irradiation introduces higher density of geometrically necessary dislocations in NiCo and NiFe, but not in NiCoFeCr. The density

change of geometrically necessary dislocations is interpreted by the volume change of plastic zone that accommodates the distribution of geometrically necessary dislocations. The volume of this plastic zone is relatively smaller in irradiated NiCo and NiFe while there is almost no change in NiCoFeCr.

(c) Flat punch indentation is successfully utilized to obtain the stress-strain curves of both NiCo and NiCoFeCr to study the deformation behavior and radiation response. A complete methodology is developed to better yield the accurate stress-strain curves from flat punch indentation by considering the effect of thermal drift and contact issue. Thermal drift is proven to have a big impact on the acquisition of indentation data and needs to be corrected. From the results, NiCoFeCr sample shows better resistance to degradation of strain hardening capacity during irradiation than NiCo. The strain hardening exponents of NiCo reduce from 0.56 to 0.35 up to 0.3 dpa while that of NiCoFeCr slightly decrease from 0.49 to 0.41. At the same time, the radiation hardening exists in both NiCo and NiCoFeCr, but NiCoFeCr shows less hardening and less radiation dose dependence.

6.2 Future work

This thesis work covers the exploration of mechanical properties and radiation damage in Ni-based CSAs containing different *3d* transition metal elements including binary NiCo, NiFe, $Ni_{80}Cr_{20}$, $Ni_{80}Mn_{20}$ and quaternary NiCoFeCr. The work presented in this thesis investigates the strengthening mechanisms upon deformation and uncovers the potential radiation resistance of Ni-based CSAs. However, the irradiation damage in this study is still at a relatively low-dose level and the experimental work also only focuses on the initial stage of irradiation. This is not

sufficient to confirm the radiation resistance of Ni-based concentrated solid solution alloys as the structural materials for high-demanding nuclear reactors, which typically require the operation at elevated temperature and extremely high radiation dose. In this case, future work is needed to further study the irradiation tolerance of Ni-based concentrated solid solution alloys at high temperature and high-dose irradiation. First, high-temperature nanoindentations are needed to investigate the mechanical performance of Ni-based concentrated solid solution alloys at elevated temperatures. Second, radiation damage should be subject to a relatively high dose like ~100 dpa. In-situ irradiation experiments especially in-situ TEM is the promising tool to observe the defect evolutions during irradiation, which benefits for the examination of defect migration kinetics. For methodology of nanoindentation developed in thesis, further work can be conducted to validate developed models of nanoindentation by more in-depth microstructural analysis. In addition, research work can also expand to use various indenter tips to evaluate the surface deformation under different stress states such as spherical indentation. Finally, the real time of dislocation behaviors upon deformation can be studied by in-situ nanoindentation.

SUPPLEMENTARY MATERIALS

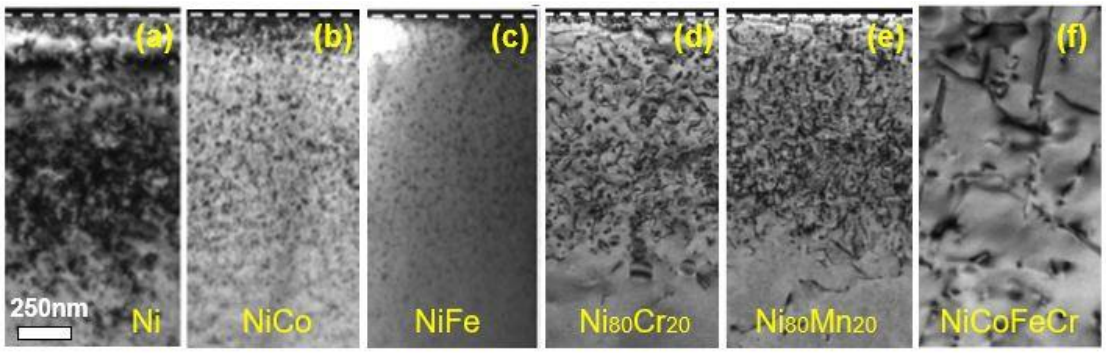

Figure S1. Bright-field TEM micrographs of heavy-ion irradiated Ni-based CSAs confirming the single-crystal structure. The defects in the samples in terms of dislocation lines and loops were induced by irradiation: (a) Ni (b) NiCo (c) NiFe (d) $Ni_{80}Cr_{20}$ (e) $Ni_{80}Mn_{20}$ (f) NiCoFeCr.

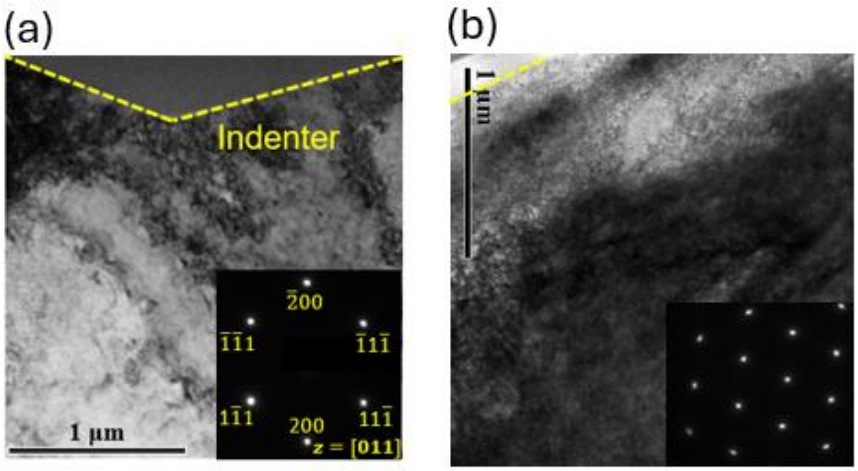

Figure S2. Bright-field TEM micrographs of ion irradiated Ni-based CSAs confirming the single-crystal structure and being indented on (100) plane. (a) NiCo (b) NiCoFeCr.

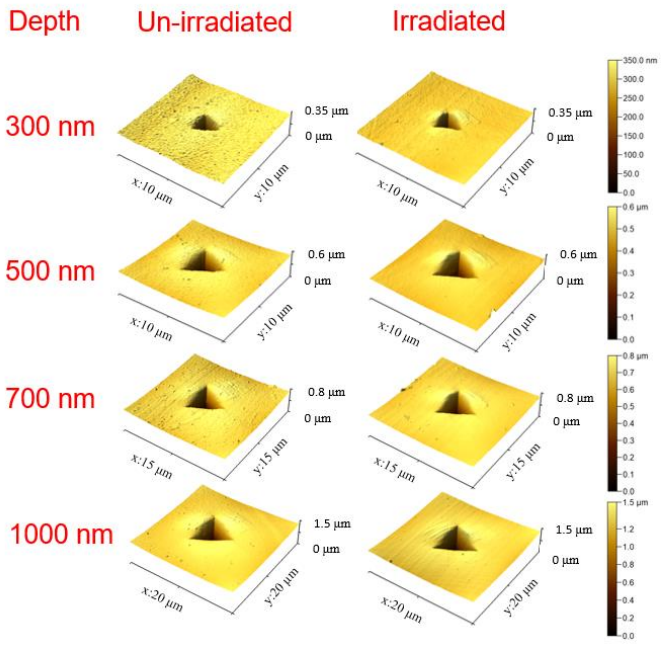

Figure S3. A complete AFM topographical examination of NiCoFeCr at various penetration depths before and after irradiation.

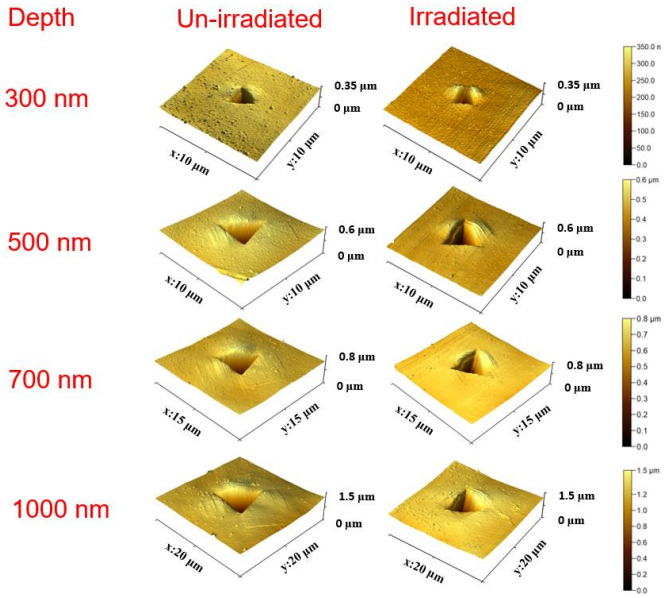

Figure S4. A complete AFM topographical examination of NiFe at various penetration depths before and after irradiation.

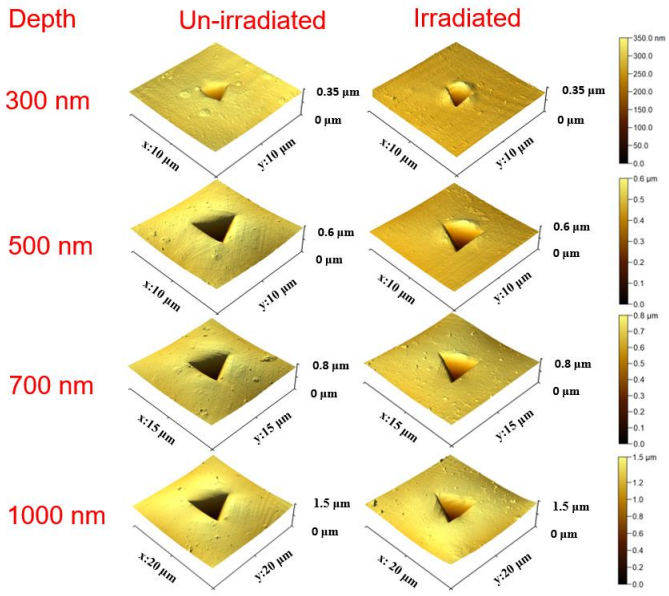

Figure S5. A complete AFM topographical examination of NiCo at various penetration depths before and after irradiation

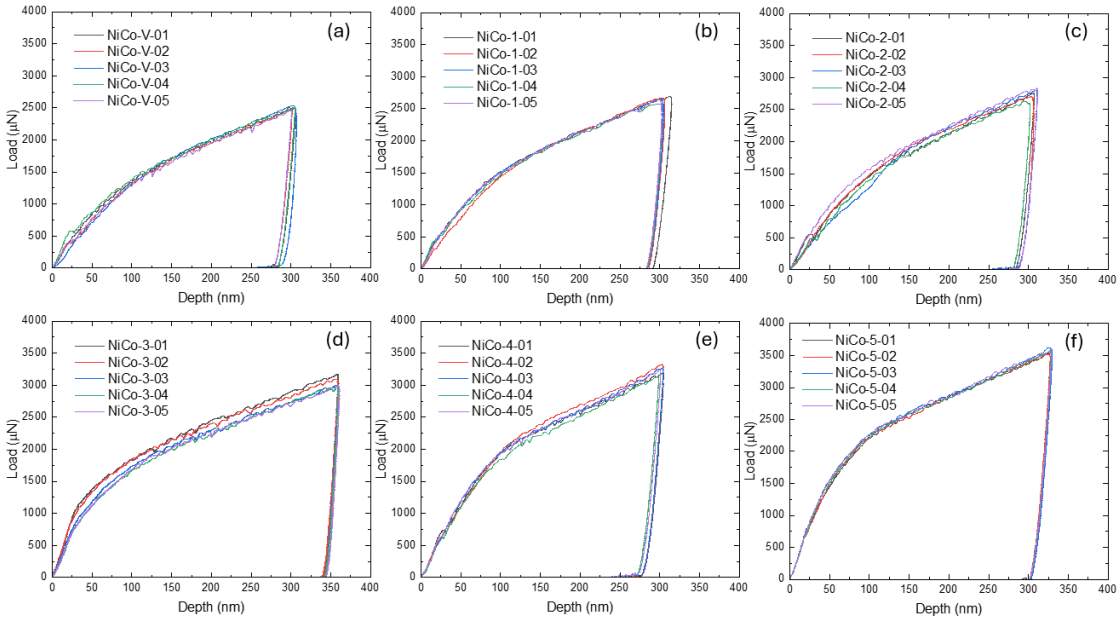

Figure S6. Corrected load-depth curves for NiCo in six different areas.

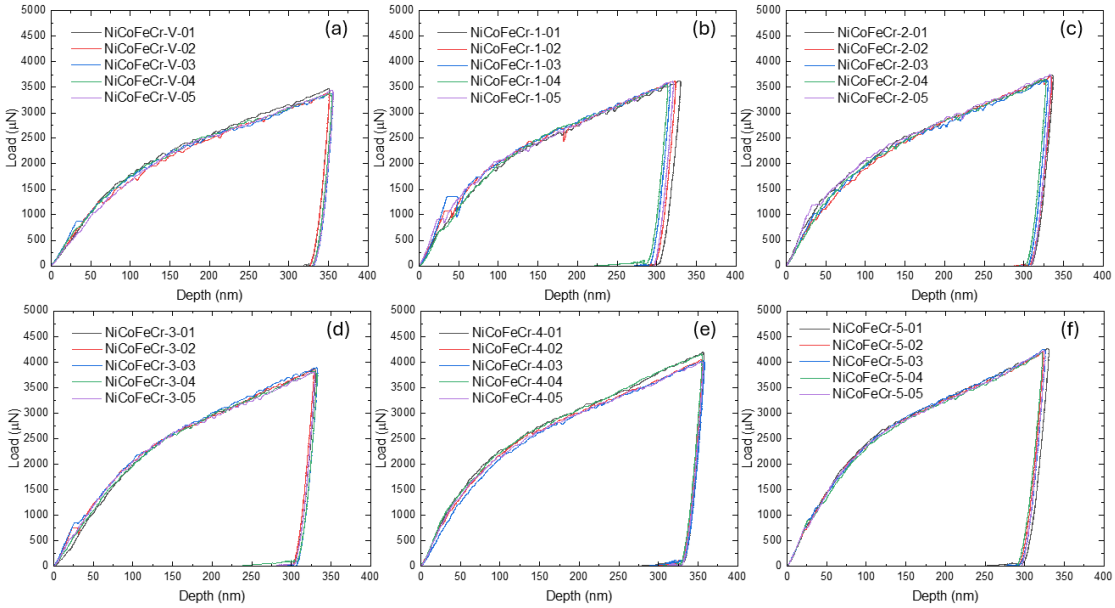

Figure S7. Corrected load-depth curves for NiCoFeCr in six different areas.

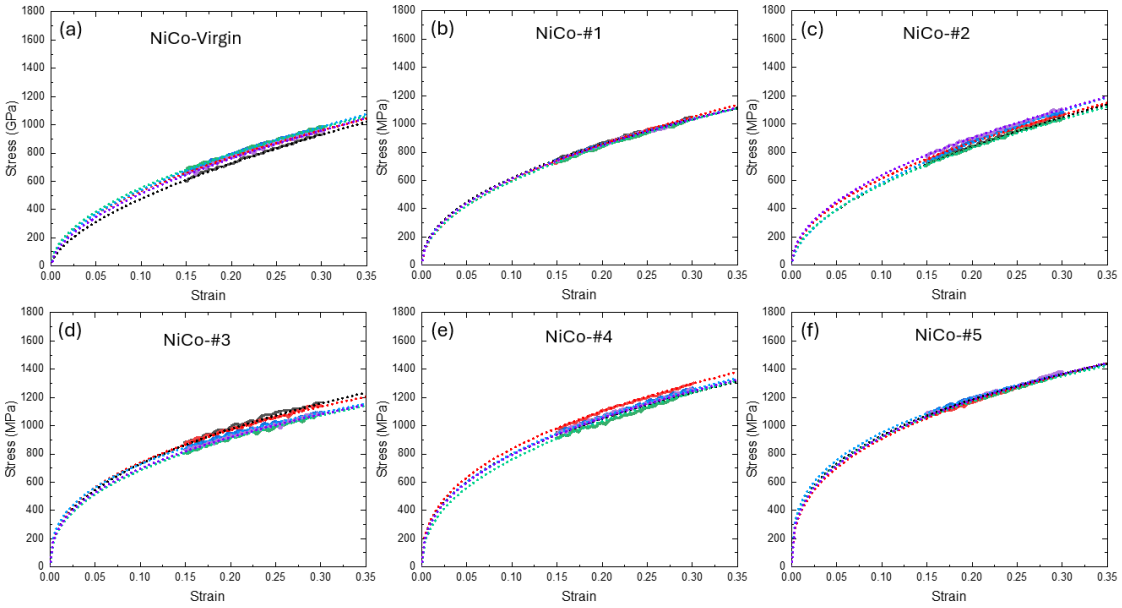

Figure S8. Indentation stress-strain curves of NiCo in six different areas.

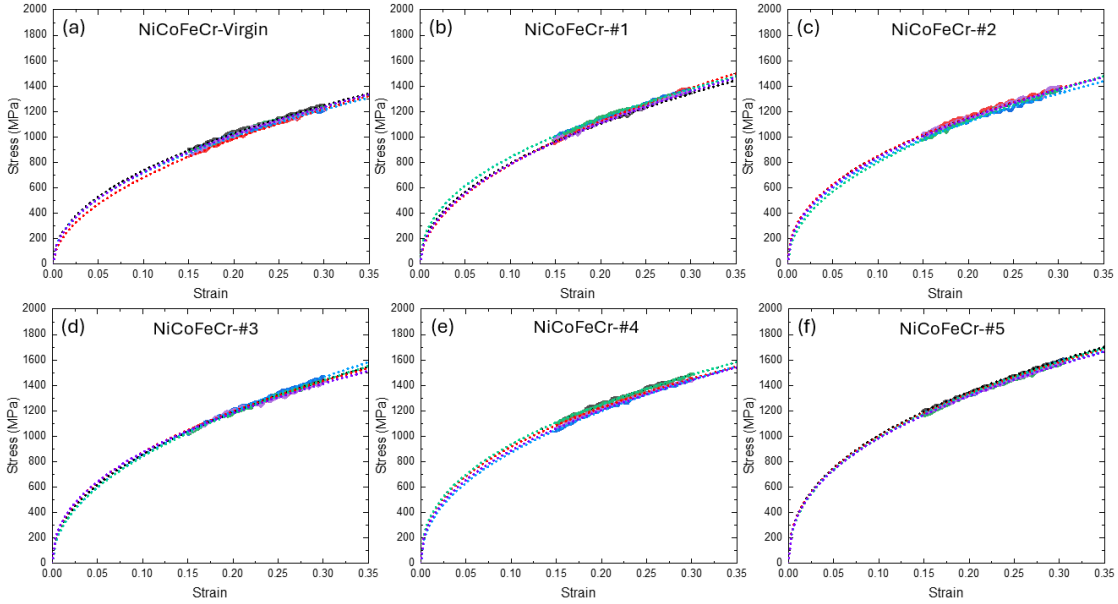

Figure S9. Indentation stress-strain curves of NiCoFeCr in six different areas.

REFERENCES

[1] George, E.P., W.A. Curtin, and C.C. Tasan, *High entropy alloys: A focused review of mechanical properties and deformation mechanisms*. Acta Materialia, 2020. **188**: p. 435-474.

[2] Li, W., et al., *Mechanical behavior of high-entropy alloys*. Progress in Materials Science, 2021. **118**: p. 100777.

[3] Senkov, O.N., et al., *Development and exploration of refractory high entropy alloys—A review*. Journal of materials research, 2018. **33**(19): p. 3092-3128.

[4] Jien-Wei, Y., *Recent progress in high entropy alloys*. Ann. Chim. Sci. Mat, 2006. **31**(6): p. 633-648.

[5] Cao, B., et al., *Cocktail effects in understanding the stability and properties of face-centered-cubic high-entropy alloys at ambient and cryogenic temperatures*. Scripta materialia, 2020. **187**: p. 250-255.

[6] Ye, Y., et al., *Design of high entropy alloys: A single-parameter thermodynamic rule*. Scripta Materialia, 2015. **104**: p. 53-55.

[7] Haase, C., et al., *Combining thermodynamic modeling and 3D printing of elemental powder blends for high-throughput investigation of high-entropy alloys–Towards rapid alloy screening and design*. Materials Science and Engineering: A, 2017. **688**: p. 180-189.

[8] Schuh, B., et al., *Thermodynamic instability of a nanocrystalline, single-phase TiZrNbHfTa alloy and its impact on the mechanical properties*. Acta Materialia, 2018. **142**: p. 201-212.

[9] Porter, D.A. and K.E. Easterling, *Phase transformations in metals and alloys (revised reprint)*. 2009: CRC press.

[10] Zhang, Y., et al., *Microstructures and properties of high-entropy alloys*. Progress in materials science, 2014. **61**: p. 1-93.

[11] Yeh, J.-W., *Physical metallurgy of high-entropy alloys*. Jom, 2015. **67**(10): p. 2254-2261.

[12] Tong, Y., et al., *Local lattice distortion in NiCoCr, FeCoNiCr and FeCoNiCrMn concentrated alloys investigated by synchrotron X-ray diffraction*. Materials & Design, 2018. **155**: p. 1-7.

[13] Oh, H.S., et al., *Lattice distortions in the FeCoNiCrMn high entropy alloy studied by theory and experiment*. Entropy, 2016. **18**(9): p. 321.

[14] Wang, Z., et al., *Effect of lattice distortion on solid solution strengthening of BCC high-entropy alloys*. Journal of Materials Science & Technology, 2018. **34**(2): p. 349-354.

[15] Guo, W., et al., *Local Atomic Structure of a High-Entropy Alloy: An X-Ray and Neutron Scattering Study*. Metallurgical and Materials Transactions A, 2013. **44**(5): p. 1994-1997.

[16] Zhang, Y., et al., *Solid-Solution Phase Formation Rules for Multi-component Alloys*. Advanced Engineering Materials, 2008. **10**(6): p. 534-538.

[17] Tsai, K.Y., M.H. Tsai, and J.W. Yeh, *Sluggish diffusion in Co–Cr–Fe–Mn–Ni high-entropy alloys*. Acta Materialia, 2013. **61**(13): p. 4887-4897.
[18] Gao, M.C., et al., *High-entropy alloys: fundamentals and applications*. 2016: Springer.
[19] Chen, W. and L. Zhang, *High-throughput determination of interdiffusion coefficients for Co-Cr-Fe-Mn-Ni high-entropy alloys*. Journal of Phase Equilibria and Diffusion, 2017. **38**: p. 457-465.
[20] Kühn, U., et al., *As-cast quasicrystalline phase in a Zr-based multicomponent bulk alloy*. Applied Physics Letters, 2000. **77**(20): p. 3176-3178.
[21] Eißmann, N., et al., *High-entropy alloy CoCrFeMnNi produced by powder metallurgy*. Powder Metallurgy, 2017. **60**(3): p. 184-197.
[22] Jin, K., et al., *Influence of compositional complexity on interdiffusion in Ni-containing concentrated solid-solution alloys*. Materials Research Letters, 2018. **6**(5): p. 293-299.
[23] Cheng, C.-Y., et al., *Physical metallurgy of concentrated solid solutions from low-entropy to high-entropy alloys*. Current Opinion in Solid State and Materials Science, 2017. **21**(6): p. 299-311.
[24] Gali, A. and E.P. George, *Tensile properties of high-and medium-entropy alloys*. Intermetallics, 2013. **39**: p. 74-78.
[25] Otto, F., et al., *The influences of temperature and microstructure on the tensile properties of a CoCrFeMnNi high-entropy alloy*. Acta Materialia, 2013. **61**(15): p. 5743-5755.
[26] Laplanche, G., et al., *Microstructure evolution and critical stress for twinning in the CrMnFeCoNi high-entropy alloy*. Acta Materialia, 2016. **118**: p. 152-163.
[27] Okamoto, N.L., et al., *Size effect, critical resolved shear stress, stacking fault energy, and solid solution strengthening in the CrMnFeCoNi high-entropy alloy*. Scientific reports, 2016. **6**(1): p. 35863.
[28] Li, Z., et al., *Metastable high-entropy dual-phase alloys overcome the strength–ductility trade-off*. Nature, 2016. **534**(7606): p. 227-230.
[29] Laplanche, G., et al., *Reasons for the superior mechanical properties of medium-entropy CrCoNi compared to high-entropy CrMnFeCoNi*. Acta Materialia, 2017. **128**: p. 292-303.
[30] Jo, Y.H., et al., *Analysis of damage-tolerance of TRIP-assisted V10Cr10Fe45Co30Ni5 high-entropy alloy at room and cryogenic temperatures*. Journal of Alloys and Compounds, 2020. **844**: p. 156090.
[31] Gludovatz, B., et al., *A fracture-resistant high-entropy alloy for cryogenic applications*. Science, 2014. **345**(6201): p. 1153-1158.
[32] Yang, T., et al., *Multicomponent intermetallic nanoparticles and superb mechanical behaviors of complex alloys*. Science, 2018. **362**(6417): p. 933-937.
[33] Li, W., P.K. Liaw, and Y. Gao, *Fracture resistance of high entropy alloys: A review*. Intermetallics, 2018. **99**: p. 69-83.
[34] Xu, X., et al., *Transmission electron microscopy characterization of dislocation structure in a face-centered cubic high-entropy alloy Al0. 1CoCrFeNi*. Acta Materialia, 2018. **144**: p. 107-115.

[35] Yoshida, S., et al., *Effect of elemental combination on friction stress and Hall-Petch relationship in face-centered cubic high/medium entropy alloys*. Acta Materialia, 2019. **171**: p. 201-215.
[36] Dirras, G., et al., *Microstructural investigation of plastically deformed Ti20Zr20Hf20Nb20Ta20 high entropy alloy by X-ray diffraction and transmission electron microscopy*. Materials Characterization, 2015. **108**: p. 1-7.
[37] Rao, S., et al., *Atomistic simulations of dislocations in a model BCC multicomponent concentrated solid solution alloy*. Acta Materialia, 2017. **125**: p. 311-320.
[38] Kim, J.H., et al., *Mechanical properties and deformation twinning behavior of as-cast CoCrFeMnNi high-entropy alloy at low and high temperatures*. Materials Science and Engineering: A, 2018. **712**: p. 108-113.
[39] Gutierrez-Urrutia, I., S. Zaefferer, and D. Raabe, *The effect of grain size and grain orientation on deformation twinning in a Fe–22 wt.% Mn–0.6 wt.% C TWIP steel*. Materials Science and Engineering: A, 2010. **527**(15): p. 3552-3560.
[40] Naeita, N. and J. Takamura, *Deformation twinning in silver-and copper-alloy crystals*. Philosophical magazine, 1974. **29**(5): p. 1001-1028.
[41] Liu, S., et al., *Transformation-reinforced high-entropy alloys with superior mechanical properties via tailoring stacking fault energy*. Journal of Alloys and Compounds, 2019. **792**: p. 444-455.
[42] Deng, Y., et al., *Design of a twinning-induced plasticity high entropy alloy*. Acta Materialia, 2015. **94**: p. 124-133.
[43] Li, Z., et al., *Ab initio assisted design of quinary dual-phase high-entropy alloys with transformation-induced plasticity*. Acta Materialia, 2017. **136**: p. 262-270.
[44] Eguchi, T., et al., *Fatigue crack growth behavior and associated microstructure in a metastable high-entropy alloy*. Procedia Structural Integrity, 2018. **13**: p. 831-836.
[45] Liu, K., et al., *Metastability-assisted fatigue behavior in a friction stir processed dual-phase high entropy alloy*. Materials Research Letters, 2018. **6**(11): p. 613-619.
[46] Basu, S., et al., *Strain rate sensitivity of a TRIP-assisted dual-phase high-entropy alloy*. Frontiers in Materials, 2018. **5**: p. 30.
[47] Huang, H., et al., *Phase-transformation ductilization of brittle high-entropy alloys via metastability engineering*. Advanced Materials, 2017. **29**(30): p. 1701678.
[48] Li, Z., et al., *A TRIP-assisted dual-phase high-entropy alloy: grain size and phase fraction effects on deformation behavior*. Acta Materialia, 2017. **131**: p. 323-335.
[49] Nene, S.S., et al., *Enhanced strength and ductility in a friction stir processing engineered dual phase high entropy alloy*. Scientific reports, 2017. **7**(1): p. 16167.
[50] Wang, M., Z. Li, and D. Raabe, *In-situ SEM observation of phase transformation and twinning mechanisms in an interstitial high-entropy alloy*. Acta Materialia, 2018. **147**: p. 236-246.
[51] Su, J., D. Raabe, and Z. Li, *Hierarchical microstructure design to tune the mechanical behavior of an interstitial TRIP-TWIP high-entropy alloy*. Acta Materialia, 2019. **163**: p. 40-54.

[52] Herrera, C., D. Ponge, and D. Raabe, *Design of a novel Mn-based 1 GPa duplex stainless TRIP steel with 60% ductility by a reduction of austenite stability*. Acta Materialia, 2011. **59**(11): p. 4653-4664.
[53] Fu, S., et al., *Deformation mechanisms and work-hardening behavior of transformation-induced plasticity high entropy alloys by in-situ neutron diffraction*. Materials Research Letters, 2018. **6**(11): p. 620-626.
[54] Li, Z., et al., *Interstitial atoms enable joint twinning and transformation induced plasticity in strong and ductile high-entropy alloys*. Scientific reports, 2017. **7**(1): p. 40704.
[55] Xu, X., et al., *Nanoscale phase separation in a fcc-based CoCrCuFeNiAl0. 5 high-entropy alloy*. Acta Materialia, 2015. **84**: p. 145-152.
[56] Fantin, A., et al., *Short-range chemical order and local lattice distortion in a compositionally complex alloy*. Acta Materialia, 2020. **193**: p. 329-337.
[57] Niu, C., et al., *Spin-driven ordering of Cr in the equiatomic high entropy alloy NiFeCrCo*. Applied Physics Letters, 2015. **106**(16).
[58] Körmann, F., A.V. Ruban, and M.H. Sluiter, *Long-ranged interactions in bcc NbMoTaW high-entropy alloys*. Materials Research Letters, 2017. **5**(1): p. 35-40.
[59] Zhao, Y., et al., *A simplified model connecting lattice distortion with friction stress of Nb-based equiatomic high-entropy alloys*. Materials Research Letters, 2019. **7**(8): p. 340-346.
[60] Nabarro, F., *Dislocations in a simple cubic lattice*. Proceedings of the Physical Society, 1947. **59**(2): p. 256.
[61] Toda-Caraballo, I. and P.E. Rivera-Díaz-del-Castillo, *Modelling solid solution hardening in high entropy alloys*. Acta Materialia, 2015. **85**: p. 14-23.
[62] Fleischer, R.L., *Substitutional solution hardening*. Acta metallurgica, 1963. **11**(3): p. 203-209.
[63] Juan, C.-C., et al., *Solution strengthening of ductile refractory HfMoxNbTaTiZr high-entropy alloys*. Materials Letters, 2016. **175**: p. 284-287.
[64] Wu, Y., et al., *Phase composition and solid solution strengthening effect in TiZrNbMoV high-entropy alloys*. Materials & Design, 2015. **83**: p. 651-660.
[65] Lin, C.-M., et al., *Effect of Al addition on mechanical properties and microstructure of refractory AlxHfNbTaTiZr alloys*. Journal of Alloys and Compounds, 2015. **624**: p. 100-107.
[66] Labusch, R., *A statistical theory of solid solution hardening*. physica status solidi (b), 1970. **41**(2): p. 659-669.
[67] Wu, Z., Y. Gao, and H. Bei, *Thermal activation mechanisms and Labusch-type strengthening analysis for a family of high-entropy and equiatomic solid-solution alloys*. Acta Materialia, 2016. **120**: p. 108-119.
[68] Varvenne, C., A. Luque, and W.A. Curtin, *Theory of strengthening in fcc high entropy alloys*. Acta Materialia, 2016. **118**: p. 164-176.
[69] Maier, V., et al., *Nanoindentation strain-rate jump tests for determining the local strain-rate sensitivity in nanocrystalline Ni and ultrafine-grained Al*. Journal of materials research, 2011. **26**(11): p. 1421-1430.

[70] Ashby, M., *The deformation of plastically non-homogeneous materials*. The Philosophical Magazine: A Journal of Theoretical Experimental and Applied Physics, 1970. **21**(170): p. 399-424.
[71] Hall, E., *The deformation and ageing of mild steel: III discussion of results*. Proceedings of the Physical Society. Section B, 1951. **64**(9): p. 747.
[72] Petch, N.J., *The cleavage strength of polycrystals*. J. Iron Steel Inst., 1953. **174**: p. 25-28.
[73] Beladi, H., et al., *Orientation dependence of twinning and strain hardening behaviour of a high manganese twinning induced plasticity steel with polycrystalline structure*. Acta materialia, 2011. **59**(20): p. 7787-7799.
[74] Gutiérrez-Urrutia, I. and D. Raabe, *Multistage strain hardening through dislocation substructure and twinning in a high strength and ductile weight-reduced Fe–Mn–Al–C steel*. Acta Materialia, 2012. **60**(16): p. 5791-5802.
[75] Karaman, I., et al., *Modeling the deformation behavior of Hadfield steel single and polycrystals due to twinning and slip*. Acta Materialia, 2000. **48**(9): p. 2031-2047.
[76] Bouaziz, O. and N. Guelton, *Modelling of TWIP effect on work-hardening*. Materials Science and Engineering: A, 2001. **319**: p. 246-249.
[77] Slone, C., et al., *Influence of deformation induced nanoscale twinning and FCC-HCP transformation on hardening and texture development in medium-entropy CrCoNi alloy*. Acta Materialia, 2018. **158**: p. 38-52.
[78] Shun, T.-T. and Y.-C. Du, *Age hardening of the Al0. 3CoCrFeNiC0. 1 high entropy alloy*. Journal of alloys and compounds, 2009. **478**(1-2): p. 269-272.
[79] Liu, W., et al., *Ductile CoCrFeNiMox high entropy alloys strengthened by hard intermetallic phases*. Acta Materialia, 2016. **116**: p. 332-342.
[80] Ming, K., X. Bi, and J. Wang, *Precipitation strengthening of ductile Cr15Fe20Co35Ni20Mo10 alloys*. Scripta Materialia, 2017. **137**: p. 88-93.
[81] He, J., et al., *Precipitation behavior and its effects on tensile properties of FeCoNiCr high-entropy alloys*. Intermetallics, 2016. **79**: p. 41-52.
[82] He, J., et al., *A precipitation-hardened high-entropy alloy with outstanding tensile properties*. Acta Materialia, 2016. **102**: p. 187-196.
[83] Argon, A.S., *Physics of strength and plasticity*. 1969.
[84] Was, G.S., *Fundamentals of radiation materials science: metals and alloys*. Vol. 510. 2007: Springer.
[85] Zhang, Y., Y.N. Osetsky, and W.J. Weber, *Tunable chemical disorder in concentrated alloys: defect physics and radiation performance*. Chemical Reviews, 2021. **122**(1): p. 789-829.
[86] Zhang, Z., D.E. Armstrong, and P.S. Grant, *The effects of irradiation on CrMnFeCoNi high-entropy alloy and its derivatives*. Progress in Materials Science, 2022. **123**: p. 100807.
[87] Jin, K. and H. Bei, *Single-phase concentrated solid-solution alloys: Bridging intrinsic transport properties and irradiation resistance*. Frontiers in materials, 2018. **5**: p. 26.
[88] Zhang, Y., et al., *Influence of chemical disorder on energy dissipation and defect evolution in concentrated solid solution alloys*. Nature communications, 2015. **6**(1): p. 8736.

[89] Lu, C., et al., *Enhancing radiation tolerance by controlling defect mobility and migration pathways in multicomponent single-phase alloys*. Nature communications, 2016. **7**(1): p. 13564.
[90] Yang, T., et al., *Irradiation responses and defect behavior of single-phase concentrated solid solution alloys*. Journal of Materials Research, 2018. **33**(19): p. 3077-3091.
[91] Koppenaal, T., W. Yeh, and R. Cotterill, *Lattice defects in neutron irradiated αCu solid solution alloys*. Philosophical Magazine, 1966. **13**(124): p. 867-871.
[92] Zhao, S., et al., *Frenkel defect recombination in Ni and Ni–containing concentrated solid–solution alloys*. Acta Materialia, 2019. **173**: p. 184-194.
[93] Zhang, Y., et al., *Influence of chemical disorder on energy dissipation and defect evolution in advanced alloys*. Journal of Materials Research, 2016. **31**(16): p. 2363-2375.
[94] Granberg, F., et al., *Mechanism of radiation damage reduction in equiatomic multicomponent single phase alloys*. Physical review letters, 2016. **116**(13): p. 135504.
[95] Granberg, F., et al., *Damage buildup and edge dislocation mobility in equiatomic multicomponent alloys*. Nuclear Instruments and Methods in Physics Research Section B: Beam Interactions with Materials and Atoms, 2017. **393**: p. 114-117.
[96] Lu, C., et al., *Direct observation of defect range and evolution in ion-irradiated single crystalline Ni and Ni binary alloys*. Scientific reports, 2016. **6**(1): p. 19994.
[97] Jin, K., et al., *Effects of compositional complexity on the ion-irradiation induced swelling and hardening in Ni-containing equiatomic alloys*. Scripta Materialia, 2016. **119**: p. 65-70.
[98] Abhaya, S., et al., *Effect of dose and post irradiation annealing in Ni implanted high entropy alloy FeCrCoNi using slow positron beam*. Journal of alloys and compounds, 2016. **669**: p. 117-122.
[99] Xia, S., et al., *Phase stability and microstructures of high entropy alloys ion irradiated to high doses*. Journal of Nuclear Materials, 2016. **480**: p. 100-108.
[100] He, M.-R., et al., *Mechanisms of radiation-induced segregation in CrFeCoNi-based single-phase concentrated solid solution alloys*. Acta Materialia, 2017. **126**: p. 182-193.
[101] Kumar, N.K., et al., *Microstructural stability and mechanical behavior of FeNiMnCr high entropy alloy under ion irradiation*. Acta Materialia, 2016. **113**: p. 230-244.
[102] Chen, Y., et al., *Microstructure and strengthening mechanisms in Cu/Fe multilayers*. Acta Materialia, 2012. **60**(18): p. 6312-6321.
[103] Pharr, G. and W. Oliver, *Measurement of thin film mechanical properties using nanoindentation*. Mrs Bulletin, 1992. **17**(7): p. 28-33.
[104] Saha, R. and W.D. Nix, *Effects of the substrate on the determination of thin film mechanical properties by nanoindentation*. Acta materialia, 2002. **50**(1): p. 23-38.
[105] Jin, K., et al., *Quantifying early stage irradiation damage from nanoindentation pop-in tests*. Scripta Materialia, 2018. **157**: p. 49-53.
[106] Hosemann, P., et al., *Issues to consider using nano indentation on shallow ion beam irradiated materials*. Journal of Nuclear Materials, 2012. **425**(1-3): p. 136-139.

[107] Zhang, X., et al., *Radiation damage in nanostructured materials*. Progress in Materials Science, 2018. **96**: p. 217-321.
[108] Chen, Y., et al., *Unusual size-dependent strengthening mechanisms in helium ion-irradiated immiscible coherent Cu/Co nanolayers*. Acta Materialia, 2015. **84**: p. 393-404.
[109] Lucca, D., K. Herrmann, and M. Klopfstein, *Nanoindentation: Measuring methods and applications*. CIRP annals, 2010. **59**(2): p. 803-819.
[110] Schuh, C.A., *Nanoindentation studies of materials*. Materials today, 2006. **9**(5): p. 32-40.
[111] Li, X. and B. Bhushan, *A review of nanoindentation continuous stiffness measurement technique and its applications*. Materials characterization, 2002. **48**(1): p. 11-36.
[112] Walker, A., P. Carrez, and P. Cordier, *Atomic-scale models of dislocation cores in minerals: progress and prospects*. Mineralogical Magazine, 2010. **74**(3): p. 381-413.
[113] McNally, P.J., *3D imaging of crystal defects*. Nature, 2013. **496**(7443): p. 37-38.
[114] Dimiduk, D., M. Uchic, and T. Parthasarathy, *Size-affected single-slip behavior of pure nickel microcrystals*. Acta materialia, 2005. **53**(15): p. 4065-4077.
[115] Iqbal, F., et al., *In situ micro-cantilever tests to study fracture properties of NiAl single crystals*. Acta Materialia, 2012. **60**(3): p. 1193-1200.
[116] Shan, Z., et al., *Mechanical annealing and source-limited deformation in submicrometre-diameter Ni crystals*. Nature materials, 2008. **7**(2): p. 115-119.
[117] Wheeler, J. and J. Michler, *Elevated temperature, nano-mechanical testing in situ in the scanning electron microscope*. Review of Scientific Instruments, 2013. **84**(4).
[118] Nili, H., et al., *In situ nanoindentation: Probing nanoscale multifunctionality*. Progress in Materials Science, 2013. **58**(1): p. 1-29.
[119] Zou, Y., *Nanomechanical studies of high-entropy alloys*. Journal of Materials Research, 2018. **33**(19): p. 3035-3054.
[120] Jin, G., et al., *High temperature wear performance of laser-cladded FeNiCoAlCu high-entropy alloy coating*. Applied Surface Science, 2018. **445**: p. 113-122.
[121] Lee, D.-H., et al., *Spherical nanoindentation creep behavior of nanocrystalline and coarse-grained CoCrFeMnNi high-entropy alloys*. Acta Materialia, 2016. **109**: p. 314-322.
[122] Tsai, M., et al., *Creep of face-centered-cubic {111} and {100} grains in FeCoNiCrMn and FeCoNiCrMnAl alloys: Orientation and solid solution effects*. Intermetallics, 2018. **103**: p. 88-96.
[123] Tabor, D., *The hardness of metals*. 2000: Oxford university press.
[124] Bhushan, B., *Handbook of micro/nano tribology*. Micro/Nanotribology and Micro/Nanomechanics of Magnetic Storage Devices and MEMS, 1995: p. 443-503.
[125] Golovin, Y.I., *Nanoindentation and mechanical properties of materials at submicro- and nanoscale levels: Recent results and achievements*. Physics of the Solid State, 2021. **63**: p. 1-41.
[126] Pharr, G.M., *Recent advances in small-scale mechanical property measurement by nanoindentation*. Current Opinion in Solid State and Materials Science, 2015. **19**(6): p. 315-316.

[127] Wheeler, J., et al., *High temperature nanoindentation: The state of the art and future challenges*. Current Opinion in Solid State and Materials Science, 2015. **19**(6): p. 354-366.
[128] Phani, P.S., et al., *High strain rate nanoindentation testing: Recent advancements, challenges and opportunities*. Current Opinion in Solid State and Materials Science, 2023. **27**(1): p. 101054.
[129] Rabe, R., et al., *Observation of fracture and plastic deformation during indentation and scratching inside the scanning electron microscope*. Thin Solid Films, 2004. **469**: p. 206-213.
[130] Moser, B., et al., *Observation of instabilities during plastic deformation by in-situ SEM indentation experiments*. Advanced Engineering Materials, 2005. **7**(5): p. 388-392.
[131] Moser, B., J.F. Löffler, and J. Michler, *Discrete deformation in amorphous metals: an in situ SEM indentation study*. Philosophical Magazine, 2006. **86**(33-35): p. 5715-5728.
[132] Pathak, S. and S.R. Kalidindi, *Spherical nanoindentation stress–strain curves*. Materials science and engineering: R: Reports, 2015. **91**: p. 1-36.
[133] Gale, J. and A. Achuthan, *The effect of work-hardening and pile-up on nanoindentation measurements*. Journal of materials science, 2014. **49**: p. 5066-5075.
[134] McElhaney, K., J.J. Vlassak, and W.D. Nix, *Determination of indenter tip geometry and indentation contact area for depth-sensing indentation experiments*. Journal of Materials research, 1998. **13**(5): p. 1300-1306.
[135] Pharr, G.M., E.G. Herbert, and Y. Gao, *The indentation size effect: a critical examination of experimental observations and mechanistic interpretations*. Annual Review of Materials Research, 2010. **40**: p. 271-292.
[136] Nix, W.D. and H. Gao, *Indentation size effects in crystalline materials: a law for strain gradient plasticity*. Journal of the Mechanics and Physics of Solids, 1998. **46**(3): p. 411-425.
[137] Ma, Q. and D.R. Clarke, *Size dependent hardness of silver single crystals*. Journal of Materials research, 1995. **10**(4): p. 853-863.
[138] Swadener, J., E. George, and G. Pharr, *The correlation of the indentation size effect measured with indenters of various shapes*. Journal of the Mechanics and Physics of Solids, 2002. **50**(4): p. 681-694.
[139] Jiang, W.-G., J.-J. Su, and X.-Q. Feng, *Effect of surface roughness on nanoindentation test of thin films*. Engineering Fracture Mechanics, 2008. **75**(17): p. 4965-4972.
[140] Demiral, M., *Enhanced gradient crystal-plasticity study of size effects in bcc metal*. 2012, Loughborough University.
[141] Lee, W.-S., et al., *Load effects on nanoindentation behaviour and microstructural evolution of single-crystal silicon*. Materials transactions, 2010. **51**(7): p. 1173-1177.
[142] Wang, Z., *Influences of sample preparation on the indentation size effect and nanoindentation pop-in on nickel*. 2012.

[143] Liu, Y. and A. Ngan, *Depth dependence of hardness in copper single crystals measured by nanoindentation*. Scripta Materialia, 2001. **44**(2): p. 237-241.
[144] Xia, Y., et al., *Synthesis, characterization, and nanoindentation response of single crystal Fe–Cr–Ni alloys with FCC and BCC structures*. Materials Science and Engineering: A, 2014. **611**: p. 177-187.
[145] Yang, T.-n., et al., *Effect of alloying elements on defect evolution in Ni-20X binary alloys*. Acta Materialia, 2018. **151**: p. 159-168.
[146] Zhang, Y., et al., *New ion beam materials laboratory for materials modification and irradiation effects research*. Nuclear Instruments and Methods in Physics Research Section B: Beam Interactions with Materials and Atoms, 2014. **338**: p. 19-30.
[147] Yeh, J.W., et al., *Nanostructured high-entropy alloys with multiple principal elements: novel alloy design concepts and outcomes*. Advanced engineering materials, 2004. **6**(5): p. 299-303.
[148] Cantor, B., et al., *Microstructural development in equiatomic multicomponent alloys*. Materials Science and Engineering: A, 2004. **375**: p. 213-218.
[149] Li, Z., et al., *Mechanical properties of high-entropy alloys with emphasis on face-centered cubic alloys*. Progress in Materials Science, 2019. **102**: p. 296-345.
[150] Shang, Y., et al., *Mechanical behavior of high-entropy alloys: A review*. High-Entropy Materials: Theory, Experiments, and Applications, 2021: p. 435-522.
[151] El-Atwani, O., et al., *Outstanding radiation resistance of tungsten-based high-entropy alloys*. Science advances, 2019. **5**(3): p. eaav2002.
[152] Miracle, D.B. and O.N. Senkov, *A critical review of high entropy alloys and related concepts*. Acta Materialia, 2017. **122**: p. 448-511.
[153] George, E.P., D. Raabe, and R.O. Ritchie, *High-entropy alloys*. Nature reviews materials, 2019. **4**(8): p. 515-534.
[154] Wu, Z., et al., *Temperature dependence of the mechanical properties of equiatomic solid solution alloys with face-centered cubic crystal structures*. Acta Materialia, 2014. **81**: p. 428-441.
[155] Oh, H.S., et al., *Engineering atomic-level complexity in high-entropy and complex concentrated alloys*. Nature communications, 2019. **10**(1): p. 2090.
[156] Zhang, Y., et al., *Effects of 3d electron configurations on helium bubble formation and void swelling in concentrated solid-solution alloys*. Acta Materialia, 2019. **181**: p. 519-529.
[157] Zhang, Z., et al., *Nanoscale origins of the damage tolerance of the high-entropy alloy CrMnFeCoNi*. Nature communications, 2015. **6**(1): p. 10143.
[158] Zhang, J. and W.-Z. Han, *Oxygen solutes induced anomalous hardening, toughening and embrittlement in body-centered cubic vanadium*. Acta Materialia, 2020. **196**: p. 122-132.
[159] Qi, L., *Effects of electronic structures on mechanical properties of transition metals and alloys*. Computational Materials Science, 2019. **163**: p. 11-16.
[160] Zhao, S., G.M. Stocks, and Y. Zhang, *Stacking fault energies of face-centered cubic concentrated solid solution alloys*. Acta Materialia, 2017. **134**: p. 334-345.
[161] Wen, C., et al., *Modeling solid solution strengthening in high entropy alloys using machine learning*. Acta Materialia, 2021. **212**: p. 116917.

[162] Pethicai, J., R. Hutchings, and W.C. Oliver, *Hardness measurement at penetration depths as small as 20 nm*. Philosophical Magazine A, 1983. **48**(4): p. 593-606.
[163] Oliver, W.C. and G.M. Pharr, *An improved technique for determining hardness and elastic modulus using load and displacement sensing indentation experiments*. Journal of materials research, 1992. **7**(6): p. 1564-1583.
[164] Chen, Y., et al., *High-throughput nanomechanical screening of phase-specific and temperature-dependent hardness in Al x FeCrNiMn high-entropy alloys*. Jom, 2019. **71**: p. 3368-3377.
[165] Zhang, P., S. Li, and Z. Zhang, *General relationship between strength and hardness*. Materials Science and Engineering: A, 2011. **529**: p. 62-73.
[166] Cheng, Y.-T. and C.-M. Cheng, *Scaling, dimensional analysis, and indentation measurements*. Materials Science and Engineering: R: Reports, 2004. **44**(4-5): p. 91-149.
[167] Fan, X., R. Qu, and Z. Zhang, *Relation between strength and hardness of high-entropy alloys*. Acta Metallurgica Sinica (English Letters), 2021. **34**(11): p. 1461-1482.
[168] Lu, C., et al., *Radiation-induced segregation on defect clusters in single-phase concentrated solid-solution alloys*. Acta Materialia, 2017. **127**: p. 98-107.
[169] Massalski, T.B., et al., *Binary Alloy Phase Diagrams (American Society for Metals, Metals Park, Ohio, 1986)*. Vol. I, 2017: p. 1100.
[170] Nečas, D. and P. Klapetek, *Gwyddion: an open-source software for SPM data analysis*. Open Physics, 2012. **10**(1): p. 181-188.
[171] Ma, X., et al., *Exploring the origins of the indentation size effect at submicron scales*. Proceedings of the National Academy of Sciences, 2021. **118**(30): p. e2025657118.
[172] Rester, M., C. Motz, and R. Pippan, *Microstructural investigation of the volume beneath nanoindentations in copper*. Acta Materialia, 2007. **55**(19): p. 6427-6435.
[173] Tymiak, N., et al., *Plastic strain and strain gradients at very small indentation depths*. Acta Materialia, 2001. **49**(6): p. 1021-1034.
[174] Heintze, C., et al., *Ion irradiation combined with nanoindentation as a screening test procedure for irradiation hardening*. Journal of Nuclear Materials, 2016. **472**: p. 196-205.
[175] Dao, M., et al., *Computational modeling of the forward and reverse problems in instrumented sharp indentation*. Acta materialia, 2001. **49**(19): p. 3899-3918.
[176] Zhu, P., et al., *Challenges to accurate evaluation of bulk hardness from nanoindentation testing at low indent depths*. Available at SSRN 3793936, 2021.
[177] Kese, K., Z.-C. Li, and B. Bergman, *Method to account for true contact area in soda-lime glass during nanoindentation with the Berkovich tip*. Materials Science and Engineering: A, 2005. **404**(1-2): p. 1-8.
[178] Kese, K. and Z.-C. Li, *Semi-ellipse method for accounting for the pile-up contact area during nanoindentation with the Berkovich indenter*. Scripta materialia, 2006. **55**(8): p. 699-702.
[179] Jin, K., Y. Gao, and H. Bei, *Intrinsic properties and strengthening mechanism of monocrystalline Ni-containing ternary concentrated solid solutions*. Materials Science and Engineering: A, 2017. **695**: p. 74-79.

[180] Durst, K., B. Backes, and M. Göken, *Indentation size effect in metallic materials: Correcting for the size of the plastic zone*. Scripta Materialia, 2005. **52**(11): p. 1093-1097.
[181] Backes, B., et al., *The correlation between the internal material length scale and the microstructure in nanoindentation experiments and simulations using the conventional mechanism-based strain gradient plasticity theory*. journal of Materials Research, 2009. **24**: p. 1197-1207.
[182] Kurpaska, L., et al., *Effects of Fe atoms on hardening of a nickel matrix: Nanoindentation experiments and atom-scale numerical modeling*. Materials & Design, 2022. **217**: p. 110639.
[183] Tang, M., L. Kubin, and G. Canova, *Dislocation mobility and the mechanical response of bcc single crystals: a mesoscopic approach*. Acta Materialia, 1998. **46**(9): p. 3221-3235.
[184] Wei, Q., et al., *Effect of nanocrystalline and ultrafine grain sizes on the strain rate sensitivity and activation volume: fcc versus bcc metals*. Materials Science and Engineering: A, 2004. **381**(1-2): p. 71-79.
[185] Sarkar, A. and J. Chakravartty, *Activation volume and density of mobile dislocations in plastically deforming Zr-1pctSn-1pctNb-0.1 pctFe alloy*. Metallurgical and Materials Transactions A, 2015. **46**: p. 5638-5643.
[186] Lucas, B. and W. Oliver, *Indentation power-law creep of high-purity indium*. Metallurgical and materials Transactions A, 1999. **30**: p. 601-610.
[187] Asaro, R.J. and S. Suresh, *Mechanistic models for the activation volume and rate sensitivity in metals with nanocrystalline grains and nano-scale twins*. Acta Materialia, 2005. **53**(12): p. 3369-3382.
[188] Dalla Torre, F., et al., *Deformation behaviour and microstructure of nanocrystalline electrodeposited and high pressure torsioned nickel*. Acta Materialia, 2005. **53**(8): p. 2337-2349.
[189] Laplanche, G., et al., *Thermal activation parameters of plastic flow reveal deformation mechanisms in the CrMnFeCoNi high-entropy alloy*. Acta Materialia, 2018. **143**: p. 257-264.
[190] Gangireddy, S., B. Gwalani, and R.S. Mishra, *Grain size dependence of strain rate sensitivity in a single phase FCC high entropy alloy Al0. 3CoCrFeNi*. Materials Science and Engineering: A, 2018. **736**: p. 344-348.
[191] Cahn, J.W. and F. Nabarro, *Thermal activation under shear*. Philosophical Magazine A, 2001. **81**(5): p. 1409-1426.
[192] Smith, T.M., et al., *Atomic-scale characterization and modeling of 60 dislocations in a high-entropy alloy*. Acta Materialia, 2016. **110**: p. 352-363.
[193] Ding, J., et al., *Tunable stacking fault energies by tailoring local chemical order in CrCoNi medium-entropy alloys*. Proceedings of the National Academy of Sciences, 2018. **115**(36): p. 8919-8924.
[194] Zhang, R., et al., *Short-range order and its impact on the CrCoNi medium-entropy alloy*. Nature, 2020. **581**(7808): p. 283-287.

[195] Dodaran, M.S., et al., *A theoretical calculation of stacking fault energy of Ni alloys: The effects of temperature and composition.* Computational Materials Science, 2021. **191**: p. 110326.
[196] Huang, S., et al., *Temperature dependent stacking fault energy of FeCrCoNiMn high entropy alloy.* Scripta Materialia, 2015. **108**: p. 44-47.
[197] Zaddach, A., et al., *Mechanical properties and stacking fault energies of NiFeCrCoMn high-entropy alloy.* Jom, 2013. **65**: p. 1780-1789.
[198] Li, J.C.-M. and A.K. Mukherjee, *Rate Processes in Plastic Deformation of Materials: Proceedings from the John E. Dorn Symposium*. 1975: American Society for Metals.
[199] Gypen, L. and A. Deruyttere, *Multi-component solid solution hardening: Part 1 Proposed model.* Journal of Materials Science, 1977. **12**: p. 1028-1033.
[200] Toda-Caraballo, I., *A general formulation for solid solution hardening effect in multicomponent alloys.* Scripta Materialia, 2017. **127**: p. 113-117.
[201] Mishra, R., N. Kumar, and M. Komarasamy, *Lattice strain framework for plastic deformation in complex concentrated alloys including high entropy alloys.* Materials Science and Technology, 2015. **31**(10): p. 1259-1263.
[202] Zhang, Y., et al., *Solid-solution phase formation rules for multi-component alloys.* Advanced engineering materials, 2008. **10**(6): p. 534-538.
[203] Bolt, H., et al., *Materials for the plasma-facing components of fusion reactors.* Journal of nuclear materials, 2004. **329**: p. 66-73.
[204] Tsai, M.-H. and J.-W. Yeh, *High-entropy alloys: a critical review.* Materials Research Letters, 2014. **2**(3): p. 107-123.
[205] Wu, Z., et al., *Recovery, recrystallization, grain growth and phase stability of a family of FCC-structured multi-component equiatomic solid solution alloys.* Intermetallics, 2014. **46**: p. 131-140.
[206] He, J., et al., *Effects of Al addition on structural evolution and tensile properties of the FeCoNiCrMn high-entropy alloy system.* Acta Materialia, 2014. **62**: p. 105-113.
[207] Ming, K., et al., *Grain boundary decohesion by nanoclustering Ni and Cr separately in CrMnFeCoNi high-entropy alloys.* Science advances, 2019. **5**(12): p. eaay0639.
[208] Chen, D., et al., *Helium accumulation and bubble formation in FeCoNiCr alloy under high fluence He+ implantation.* Journal of Nuclear Materials, 2018. **501**: p. 208-216.
[209] Yan, Z., et al., *He behavior in Ni and Ni-based equiatomic solid solution alloy.* Journal of Nuclear Materials, 2018. **505**: p. 200-206.
[210] Fan, Z., et al., *Helium irradiated cavity formation and defect energetics in Ni-based binary single-phase concentrated solid solution alloys.* Acta Materialia, 2019. **164**: p. 283-292.
[211] Zhang, Y., T. Egami, and W.J. Weber, *Dissipation of radiation energy in concentrated solid-solution alloys: Unique defect properties and microstructural evolution.* Mrs Bulletin, 2019. **44**(10): p. 798-811.
[212] Zhang, Y., et al., *Atomic-level heterogeneity and defect dynamics in concentrated solid-solution alloys.* Current Opinion in Solid State and Materials Science, 2017. **21**(5): p. 221-237.

[213] Wang, Z., C. Liu, and P. Dou, *Thermodynamics of vacancies and clusters in high-entropy alloys*. Physical Review Materials, 2017. **1**(4): p. 043601.
[214] Aidhy, D.S., et al., *Point defect evolution in Ni, NiFe and NiCr alloys from atomistic simulations and irradiation experiments*. Acta Materialia, 2015. **99**: p. 69-76.
[215] Ullah, M.W., et al., *Damage accumulation in ion-irradiated Ni-based concentrated solid-solution alloys*. Acta Materialia, 2016. **109**: p. 17-22.
[216] Averback, R., R. Benedek, and K. Merkle, *Ion-irradiation studies of the damage function of copper and silver*. Physical Review B, 1978. **18**(8): p. 4156.
[217] Eldrup, M. and B. Singh, *Studies of defects and defect agglomerates by positron annihilation spectroscopy*. Journal of nuclear materials, 1997. **251**: p. 132-138.
[218] Selim, F., *Positron annihilation spectroscopy of defects in nuclear and irradiated materials-a review*. Materials Characterization, 2021. **174**: p. 110952.
[219] Song, E., M.T. Andani, and A. Misra, *Investigation of grain size and geometrically necessary dislocation density dependence of flow stress in Mg-4Al by using nanoindentation*. Acta Materialia, 2024. **265**: p. 119633.
[220] Feng, G. and W.D. Nix, *Indentation size effect in MgO*. Scripta materialia, 2004. **51**(6): p. 599-603.
[221] Kiener, D., et al., *Application of small-scale testing for investigation of ion-beam-irradiated materials*. Journal of Materials Research, 2012. **27**(21): p. 2724-2736.
[222] Kasada, R., et al., *A new approach to evaluate irradiation hardening of ion-irradiated ferritic alloys by nano-indentation techniques*. Fusion engineering and design, 2011. **86**(9-11): p. 2658-2661.
[223] Saleh, M., et al., *Relationship between damage and hardness profiles in ion irradiated SS316 using nanoindentation–Experiments and modelling*. International Journal of Plasticity, 2016. **86**: p. 151-169.
[224] Mattucci, M., et al., *Indentation size effect, geometrically necessary dislocations and pile-up effects in hardness testing of irradiated nickel*. Acta Materialia, 2021. **207**: p. 116702.
[225] Zong, Z., et al., *Indentation size effects in the nano-and micro-hardness of fcc single crystal metals*. Materials Science and Engineering: A, 2006. **434**(1-2): p. 178-187.
[226] Huang, Y., et al., *A model of size effects in nano-indentation*. Journal of the Mechanics and Physics of Solids, 2006. **54**(8): p. 1668-1686.
[227] Weber, W.J. and Y. Zhang, *Predicting damage production in monoatomic and multi-elemental targets using stopping and range of ions in matter code: Challenges and recommendations*. Current Opinion in Solid State and Materials Science, 2019. **23**(4): p. 100757.
[228] Wiedersich, H., *Effects of the primary recoil spectrum on microstructural evolution*. Journal of nuclear materials, 1991. **179**: p. 70-75.
[229] Yang, L., et al., *Deformation mechanisms in single crystal Ni-based concentrated solid solution alloys by nanoindentation*. Materials Science and Engineering: A, 2022. **856**: p. 143685.
[230] Hardie, C.D., S.G. Roberts, and A.J. Bushby, *Understanding the effects of ion irradiation using nanoindentation techniques*. Journal of Nuclear Materials, 2015. **462**: p. 391-401.

[231] Hosemann, P., et al., *Nanoindentation on ion irradiated steels*. Journal of Nuclear Materials, 2009. **389**(2): p. 239-247.
[232] Hasenhuetl, E., et al., *Evaluation of ion-irradiation hardening of tungsten single crystals by nanoindentation technique considering material pile-up effect*. Materials transactions, 2017. **58**(5): p. 749-756.
[233] Tang, Z., et al., *Examining the effect of pileup on the accuracy of sharp indentation testing*. Advances in Materials Science and Engineering, 2015. **2015**(1): p. 528729.
[234] Bolshakov, A. and G. Pharr, *Influences of pileup on the measurement of mechanical properties by load and depth sensing indentation techniques*. Journal of materials research, 1998. **13**(4): p. 1049-1058.
[235] Xu, Z.-H. and J. Ågren, *An analysis of piling-up or sinking-in behaviour of elastic–plastic materials under a sharp indentation*. Philosophical Magazine, 2004. **84**(23): p. 2367-2380.
[236] Gupta, J., et al., *Characterization of ion irradiation effects on the microstructure, hardness, deformation and crack initiation behavior of austenitic stainless steel: Heavy ions vs protons*. Journal of Nuclear Materials, 2018. **501**: p. 45-58.
[237] Taylor, G.I., *The mechanism of plastic deformation of crystals. Part I.—Theoretical*. Proceedings of the Royal Society of London. Series A, Containing Papers of a Mathematical and Physical Character, 1934. **145**(855): p. 362-387.
[238] Johnson, K., *The correlation of indentation experiments*. Journal of the Mechanics and Physics of Solids, 1970. **18**(2): p. 115-126.
[239] Hill, R., *The mathematical theory of plasticity*. Vol. 11. 1998: Oxford university press.
[240] Fivel, M., et al., *Three-dimensional modeling of indent-induced plastic zone at a mesoscale*. Acta materialia, 1998. **46**(17): p. 6183-6194.
[241] Kiener, D., et al., *Microstructural evolution of the deformed volume beneath microindents in tungsten and copper*. Acta materialia, 2006. **54**(10): p. 2801-2811.
[242] Demir, E., et al., *Investigation of the indentation size effect through the measurement of the geometrically necessary dislocations beneath small indents of different depths using EBSD tomography*. Acta Materialia, 2009. **57**(2): p. 559-569.
[243] McLaughlin, K. and W. Clegg, *Deformation underneath low-load indentations in copper*. Journal of Physics D: Applied Physics, 2008. **41**(7): p. 074007.
[244] Yaghoobi, M. and G.Z. Voyiadjis, *Atomistic simulation of size effects in single-crystalline metals of confined volumes during nanoindentation*. Computational Materials Science, 2016. **111**: p. 64-73.
[245] Feng, G., et al., *Indentation size effects in single crystal copper as revealed by synchrotron x-ray microdiffraction*. Journal of Applied Physics, 2008. **104**(4).
[246] Xiao, X. and L. Yu, *Nano-indentation of ion-irradiated nuclear structural materials: A review*. Nuclear Materials and Energy, 2020. **22**: p. 100721.
[247] Heintze, C., F. Bergner, and M. Hernández-Mayoral, *Ion-irradiation-induced damage in Fe–Cr alloys characterized by nanoindentation*. Journal of Nuclear Materials, 2011. **417**(1-3): p. 980-983.
[248] Oliver, W.C. and G.M. Pharr, *Measurement of hardness and elastic modulus by instrumented indentation: Advances in understanding and refinements to methodology*. Journal of materials research, 2004. **19**(1): p. 3-20.

[249] Francis, H., *Phenomenological analysis of plastic spherical indentation*. 1976.
[250] Au, P., et al., *Flow property measurements from instrumented hardness tests*. Non-destructive evaluation in the nuclear industry, 1980: p. 597-610.
[251] Sinclair, G., P. Follansbee, and K. Johnson, *Quasi-static normal indentation of an elasto-plastic half-space by a rigid sphere—II. Results*. International Journal of Solids and Structures, 1985. **21**(8): p. 865-888.
[252] Pavlina, E. and C. Van Tyne, *Correlation of yield strength and tensile strength with hardness for steels*. Journal of materials engineering and performance, 2008. **17**: p. 888-893.
[253] Takakuwa, O., Y. Kawaragi, and H. Soyama, *Estimation of the yield stress of stainless steel from the Vickers hardness taking account of the residual stress*. Journal of Surface Engineered Materials and Advanced Technology, 2013. **3**(04): p. 262.
[254] Rudnitsky, V., A. Kren, and G. Lantsman, *Determining yield strength of metals by microindentation with a spherical tip*. Russian Journal of Nondestructive Testing, 2019. **55**: p. 162-168.
[255] Herbert, E., et al., *On the measurement of stress–strain curves by spherical indentation*. Thin solid films, 2001. **398**: p. 331-335.
[256] Pathak, S., et al., *Analyzing indentation stress–strain response of LaGaO3 single crystals using spherical indenters*. Journal of the European Ceramic Society, 2008. **28**(11): p. 2213-2220.
[257] Vachhani, S., R. Doherty, and S. Kalidindi, *Effect of the continuous stiffness measurement on the mechanical properties extracted using spherical nanoindentation*. Acta Materialia, 2013. **61**(10): p. 3744-3751.
[258] Hay, J., *Instrumented indentation apparatus having indenter punch with flat end surface and instrumented indentation method using the same*. 2019, Google Patents.
[259] Uchic, M.D., et al., *Sample dimensions influence strength and crystal plasticity*. Science, 2004. **305**(5686): p. 986-989.
[260] Kiener, D., et al., *In situ nanocompression testing of irradiated copper*. Nature materials, 2011. **10**(8): p. 608-613.
[261] Qu, H.J., et al., *Understanding plasticity in irradiated alloys through TEM in situ compression pillar tests*. Journal of Materials Research, 2020. **35**(8): p. 1037-1050.
[262] Jeong, J., et al., *In-situ TEM observation of {101 2} twin-dominated deformation of Mg pillars: Twinning mechanism, size effects and rate dependency*. Acta Materialia, 2018. **158**: p. 407-421.
[263] Yu, Q., et al., *In situ TEM observation of FCC Ti formation at elevated temperatures*. Scripta Materialia, 2017. **140**: p. 9-12.
[264] Reichardt, A., et al., *Nanoindentation and in situ microcompression in different dose regimes of proton beam irradiated 304 SS*. Journal of Nuclear Materials, 2017. **486**: p. 323-331.
[265] Yang, L., et al., *Nanoindentation study on early-stage radiation damage in single-phase concentrated solid solution alloys*. Materials Science and Engineering: A, 2024: p. 146746.

[266] Wu, Z. and H. Bei, *Microstructures and mechanical properties of compositionally complex Co-free FeNiMnCr18 FCC solid solution alloy*. Materials Science and Engineering: A, 2015. **640**: p. 217-224.
[267] Sneddon, I.N., *The relation between load and penetration in the axisymmetric Boussinesq problem for a punch of arbitrary profile*. International journal of engineering science, 1965. **3**(1): p. 47-57.
[268] Hertz, H., *Miscellaneous papers*. 1896: Macmillan.
[269] Zener, C. and J.H. Hollomon, *Effect of strain rate upon plastic flow of steel*. Journal of Applied physics, 1944. **15**(1): p. 22-32.
[270] Swift, H.W., *Plastic instability under plane stress*. Journal of the Mechanics and Physics of Solids, 1952. **1**(1): p. 1-18.
[271] Ludwik, P., *Elemente der technologischen Mechanik*. 1909: Springer.